POLITECNICO
MILANO 1863

Master Thesis

Transonic Flow Features in a Nozzle Guide Vane Passage

Author:
Alessandro Ceci
836523

Supervisor:
Prof. Gianluca Montenegro

Co-Supervisors:
Post-Doc. Romain Gojon
Prof. Mihai Mihaescu

Politecnico di Milano

A thesis submitted in fulfillment of the requirements
for the degree in

Aeronautical Engineering

School of Industrial and Information Engineering

Academic Year 2016/2017

Politecnico di Milano

Abstract

School of Industrial and Information Engineering

Aeronautical Engineering

Transonic Flow Features in a Nozzle Guide Vane Passage

by Alessandro CECI

The entropy noise in modern engines is mainly originating from two types of mechanisms. First, chemical reactions in the combustion chamber lead to unsteady heat release which is responsible of the direct combustion noise. Second, hot and cold blobs of air coming from the combustion chamber are advected and accelerated through turbine stages, giving rise to the so-called entropy noise (or indirect combustion noise). In the present work, numerical characterization of indirect combustion noise of a Nozzle Guide Vane passage was assessed using three-dimensional Large Eddy Simulations. The study was conducted on a simplified topology of a real turbine stator passage, for which experimental data were available in transonic operating conditions. First, a baseline case was reproduced to validate a numerical finite volume solver against the experimental measurements. Then, the same solver is used to reproduce the effects of incoming entropy waves from the combustion chamber and to characterize the additional generated acoustic power. Periodic temperature fluctuations are imposed at the inlet, permitting to simulate hot and cold packets of air coming from the unsteady combustion. The incoming waves are characterized by their characteristic wavelength; therefore, a parametric study has been conducted varying the inlet temperature of the passage, generating entropy waves of greater wavelengths. The study proves that the generated indirect combustion noise can be significant. Moreover, the generated indirect combustion noise increases as the wavelength of the incoming disturbances increases. Finally, the present work suggests that, in transonic conditions, there might be flow features which enhance the indirect combustion noise generation mechanism.

Politecnico di Milano

Sommario

School of Industrial and Information Engineering

Aeronautical Engineering

Transonic Flow Features in a Nozzle Guide Vane Passage

by Alessandro CECI

Nei motori areonautici moderni, il rumore associato alla grandezza termodinamica entropia ha origine principalmente da due meccanismi. Per prima cosa, le reazioni chimiche all'interno della camera di combustione danno origine ad un rilascio di un flusso di calore instazionario, il quale è responsabile della generazione del rumore di combustione diretto. Inoltre, porzioni di aria calda e fredda provenienti dalla camera di combustione sono accelerate attraverso i vari stadi della turbina, dando origine al soprannominato *rumore entropico* (o altresí noto come rumore di combustione indiretto). Nel presente lavoro, la caratterizzazione numerica del rumore di combustione indiretto attraverso le pale guida dello statore di una turbina è stata effettuata grazie all'utilizzo di simulazioni fluidodinamiche LES (Large Eddy Simulations). Lo studio è stato condotto su una geometria semplificata di un reale statore, per il quale erano disponibili i dati sperimentali relativi a condizioni operative transoniche. All'inizio, un caso di riferimento è stato riprodotto mediante le simulazioni numeriche in modo da validare un solutore ai volumi finiti attraverso un confronto con i dati sperimentali. In seguito, lo stesso solutore è stato utilizzato per riprodurre gli effetti di un sistema di *onde di entropia* provenienti dalla camera di combustione e per caratterizzare un'eventuale generazione di potenza acustica addizionale rispetto al caso base di riferimento. Fluttuazioni periodiche di temperatura sono state imposte all'ingresso del dominio computazionale, permettendo di simulare masse di aria calda e fredda derivanti dalla combustione instazionaria. Uno studio parametrico è stato effetuato variando la lunghezza d'onda delle fluttuazioni, tramite l'imposizione di temperature di ingresso differenti. Lo studio dimostra che l'intensitá del rumore di combustione indiretto puó essere significativa e puó aumentare qualora aumentino le lunghezze d'onda delle fluttuazioni. Infine, il presente lavoro suggerisce che, in condizioni transoniche, possano esserci caratteristiche della corrente fluidodinamica che favoriscano la generazione del rumore di combustione indiretto.

Acknowledgements

I want to express my gratitude to my supervisors Prof. Gianluca Montenegro, Post-Doc. Romain Gojon and Prof. Mihai Mihaescu for inspiring and guiding me throughout my work.

Thank you Valeriu Dragan, Lukas Schickhofer, Niclas Berg, and Asuka Gabriele Pietroniro for welcoming me in your group and for the pleasing time spent together. Special thanks to Asuka Gabriele Pietroniro for providing me the CAD model.

Sincere thanks go to my friends and colleagues at Politecnico di Milano and KTH for all the fruitful discussions, for the support and for making my stay in the university a joyful experience.

Grazie di cuore Mamma e Papà per aver sempre creduto in me ed in ogni mia scelta. Grazie a tutta la mia famiglia, che mi ha sostenuto e mi è stata sempre vicino, sebbene spesso i chilometri di distanza non fossero pochi.

Grazie Giada, che con la tua dolcezza e detreminazione mi hai accompagnato in questo lungo viaggio. Sei stata luce nelle giornate più buie e forza nei momenti più difficili.

The simulations of this work were performed at the PDC Center for High Performance Computing (PDC-HPC) and at the High Performance Computing Center North (HPC2N), on resources provided by the Swedish National Infrastructure of Computing (SNIC).

. . . ad Antonino Francesconi

Contents

List of Figures

List of Tables

Chapter 1

Introduction and Motivation

1.1 Introduction

The role of civil aviation in modern transportation is of primary importance, driving a sustainable economic and social development. According to the latest ICAO navigation plan [1], 3.3 billion passengers are annually carried on scheduled traffic, in addition global air traffic has doubled in size once every 15 years since 1977 and will continue to do so. In this continuously increasing trend, noise emissions started to develop into a subject of great burden for society. Inevitably, the reduction and the control of noise emissions are fundamental for community approval and economic relevance.

Although in the last decades engineers constantly improved their designs for noise reduction, aircraft noise is still considered the most annoying source among the transportation ones.

1.2 Noise Pollution in Modern Civil Aviation

Noise pollution of aircraft is due to two types of noise above all: *aerodynamic-* and *mechanical-noise*. The first one radiates from a fluid flow that interacts with a solid body immersed in it, while the latter originates mainly from the engine, i.e. from jets, combustors and turbomachinery.

The earliest theoretical work on this subject started in 1951 with M. J. Lighthill [2], who described such phenomena in a very meaningful way: "*The airflow may contain fluctuations as a result of instability, giving at low Reynolds numbers a regular eddy pattern which is responsible for the sound produced by musical wind instrument, and at high Reynolds numbers an irregular turbulent motion which is responsible for the roar of the wind and of jet airplanes; or they may be inherent in the mechanism for producing flow, as in the siren, or in machinery containing rotating blades*".

A qualitative description of engine noise sources is pictured in Figure 1.1. Efforts in the last decades have been made in order to significantly reduce jet and fan noise, some examples are the *chevrons* (the "V" shaped patterns at the trailing edge of jet nozzles), the sophisticated designs of fan blades and the introduction of very high bypass ratio turbofan engines.

All these successful attempts have hence left combustion noise as a big remaining contributor in the scenario and the present thesis will primarily asses this particular noise source.

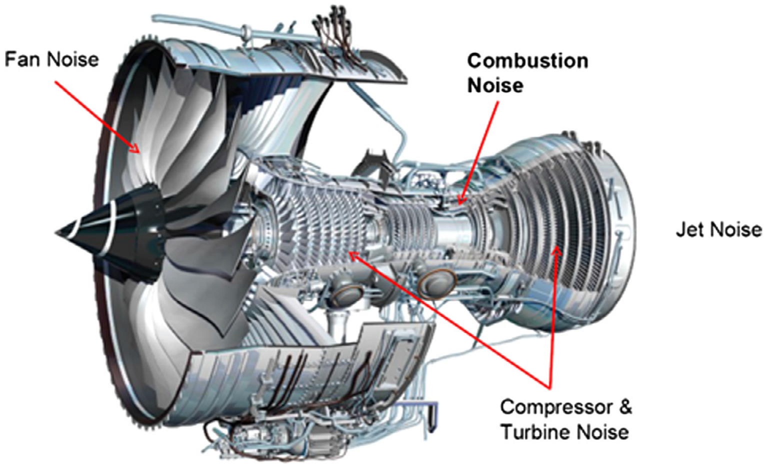

FIGURE 1.1: Engine noise sources (Rolls-Royce Trent 100, copyright Rolls-Royce), Figure from [3].

1.2.1 Aircraft Noise and Health Consequences

High levels of air traffic may have a significant impact on every day life in modern society and it is becoming increasingly important to evaluate medically and scientifically the effects of aircraft related noise.

Numerous field studies have been conducted nowadays, with particular interest on annoyance, medical diseases and functional disorders [4].

Erikson et al.[5] conducted an intensive study on a 10 year period among 20137 men in the age of 40-60 years. They concluded that exposure to aircraft noise above $50\,\mathrm{dB(A)}$ (FBN) was linked significantly to a 20% increase in the risk of hypertension.

The HYENA study [6], instead, extensively documented the importance of nocturnal aircraft noise exposure in the development of hypertension. It studied a group of 4861 adults in between 45 and 70 years living in the proximity of six European airports exposed to continuous nocturnal noise levels. The investigation showed that a $10\,\mathrm{dB}$ increase in the night-time noise level was significantly correlated with a 14% raise in the probability of being diagnosed with hypertension.

The most extensive study in terms of medical prescription increase was performed in the neighborhood of Köln-Bonn Airport (Germany) [7]. Individual informations related to medical prescriptions of 809379 persons insured with health-care insurance firms were analyzed: the research underlined the existence of a strong relationship between the aircraft noise intensity and the prescriptions of antihypertensive pharmaceuticals. Figure 1.2 shows the association between exposure and effect.

Learning disorders or difficulties related studies showed impacts on cognitive performances without detectable signs of damage. Investigations on children (aged from 9 to 10 years) in 89 schools showed correlations between deterioration in memory performance and aircraft noise exposure of the schools [8].

Finally, a study in the proximity of Frankfurt Airport showed that aircraft noise is classified as the greatest objectionable source of noise [9].

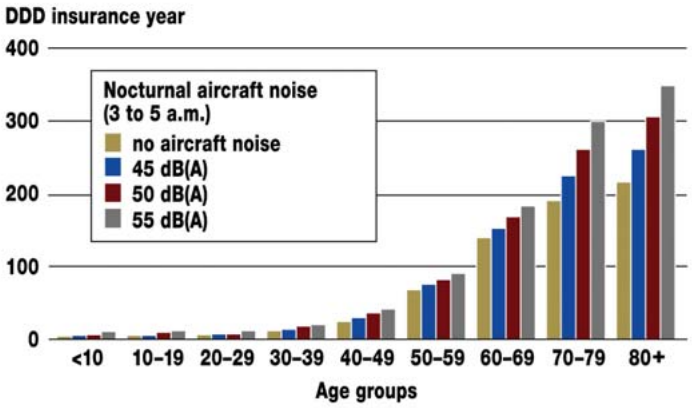

FIGURE 1.2: Relation between antihypertensive pharmaceuticals prescriptions and night-time aircraft noise exposure level in women (with and without exposure). Calm areas had no aircraft noise and road-rail noise level below 35 dB(A). Figure from [4]. DDD = defined daily doses.

1.3 Indirect Combustion Noise in Literature

Figure 1.3 shows the relative importance of combustion noise with respect to other sources in aero-engines on a typical approach, underlining its importance in the frequency range of $200 - 1000$ Hz.

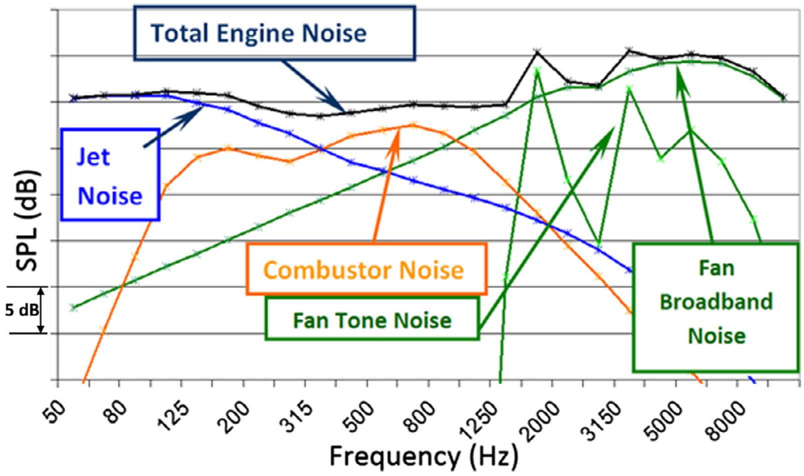

FIGURE 1.3: Typical SPL spectrum on a turbojet engine at approach (from SAFRAN Snecma, http://www.safran-group.com/), Figure from [3].

The combustion noise in aero-engines is known to originate from two different sources. First, the unsteady heat release due to chemical reactions in the combustion chamber generates the direct combustion noise, which is related to volumetric expansion and contraction of gases in the reactive region [10, 11]. Second, hot and cold spots of air generated by the combustion process are advected and accelerated by the turbine stages via strong mean flow gradients, giving rise to the so-called entropy noise or indirect combustion noise. This type of noise source was early investigated in the works of Candel [12] and Marble & Candel [13]. They proposed an analytical model for the convection of non-uniform temperature regions through a nozzle in several configurations: subsonic, supersonic and supersonic with shock in the divergent. The model assumes quasi-one-dimensional inviscid flow and compactness of the nozzle, i.e. the perturbations are considered quasi-steady. The relations linking the different perturbations are established using only conservation laws. In supersonic operations the critical mass-flow is also imposed at the throat.

A definitive analytical model of indirect combustion noise for any geometry and disturbance type is still missing in literature [14]; recent developments have been made by Howe [15] who transformed the momentum equation in Crocco's form into an acoustic analogy equation and found a solution to the non compact nozzle problem using the Green's function. In his work he also took into account the noise contribution from separated flow in the divergent section.

From an experimental point of view an extensive study of entropy noise in nozzle flows has been carried out by Bake *et al.* [16] and it consists of a straight tube flow with a heating module and a nozzle where the flow is accelerated. A schematic representation of the experiment can be visualized in Figure 1.4.

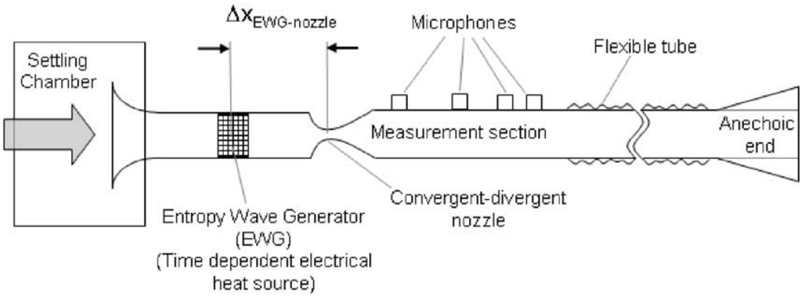

FIGURE 1.4: Schematic representation of the entropy wave generator (EWG) experimental setup, Figure from [16].

A large variety of numerical investigation of the EWG experiment can also be found in literature, in the present thesis the author analyzed the work conducted by Bake *et al.* [16] and Leyko *et al.* [17]. The results showed that the pressure signals obtained in the EWG experiment come from two main mechanisms: the entropy-to-acoustic conversion of the perturbations via strong mean velocity gradients in the nozzle, including the presence of the shock in the divergent, and the acoustic reflection at the exhaust due to the non perfect anechoic outlet. The numerical and experimental pressure fluctuations signals are in very close agreement in the low-limit frequency of the incoming perturbations (nozzle compactness). In this low frequency range only 1D planar wave are present and the compact assumption is valid.

Different types of investigation on entropy noise analyze, instead, the generation of acoustic disturbances through turbine blade rows.

In 1977 Cumpsty and Marble [18] proposed an analytical method, based on the actuator disk theory, for the evaluation of indirect combustion noise through several turbine stages. It is based on the axial compactness assumption for the blade geometry (analogously to the nozzle one) but it considers a 2D configuration taking into account the flow deflection due to the circumferential component of the turbomachine, which induces vorticity fluctuations. The axial Mach number is also assumed to be subsonic, even though the flow may leave the blade passage at supersonic discharge conditions. The axial compactness assumption implies that the wavelength

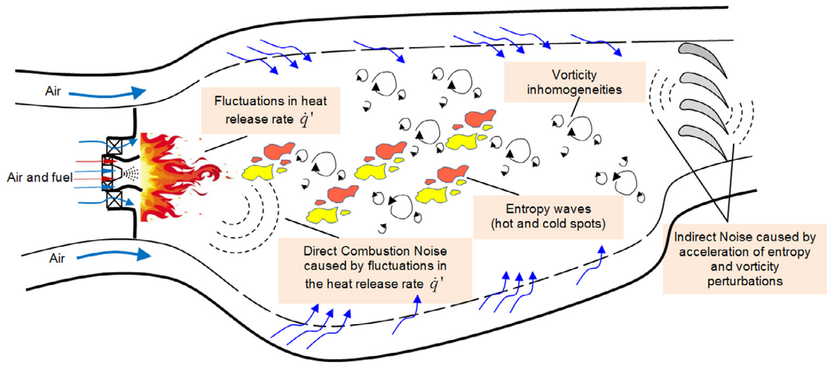

FIGURE 1.5: Graphic representation of entropy noise generation and transmission in an aero-engine, Figure from [3].

of the disturbance λ is large compared to the axial chord C_{ax}. The different perturbations are related once again by the means of conservation laws and choking condition at the throat (in case of supersonic discharge).

Leyko *et al.* [19] analyzed the wave generation and transmission mechanism from a numerical perspective. In their work they assessed the range of validity of the compact assumption for a stator blade row, comparing the analytical results with simulation data. The incoming disturbances used in the simulations were planar 1D temperature pulses and the acoustic response of the row was evaluated.

Both the acoustic responses predicted by the simulations and the analytical model agreed for the cases where $\lambda/C_{ax} > 10$; while theoretical results rapidly differ from the numerical ones at higher frequencies. This discrepancy is due to the fact that in Cumpsty and Marble's model [18] the incoming planar entropy waves are convected with no distortion through the blades. Planar entropy waves, instead, were shown to be strongly distorted in the inter blade passage at high frequencies in the numerical simulations.

An extensive experimental study was recently conducted, instead, in the high pressure turbine facility at Politecnico di Milano in the framework of the European funded project RECORD (Research on Core Noise Reduction) [20]. Two turbine operating conditions were investigated, subsonic and transonic respectively. Entropy noise was evaluated by comparison of the acoustic signals with respect to the ones without any flow disturbances. The study was also carried out for different frequencies and different amplitudes of the excitations. The entropy wave excitation was shown to generate additional acoustic power correlating to the temperature amplitude of the incoming disturbances.

1.4 Thesis Outline

Indirect combustion noise through a nozzle guide vane will be the core content of the present thesis. The present work will try to offer a more in depth description of the mechanism in the energy transfer between different thermodynamic quantities. Numerical analyses will be conducted by the means of Large Eddy Simulations (LES) in order to provide an accurate description of the phenomenon regardless from the validity of the axial compactness assumption.

Chapter 1 offered an introduction to the problem of interest, underlining the impact that noise has on human health and the main features of indirect combustion noise.

Chapter 2, on the other hand, will present the mathematical description of compressible flows, dealing with the equations that govern the motion of a fluid and with the thermodynamic description of the latter.
Chapter 3 will introduce the numerical modeling of the problem starting with the presentation of the finite volume method. Then, the different discretization schemes and the turbulence models will be described in detail. The mathematical description is also referred to the solver *foam-extend* which has been adopted in the simulations.
Chapter 4 is focusing the attention on the physics of the problem. The main geometrical and mesh details will be presented. The simulation of the baseline case will constitute the starting point for the validation of the solver and for the correct reproduction of the flow physics.
In Chapter 5 the entropy to acoustic conversion mechanism will be addressed by imposing a planar entropy wave-train (in terms of temperature fluctuations) at the inlet of the computational domain. Several analysis will be conducted in terms of different wavelengths of the incoming disturbances.
Finally, Chapter 6 will conclude the work, also proposing some reflections on what might be the continuation of the study.

Chapter 2

Compressible Flows

2.1 Kinematics and Dynamics of Compressible Flows

Fluid mechanics is the science studying the motion and the dynamics of gases and liquids. *Compressible-fluid* dynamics is the study of those in which density is not uniform and plays an essential role in the physical description [21].

The phenomena analyzed in this thesis occupy a category where compressibility effects are a crucial descriptive aspect of the flow field: the fluid speed is of the same order of magnitude as the speed of sound and wave propagation within the fluid is fundamental.

The laws governing the fluid motion will be explained in the following subsections. The fluid is considered to be unstructured matter, regardless how fine it might be divided. This concept is called *continuum* assumption and the fluid properties are treated as punctual in space and they are continuous functions of space and time.

An important concept of this model is the *material volume*, that is a collection of identical matter enclosed by a *material surface* which moves with the local fluid velocity. The material volume moves through space and can change its shape and volume during the motion. If the material volume is reduced to the limit of a point, it results in a *fluid particle*. The material volume and surface will be labeled respectively as $V(t)$ and $S(t) = \partial V(t)$, where (t) expresses the explicit dependence on time of the latter quantities.

2.1.1 Eulerian vs Lagrangian Description

In fluid motion, the change of configuration results in a displacement, which in general is composed by a *rigid body displacement* and a *deformation*. The rigid body displacement consists of a simultaneous translation or rotation of the volume without change in shape and size. The deformation implies, instead, the change in shape or size from an initial configuration $\zeta_0(V)$ to a deformed state $\zeta_t(V)$ [22].

When analyzing the motion of a fluid, it is necessary to describe the entire sequence of deformation throughout time. One way to describe such a process is to use the Lagrangian description: the position and the physical properties of the fluid in terms of the referential coordinates and time. In this case the reference state is the undeformed condition $\zeta_0(V)$ at $t = 0$. From the Lagrangian description, the displacement is expressed by a mapping function $\chi(\cdot)$, such that $\mathbf{x} = \chi(\mathbf{X}, t)$. The vector $\mathbf{X}$ is the position vector that a fluid particle has in the undeformed configuration, while the vector $\mathbf{x}$ represents the deformed state.

Physical and kinematic quantities are expressed as functions of the position vector and time: $Q = Q(\mathbf{X}, t)$. Therefore in the Lagrangian description the derivative of the quantity with respect to time is simply

$$\frac{\mathrm{d}}{\mathrm{d}t}[Q(\mathbf{X},t)] = \frac{\partial}{\partial t}[Q(\mathbf{X},t)]. \tag{2.1}$$

Given $\mathbf{x}$ the instantaneous position of the fluid particle, the flow velocity $\mathbf{u}$ and acceleration $\mathbf{a}$ are given by

$$\mathbf{u} = \frac{\mathrm{d}\mathbf{x}}{\mathrm{d}t} = \frac{\partial \chi(\mathbf{X},t)}{\partial t} \tag{2.2}$$

$$\mathbf{a} = \frac{\mathrm{d}^2\mathbf{x}}{\mathrm{d}t^2} = \frac{\partial^2 \chi(\mathbf{X},t)}{\partial t^2}. \tag{2.3}$$

Continuity in the Lagrangian description is expressed by the spatial and temporal continuity of the mapping from the reference configuration to the deformed configuration of the material points. The function $\chi(\cdot)$ and $Q(\cdot)$ are single-valued and continuous, with continuous derivatives with respect to space and time.

Thanks to continuity, the map $\chi(\cdot)$ can be inverted in order to track backwards the starting position $\mathbf{X}$ of a fluid particle currently at position $\mathbf{x}$. In this case, the current configuration $\zeta_t(V)$ is taken as the reference configuration. This particular way to describe the fluid motion is called Eulerian description and it is conveniently applied in fluid mechanics. The Eulerian description focuses on what is happening at a fixed point in space as time passes by, instead of focusing on individual particles that moves through space and time. The kinematic property of greatest interest is the rate at which change is taking place rather than the shape of the body of fluid at a reference time [22].

The mathematical description of the motion is given by the inverse of the mapping function $\chi(\cdot)$, such that $\mathbf{X} = \chi^{-1}(\mathbf{x},t)$. For such a description to exist it is necessary and sufficient that the Jacobian determinant is different from zero, i.e. $J = \left|\frac{\partial \chi_i}{\partial X_j}\right| \neq 0$.

The physical property Q in the Eulerian description is then expressed as

$$Q(\mathbf{X},t) = Q[\chi^{-1}(\mathbf{x},t),t] = q(\mathbf{x},t). \tag{2.4}$$

And the rate of change of such a property is simply

$$\frac{\mathrm{d}}{\mathrm{d}t}[q(\mathbf{x},t)] = \frac{\partial}{\partial t}[q(\mathbf{x},t)] + \frac{\partial}{\partial x_i}[q(\mathbf{x},t)]\frac{\mathrm{d}x_i}{\mathrm{d}t}, \tag{2.5}$$

where the first term is often refereed as the *local* or *unsteady* rate of change and the second term as the *convective* rate of change.

For the case where $x_i(t)$[1] is restricted to be the position of a fluid particle, $\frac{\mathrm{d}x_i}{\mathrm{d}t}$ is the velocity component u_i. By convention, the derivative expressed in equation (2.5) is indicated with the special notation introduced by Stokes:

$$\frac{\mathrm{D}q}{\mathrm{D}t} = \frac{\partial q}{\partial t} + u_i \frac{\partial q}{\partial x_i}. \tag{2.6}$$

This is the *material* derivative of q and this operator has the usual properties of space-time derivatives.

---

[1] In this thesis the kinematic description is mostly based on the *indicial* notation (sometimes the vectorial notation is used if it becomes handier or if a more general description wants to be given). The spatial coordinates will be represented by three Cartesian components x_1, x_2, x_3, which are the components of the position vector.

In the case of q being the velocity field $\mathbf{u}$, the *material acceleration* is

$$\mathbf{a} = \frac{\mathrm{D}\mathbf{u}}{\mathrm{D}t} = \frac{\partial \mathbf{u}}{\partial t} + u_i \frac{\partial \mathbf{u}}{\partial x_i}. \tag{2.7}$$

2.1.2 Kinematics

During its motion, a fluid particle is subjected to deformations according to the surrounding motion of neighboring particles [21]. The motion of a particle at location $\mathbf{x} + \mathrm{d}\mathbf{x}$ with respect to one located at $\mathbf{x}$ can be calculated knowing all the nine components of the *velocity gradient* tensor[2] at position $\mathbf{x}$. This will show how the fluid particle deforms and it is a complete description around the position $\mathbf{x}$. The velocity gradient tensor is expressed as

$$D_{ij} = \frac{\partial u_i}{\partial x_j}. \tag{2.8}$$

It can be further split into its symmetric and antisymmetric parts:

$$D_{ij} = \frac{1}{2}\Big(\frac{\partial u_i}{\partial x_j} + \frac{\partial u_j}{\partial x_i}\Big) + \frac{1}{2}\Big(\frac{\partial u_i}{\partial x_j} - \frac{\partial u_j}{\partial x_i}\Big). \tag{2.9}$$

The first term on the right hand side is the *rate-of-deformation* tensor or often called the *rate-of-strain* tensor. It is denoted by

$$S_{ij} \equiv \frac{1}{2}\Big(\frac{\partial u_i}{\partial x_j} + \frac{\partial u_j}{\partial x_i}\Big) \tag{2.10}$$

and it is symmetric, i.e. $S_{ij} = S_{ji}$ [3]
the second term is instead the *spin* tensor,

$$\Omega_{ij} = \frac{1}{2}\Big(\frac{\partial u_i}{\partial x_j} - \frac{\partial u_j}{\partial x_i}\Big), \tag{2.11}$$

which is antisymmetric, i.e. $\Omega_{ij} = -\Omega_{ji}$. It is straight forward to notice that due to the antisymmetric property the spin tensor has zeros on the main diagonal. This can be used as an advantage and Ω_{ij} can be replaced by an appropriate vector, the *vorticity* vector:

$$\omega_k = \partial_i u_j \epsilon_{ijk}{}^{4}. \tag{2.12}$$

The relation between the spin tensor and the vorticity vector is given by

$$\Omega_{ik} = \frac{1}{2}\epsilon_{ijk}\omega_j. \tag{2.13}$$

Finally, it is important to state some properties for the strain rate tensor, the spin tensor and the vorticity vector [21]:

---

[2] Tensors are mathematical objects used to describe physical properties and they are generalization of scalars, vectors and matrices. The word tensor in this thesis will refer to second-order tensors, which are distinguished from ordinary matrices. The difference between tensors and matrices is that certain tensors' components combinations are *invariant* under axis rotation and the individual components transform themselves according to specific laws of transformation. In other words, tensors themselves are independent of a particular choice of basis.

[3] A better and more general description of S_{ij} would be achieved expressing its components in any general reference system with orthogonal curvilinear coordinates, i.e. $S_{ij} = \frac{1}{2}[\hat{\eta_i}\cdot(\hat{\eta_j}\cdot\nabla)\mathbf{u}+\hat{\eta_j}\cdot(\hat{\eta_i}\cdot\nabla)\mathbf{u}]$. Where η_1, η_2, η_3 are the versors.

[4] ϵ_{ijk} is the *Levi-Civita* permutation symbol.

- The components of the strain tensor are all equal to zero for the case of rigid body motion. The strain tensor represents fluid deformations.
- The trace of the strain tensor is the divergence of the velocity field and represents the relative rate of volume growth or contraction of a fluid particle, it is invariant with respect to the choice of coordinates directions.
- the vorticity vector represents the local rate of rotation of the fluid particle and it is twice the angular velocity of rigid body motion. Flows which exhibits zero vorticity vector are called *irrotational* flows.

One further result from kinematics is the *Reynold's transport theorem*, which allows to express the rate of change of a volume integral of the generic quantity q on an arbitrary moving control volume:

$$\frac{\mathrm{d}}{\mathrm{d}t}\int_{V^*(t)} q\ \mathrm{d}V = \int_{V^*(t)} \frac{\partial q}{\partial t}\ \mathrm{d}V + \int_{S^*(t)} q\mathbf{b}\cdot\mathbf{n}\ \mathrm{d}S. \tag{2.14}$$

The two terms on the right end side are the two contributions to the rate of change of the integral: the first term expresses the local change in time of q within the volume, while the second term is the rate of change of q at each element $\mathrm{d}A$ due to new space regions enveloped by the boundary motion of the surface $S^*(t)$, where $\mathbf{b}$ is the boundary velocity and $\mathbf{n}$ is the local normal versor to the surface.
Reynold's transport theorem can be applied to a particular volume, the material volume. In that case the boundary velocity $\mathbf{b}$ is simply the fluid velocity $\mathbf{u}$ and the equation (2.14) becomes

$$\frac{\mathrm{d}}{\mathrm{d}t}\int_{V(t)} q\ \mathrm{d}V = \int_{V(t)} \frac{\partial q}{\partial t}\ \mathrm{d}V + \int_{S(t)} q\mathbf{u}\cdot\mathbf{n}\ \mathrm{d}S. \tag{2.15}$$

With the Reynold's transport theorem, it is possible to deduce the governing equations of fluid dynamics from the conservation laws of mass, linear momentum and energy applied to the material volume [23].

2.1.3 Conservation of Mass

The mass of the material volume is conserved in time and the conservation of mass has the form

$$\frac{\mathrm{d}m_V}{\mathrm{d}t} = \frac{\mathrm{d}}{\mathrm{d}t}\int_{V(t)} \rho\,\mathrm{d}V = 0. \tag{2.16}$$

This is the *integral* form of the conservation of mass.
Applying the Reynold's transport theorem, equation (2.16) becomes

$$\int_{V(t)} \frac{\partial \rho}{\partial t}\ \mathrm{d}V + \int_{S(t)} \rho u_j n_j\ \mathrm{d}S = 0. \tag{2.17}$$

Here the velocity of the boundary $\mathbf{b}$ is directly the velocity of the fluid $\mathbf{u}$, which is defined in the entire flow-field. Then the divergence theorem can be applied on the second term of equation (2.17) in order to obtain

$$\int_{V(t)} \left[\frac{\partial \rho}{\partial t} + \frac{\partial}{\partial x_j}(\rho u_j)\right]\mathrm{d}V = 0. \tag{2.18}$$

For the arbitrariness of $V(t)$ and in absence of discontinuities the previous integral equation is equivalent to the differential equation

$$\frac{\partial \rho}{\partial t} + \frac{\partial}{\partial x_j}(\rho u_j) = 0, \tag{2.19}$$

which is the *local* form of the conservation of mass, also known as the *continuity* equation.

2.1.4 Balance of Linear Momentum

The balance of linear momentum[5] matches the rate of change of the linear momentum in the material volume to the net body force plus the net surface force acting on it:

$$\frac{\mathrm{d}}{\mathrm{d}t}\int_{V(t)} \rho u_i \,\mathrm{d}V = \int_{V(t)} \rho g_i \,\mathrm{d}V + \int_{S(t)} T_i \,\mathrm{d}S. \tag{2.20}$$

Among the body forces, only the gravitational force is considered in the momentum equation, i.e. $g_i = -g\delta_{i3}$, where g is the intensity of the gravitational field and δ_{ij} is the Kronecker delta[6].

Considering now the surface type of force in a fluid, the vector T_i is the surface force per unit area. This vector depends on the orientation of the material surface and, at a given point in space and time, it can be written as $\mathbf{T} = \mathbf{T}(\mathbf{n})$. Taking one imaginary surface ΔS with a normal $\mathbf{n}$, the generic state of stress can have components directed both along the normal and the tangential direction. The state of stress $\mathbf{T}$ must therefore depend on three distinct vectors representing the internal action among the fluid particles. It is then necessary to introduce the *stress* tensor. It can be demonstrated that the conservation of angular momentum implies a symmetric structure for such a tensor [21].

In the case of a Cartesian reference system the stress vector can be expressed as

$$T_i = \sigma_{ij} n_j. \tag{2.21}$$

For a fluid at rest (or in rigid body motion) the stress tensor is expected to reduce to its isotropic part only, which is simply the hydrostatic pressure p.

This motivates the decomposition of the stress tensor into

$$\sigma_{ij} = -p\delta_{ij} + \Sigma_{ij} \tag{2.22}$$

The deviatoric part Σ_{ij} of the stress tensor is called the *viscous* stress tensor. It is easy to recognize that since $-p\delta_{ij}$ is symmetric, Σ_{ij} must also be symmetric. It can also be noticed that in the hydrostatic case the state of stress reduces to $T_i = -p\delta_{ij} n_j = -p n_i$.

In order to describe the fluid properties related to internal friction, the relation between the viscous stress tensor and the strain rate tensor must be given. In the simple (but important) case in which this relation is linear, the fluid is called Newtonian viscous fluid. For this particular work, only Newtonian fluids will be considered. Assuming an isotropic fluid, the relation between the viscous stress tensor and the strain tensor depends only on two scalar coefficients. The aforementioned statement

---

[5] Which is the application of Newton's second law to the material volume $V(t)$.

[6] The symbol δ_{i3} indicates that the gravitational force acts on the direction of x_3

derives from the *invariance principle* of tensors with respect to reflections and rotations in space [23, 21]. The constitutive relation $\Sigma_{ij} = \Sigma_{ij}(S_{ij})$ is then given by

$$\Sigma_{ij} = 2\mu S_{ij} + \lambda S_{mm}\delta_{ij}, \tag{2.23}$$

where S_{mm} is the divergence of the velocity field, μ is the *shear (dynamic) viscosity* and λ is the *dilatation viscosity*.
Relation (2.23) can be also written in terms of the *bulk viscosity* $\mu_v = \lambda + \frac{2}{3}\mu$:

$$\Sigma_{ij} = 2\mu\Big(S_{ij} - \frac{1}{3}S_{mm}\delta_{ij}\Big) + \mu_v S_{mm}\delta_{ij}. \tag{2.24}$$

According to *Stokes' hypothesis* the bulk viscosity μ_v should be set equal to zero. This assumption is found to be true only for dilute monoatomic gases both from experiments and Boltzmann kinetic theory [21]. In general, however, the bulk viscosity is proved to be other than zero.
In the following thesis, the adopted numerical solver assumes the stokes hypothesis to hold, therefore the last term on the right hand side of equation (2.24) is set to zero.
In general the viscosity of the fluid depends on its thermodynamic state. In the case of validity of the Stoke's hypothesis, the only coefficient left is μ; then it is possible to write $\mu = \mu(T, p)$.
Finally, combining relation (2.21), the Reynold's transport theorem and divergence theorem, the linear momentum conservation equation becomes:

$$\int_{V(t)} \Big[\frac{\partial}{\partial t}(\rho u_i) + \frac{\partial}{\partial x_j}(\rho u_i u_j)\Big] \mathrm{d}V = \int_{V(t)} \Big[\rho g_i + \frac{\partial \sigma_{ij}}{\partial x_j}\Big] \mathrm{d}V. \tag{2.25}$$

Again, for the arbitrariness of $V(t)$ and in absence of discontinuities the previous integral equation is equivalent to the differential equation

$$\frac{\partial}{\partial t}(\rho u_i) + \frac{\partial}{\partial x_j}(\rho u_i u_j) = \rho g_i + \frac{\partial \sigma_{ij}}{\partial x_j}. \tag{2.26}$$

Using now constitutive relations (2.23) and (2.24), the differential form of balance of linear momentum reads

$$\frac{\partial}{\partial t}(\rho u_i) + \frac{\partial}{\partial x_j}(\rho u_i u_j + p\delta_{ij}) = \rho g_i + \frac{\partial}{\partial x_j}\Big[2\mu\Big(S_{ij} - \frac{1}{3}S_{mm}\delta_{ij}\Big)\Big]. \tag{2.27}$$

2.1.5 Conservation of Energy

The balance of total energy (first law of thermodynamics) simply states that the rate of change of total energy (internal plus kinetic) in the material volume is equal to the power of the forces acting upon it plus the rate at which heat is transfered into it. The power of the forces acting on the material volume is composed by the power of the surface forces (pressure and viscous forces) plus the one of the volume forces; this contribution can be expressed as

$$\dot{W}_{ext} = \int_{S(t)} u_i T_i \,\mathrm{d}S + \int_{V(t)} u_i \rho g_i \,\mathrm{d}V. \tag{2.28}$$

In order to account for the heat transfer due to thermal conduction, the vector q_j represents the heat flux per unit area entering the material volume. The heat flux entering in the control volume is then

$$\dot{Q}_{in} = -\int_{S(t)} q_i n_i \, \mathrm{d}S. \tag{2.29}$$

Assuming now that the heat flux q_i depends on the gradient of temperature in a linear fashion, a simple proportional relation is given by the constitutive *Fourier's law*:

$$q_i = -k\frac{\partial T}{\partial x_i}. \tag{2.30}$$

The constant of proportionality k is known as the *thermal conductivity* and it also depends on the thermodynamic state of the fluid: $k = k(T, p)$.
The conservation of energy then simply reads as

$$\frac{\mathrm{d}E^t_V}{\mathrm{d}t} = \dot{W}_{ext} + \dot{Q}_{in}, \tag{2.31}$$

that is for the material volume[7]

$$\frac{\mathrm{d}}{\mathrm{d}t}\int_{V(t)} E^t \mathrm{d}V = \frac{\mathrm{d}}{\mathrm{d}t}\int_{V(t)} (\rho e^t)\mathrm{d}V = \frac{\mathrm{d}}{\mathrm{d}t}\int_{V(t)} \left[\rho\Big(e + \frac{1}{2}u_i u_i\Big)\right]\mathrm{d}V = \int_{S(t)} u_i T_i \, \mathrm{d}S + \int_{V(t)} u_i \rho g_i \, \mathrm{d}V - \int_{S(t)} q_i n_i \, \mathrm{d}S. \tag{2.32}$$

Repeating the same procedure for the momentum equations and rearranging some terms of the resulting equation, the final differential form of the energy equation can be presented as following

$$\frac{\partial}{\partial t}(\rho e^t) + \frac{\partial}{\partial x_j}[(\rho e^t + p)u_j] = \frac{\partial}{\partial x_j}\left[k\frac{\partial T}{\partial x_j} + 2\mu u_i\Big(S_{ij} - \frac{1}{3}S_{mm}\delta_{ij}\Big)\right] + u_i \rho g_i. \tag{2.33}$$

2.2 Thermodynamic Description

The resulting set of equations derived from the conservation laws of mass, linear momentum and energy consists in a system of five equations[8], but they contain the variables ρ, u_i, p, T, e^t, μ and k, which appear to be of a greater number. In order to solve the aforementioned system of partial differential equations it is necessary to have the same number of equations as the number of unknowns.
The thermodynamics of motion, hence, occupies a fundamental role in the description of compressible flows, which will be far from complete without it.
The characterization of a particular thermodynamic system is far from a trivial task from a rigorous mathematical point of view, which involves familiarity with the axiomatic character of thermodynamics and multi-variable calculus.
In the present work, an extensive dissertation of thermodynamics is avoided and the reader is invited to consult references [24, 21, 23] for a deeper knowledge of the subject.
This work will limit the analysis to a specific thermodynamic model for the assessment of air properties, which will be later used in numerical simulations. The goal is still to close the system of differential equations in order to derive the final system

---

[7] In the energy equation E^t, e^t and e are respectively the total energy per unit volume, the specific total energy and the specific internal energy.

[8] One for the mass, three for the momentum and one for the energy respectively.

of *compressible Navier-Stokes equations*.

Even if the word *thermodynamics* seems to be pointing to physical phenomena in continuous development, it is usually refereed as the subject which deals with approximately permanent states of uniform matter, the *equilibrium states*.

In this text, the matter will be considered to be in a fluid state (liquid or gas), with isotropic properties (independent from the spatial direction). Moreover the fluid is considered to remain always in its liquid or gas state, without phase changes. Finally, it is assumed that the fluid is *single component*, i.e. it is constituted by a single chemical specie. The resulting system is called *simple thermodynamical system*.

Equilibrium states are characterized by some quantities that completely define the system in that particular state. Such quantities are called *state variables*. A simple system stays in its equilibrium state unless some quantities are modified by a particular condition happening inside or outside the system[9]. Moreover any changes are assumed to take place very slowly.

State variables can be *extensive* or *intensive*. Extensive variables are quantities which are proportional to the extension of the system, while intensive[10] variables are independent from system's dimensions.

According to the *state principle* the local thermodynamic state is fixed by any two independent variables [11]; if for example the pair (e, ρ) of independent thermodynamic variables is selected, any other variable is known in terms of these two: i.e. $p = p(e, \rho)$, $T = T(e, \rho)$, $s = s(e, \rho)$ and so on (where s is the specific entropy). Relations of this type are called *equations of state*, and in this way any thermodynamic quantity appearing in the equations of motion can be expressed in terms of the two independent ones.

One equation of state of particular interest is the famous *thermal* equation of state for an ideal gas $p = p(\rho, T)$:

$$p = \rho R T, \tag{2.34}$$

where $R = \frac{\tilde{R}}{\tilde{M}}$, being $\tilde{R}$ and $\tilde{M}$ the universal gas constant and the molecular weight respectively.

This equation alone is, anyway, insufficient to completely determine all the properties of the given state at (ρ, T); i.e. the other thermodynamic variables cannot be determined from (2.34) alone. An additional relation is needed; a common one is the specification of the *caloric* equation of state [21]

$$e = e(\rho, T). \tag{2.35}$$

It is then possible to show that equations (2.34) and (2.35) are sufficient to determine any other property of the considered fluid.

An alternative way to completely determine the thermodynamic state of a system resides in the knowledge of the *fundamental thermodynamical relation*

$$s = s(e, v), \tag{2.36}$$

or

$$e = e(s, v), \tag{2.37}$$

---

[9] A thermodynamic system can be open, closed or isolated. An open system is a system that allows the exchange of mass and energy with the surroundings. A closed system instead only allows energy exchange. Finally an isolated system does not allow any exchange of mass or energy with the surroundings.

[10] Intensive variables are formally derived from extensive ones.

[11] More exactly by the number of reversible works plus one. In this case there is only one reversible work mode [21].

in which v is the specific volume $v = 1/\rho$.
The existence of the inverse of the first fundamental relation follows from the postulates for the function $s = s(e, v)$ [24, 23].
Their name derives from the fact that they implicitly contain the complete specification of the thermodynamic variables of a given system and they alone complete the description.
On the other hand, the equations of state involve quantities which are easier to measure, therefore they can be deduced from well conducted experiments.
Finally the knowledge of two equations of state is equivalent to the knowledge of the fundamental relation[12].
All the previous description refers to the branch of *equilibrium thermodynamics*, which means that the instantaneous rate of change of the local thermodynamic state is not too large.
Even if compressible flows do not appear to be slow, usually the local equilibrium assumption happens to hold in a large variety of phenomena.
Other cases for which this assumption loses its validity are, for example, processes with dissociation, ionization, chemical reactions and other lagging processes called *relaxation processes* [21]. In that particular case the thermodynamic state has also an explicit dependence on time, i.e. $e = e(p, T, t)$.
A reasonable measure to access whether or not the fluid is in local thermodynamic equilibrium is to assign a *relaxation time* τ_{rel} as a measure of the time required for a given quantity to gain back an equilibrium state. If the characteristic time[13] Δt_{fluid} of the fluid satisfies the inequality

$$\Delta t_{\text{fluid}} \gg \tau_{\text{rel}}, \tag{2.38}$$

then it is considered a good approximation to treat the fluid as if it were in local equilibrium. This assumption will be assumed to hold throughout all the analyses done in the present thesis.

2.2.1 The Perfect Gas Model

From the previous considerations, it is now required to construct a thermodynamic model for air, which is the fluid of interest.
First, the thermal equation of state (2.34) is assumed to hold for air throughout the envelope of simulated conditions. Gases for which the aforementioned equation is applicable are called *ideal gases*.
Then, another equation of state is needed in order to close the differential system of equations. The missing equation of state will be a caloric equation of state in a form analogous to the one in (2.35). For certain fluids it is possible to show that the internal energy depends only on temperature [21]: they are fluid for which the specific volume v depends only on p/T, that is $v = v(p/T)$. The important case is hence the one of ideal gases for which $v = R(p/T)^{-1}$.
Two other important quantities in thermodynamics are the *specific heats* at constant volume and pressure, which are respectively defined as

$$c_v = \left.\frac{\partial e}{\partial T}\right|_v, \qquad c_p = \left.\frac{\partial h}{\partial T}\right|_p, \tag{2.39}$$

---

[12] From the homogeneity property of the fundamental relation [24, 23].

[13] For instance it can be the time required for a fluid particle to pass through the vane that will be studied in the present work.

where $h = e + pv$ is the definition of enthalpy. These quantities can be measured through experiments or evaluated by more or less complex analytical models.
For the particular case of $e = e(T)$ only, the exact differentials of internal energy and enthalpy assume hence the form

$$\mathrm{d}e = \frac{\mathrm{d}e}{\mathrm{d}T}\mathrm{d}T = c_v(T)\mathrm{d}T, \qquad \mathrm{d}h = \frac{\mathrm{d}h}{\mathrm{d}T}\mathrm{d}T = c_p(T)\mathrm{d}T. \tag{2.40}$$

Furthermore, there is a relation between c_v and c_p:

$$c_p - c_v = \frac{\mathrm{d}h}{\mathrm{d}T} - \frac{\mathrm{d}e}{\mathrm{d}T} = \frac{\mathrm{d}}{\mathrm{d}T}(h - e) = \frac{\mathrm{d}}{\mathrm{d}T}(RT) = R, \tag{2.41}$$

which is also known as the *Mayer's relation*.
Now the ratio of specific heats

$$\gamma = \frac{c_p}{c_v} \tag{2.42}$$

can be introduced. In general $\gamma = \gamma(T)$ and this ratio will be of great interest for some derivations that will be developed throughout the work.
The last task is now to obtain a model for $c_v(T)$, in order to integrate the respective relation in (2.40) and obtain the missing equation of state $e = e(T)$.
Assuming that the ideal gas model is valid, then in a molecular level it means that the interactions between molecules are negligible and all the energy of the gas resides in the molecules themselves; i.e. the internal potential energy associated with intermolecular forces is negligible.
Recalling the equipartitional principle of classical statistical mechanics, it states that the molecular energy is equally distributed among each degree of freedom. The energy for each degree of freedom is $k_bT/2$, where k_b is the Boltzman constant. For a generic molecules with n_{dof} degrees of freedom the average energy per molecule and per mole are respectively

$$\epsilon = \frac{n_{\mathrm{dof}}}{2}k_bT, \qquad N_\epsilon = \frac{n_{\mathrm{dof}}}{2}\tilde{R}T. \tag{2.43}$$

Finally, given a fixed number of degrees of freedom, the specific internal energy and enthalpy are respectively

$$e(T) - e_0 = \frac{n_{\mathrm{dof}}}{2}RT, \qquad h(T) - h_0 = \frac{n_{\mathrm{dof}} + 2}{2}RT, \tag{2.44}$$

where e_0 and h_0 are two reference states.
From the previous relations it is also trivial to derive the model for $c_v(T)$ and $c_p(T)$, which are respectively

$$c_v(T) = n_{\mathrm{dof}}\frac{R}{2}, \qquad c_p(T) = (n_{\mathrm{dof}} + 2)\frac{R}{2}. \tag{2.45}$$

A diatomic gas has a number of degrees of freedom given by three translation modes of the center of mass, two rotation modes about two principal axes[14] and two vibration modes about the center of mass. The resulting number n_{dof} will then be $n_{\mathrm{dof}} = 7$.
The dependence of the specific heats on the temperature relies in the number of degrees of freedom which are activated for a given temperature. In fact, the equipartition principle fails to predict their correct values if we consider, for instance, air

---

[14] One rotational mode is neglected due to the low moment of inertia with respect to the axis connecting the two molecules.

at room temperature: the predicted values based only on the number n_{dof} will be $c_v = 7R/2$ and $c_p = 9R/2$ and their ratio $\gamma = 9/7$. Instead it is found that the correct value for room condition is $c_v = 5R/2$, $c_p = 7R/2$ and $\gamma = 7/5$.

The reason is that classical statistical mechanics does not take into account for the quantization of energy in vibrational or rotational modes.

It is possible to define a characteristic temperature $\theta_{r,v}$ in order to evaluate if the modes are active or not; if $T \gg \theta_{r,v}$ then the respective degrees of freedom associated to that mode must be accounted for.

For the rotational modes, the characteristic temperature is usually very low, for example nitrogen N_2 and oxygen O_2 have a characteristic rotational temperature θ_r of 2.89[K] and 2.08[K]. Therefore at room temperature there are five degrees of freedom to consider (three translations and two rotations).

For vibrational modes instead, the characteristic temperature is defined as $\theta_v = h\nu/k_b$, where h is the Plank's constant and ν is the natural frequency of the diatomic oscillator. This temperature can be considerably high: using again nitrogen and oxygen as example, it is respectively of 3393[K] and 2273[K]. This analysis leads then to a qualitative relation that allows to consider weather or not rotational modes have to be considered:

$$\begin{aligned} T \gg \theta_v &\rightarrow c_v = 7/2R, \quad c_p = 9/2R, \quad \gamma = 9/7 \\ T \ll \theta_v &\rightarrow c_v = 5/2R, \quad c_p = 7/2R, \quad \gamma = 7/5 \end{aligned}$$

and in the present study the range of temperatures of interest will not be sufficiently large to take into account vibrational modes.

Hence the system of differential equations can be completed with the two equations of state

$$\begin{aligned} p &= \rho R T \\ e &= c_v T. \end{aligned}$$

This type of gas, for which the ideal gas relation (2.34) and $c_v(T) = \text{const}$ hold, is often celebrated as *perfect gas* or *polytropic ideal gas*.

It is also worth to mention that the resulting system of the compressible Navier-Stokes equation is thermodynamically stable, respecting all the assumption of the postulatory thermodynamic theory.

Finally, a concluding remark has to be specified for the dynamic viscosity μ and the thermal conductivity k, which also depend on the thermodynamic state of the fluid. Dynamic viscosity depends sensibly on temperature but very low on pressure. A very useful model, derived from kinetic gas theory, is the *Sutherland's law*

$$\frac{\mu(T)}{\mu_1} = \frac{1 + S/T_1}{1 + S/T}\left(\frac{T}{T_1}\right)^{1/2}, \tag{2.46}$$

where μ_1 is the reference value of viscosity at temperature T_1 (usually $T_1 = 273.15$[K]) equal to $\mu_1 = 1.716e^{-5}$[kg/(m s)] and $S = 110.4$[K] is a constant determined experimentally.

For the thermal conductivity instead the use of the *modified Euken model* is implemented in the solver that will be used in the numerical simulations of the present work. This model is also based on the kinetic theory of gases and is valid for gases over a fairly large range of temperatures below the critical point. The modified Euken model is described in Poling, Prausnitz & O'Connell [25] and is given by

$$\frac{k}{\mu c_v} = 1.32 + 1.77 \frac{R}{c_v}. \tag{2.47}$$

The thermodynamic description is now finalized.

Chapter 3

Numerical Modeling of the Problem

3.1 Conservative Form of Compressible Navier-Stokes Equations

The previous considerations lead to the final representation of the full set of differential equations required to describe the motion of a compressible fluid. They are summarized as follows:

$$\frac{\partial \rho}{\partial t} + \frac{\partial}{\partial x_j}(\rho u_j) = 0$$

$$\frac{\partial}{\partial t}(\rho u_i) + \frac{\partial}{\partial x_j}(\rho u_i u_j + p\delta_{ij}) = \rho g_i + \frac{\partial}{\partial x_j}\left[2\mu\Big(S_{ij} - \frac{1}{3}S_{mm}\delta_{ij}\Big)\right]$$

$$\frac{\partial}{\partial t}(\rho e^t) + \frac{\partial}{\partial x_j}[(\rho e^t + p)u_j] = \frac{\partial}{\partial x_j}\left[k\frac{\partial T}{\partial x_j} + 2\mu u_i\Big(S_{ij} - \frac{1}{3}S_{mm}\delta_{ij}\Big)\right] + u_i\rho g_i$$

$$p = \rho R T$$

$$T = \frac{e}{c_v},$$

where μ and k are described by the two constitutive relations in equations (2.46) and (2.47). Pressure p and Temperature T are defined by the two equation of state that can be rearranged for the couple (ρ, e^t) [1], resulting in a final system of five equations for the five unknowns ρ, u_i, e^t. The system is non linear and a peculiar characteristic relays in its *hybrid* hyperbolic/parabolic nature. In fact the conservation law of mass is hyperbolic, while the conservation laws for linear momentum and energy are parabolic due to the presence of a *laplacian*-like term on the right hand side of these equations [23].

The previous formulation of the compressible Navier-Stokes equations is nearly written in the most suitable form to handle their numerical solution in transonic or supersonic regimes. One important feature of such flows can be the presence of shockwaves, which exhibit large gradients of physical quantities in a very tiny region of space. In order to avoid a ridiculously fine discretization in space (leading to enormous computational costs) an appropriate approach will be discussed in this

---

[1] One must recall the expression of the specific internal energy $e = e^t - u_i u_i/2$.

chapter.

It consists in a numerical procedure suited for the solution of the compressible Navier-Stokes equations in their integral form: *the Finite Volume Method*.

This solution method requires the formulation of the conservation laws in terms of their *conservative variables*: $(\rho, \rho u_i, \rho e^t)$.

For a clearer mathematical expression, the aforementioned set of variables will be translated into a new one

$$(\rho, \rho u_i, \rho e^t) \to (\rho, m_i, E^t),$$

where m_i is the linear momentum vector per unit volume and E^t is the total energy per unit volume.

In absence of external volume forces, $g_i = 0$, the Navier-Stokes equations (for a polytropic ideal gas) can be finally written in their conservative form:

$$\frac{\partial \rho}{\partial t} + \frac{\partial m_j}{\partial x_j} = 0$$

$$\frac{\partial m_i}{\partial t} + \frac{\partial}{\partial x_j}\Big(\frac{m_i m_j}{\rho} + p\delta_{ij}\Big) = \frac{\partial \Sigma_{ij}(m_i/\rho)}{\partial x_j}$$

$$\frac{\partial E^t}{\partial t} + \frac{\partial}{\partial x_j}\Big[(E^t + p)\frac{m_j}{\rho}\Big] = \frac{\partial}{\partial x_j}\Big[k\frac{\partial T}{\partial x_j} + u_i \Sigma_{ij}(m_i/\rho)\Big]$$

$$p = p\Big(\frac{E^t}{\rho} - \frac{m_i m_i}{2\rho^2}, \rho\Big) = \rho(\gamma - 1)\Big(\frac{E^t}{\rho} - \frac{m_i m_i}{2\rho^2}\Big)$$

$$T = T\Big(\frac{E^t}{\rho} - \frac{m_i m_i}{2\rho^2}, \rho\Big) = \frac{1}{c_v}\Big(\frac{E^t}{\rho} - \frac{m_i m_i}{2\rho^2}\Big),$$

where now the constitutive relations for μ and k must be written in terms of the conservative variables specified above.

It can be noticed that all the terms with spatial derivatives appear as the divergence of appropriate fluxes. The fluxes in the momentum and energy equations have two contributions: the flux on the left hand side corresponding to the one of an inviscid and non-thermally conductive fluid, and the diffusive flux on the right hand side due to the real character of the fluid with non-zero dissipation properties.

With that set of equations, it is now possible to move forward to the description of the finite volume method.

3.2 The Finite Volume Method

The differential formulation of the compressible Navier-Stokes equation can be written in a more compact way using a vectorial notation:

$$\frac{\partial \mathbf{U}}{\partial t} + \nabla \cdot \mathbf{F}(\mathbf{U}) = \nabla \cdot \mathbf{F_v}(\mathbf{U}), \tag{3.1}$$

in which $\mathbf{U}$ is the set of conservative variables $\mathbf{U} = (\rho, m_i, E^t)^T$ and $\mathbf{F}(\mathbf{U})$, $\mathbf{F_v}(\mathbf{U})$ are appropriate fluxes[2]. This particular notation will allow to express the finite volume method in a more general framework.

The solution of these equations is far from being simple for arbitrary spatial domains, requiring often the use of numerical techniques which calculate approximate solutions.

Anyway, the use of system (3.1) still represents a local description of the dynamics of a compressible flow, where the equations are written in a differential form. Compressible flow phenomena are often characterized by large variations of flow quantities over a very tiny region of space, for instance shockwaves or boundary layers. The use of numerical algorithms, which adopt the differential form, must then provide all the possible variations in the entire domain, resulting in a prohibitive spatial discretization of the flow-field.

In this case it is necessary to abandon the differential form of conservation laws in favor of the more suitable integral form. Such a form allows the expression of conservation laws in finite region of space for which the domain is decomposed. This spatial region is represented by a finite number of degrees of freedoms, i.e. a finite number of small elements, called *finite volumes* or *grid cells*. In this work the analysis will only rely on *cell-centered* schemes, where the flow quantities are stored at the centroids of the grid cells.

The integral form of the Navier-Stokes equations is then simply the one obtained from the conservation laws of mass, linear momentum and energy for any arbitrary fixed control volume. They are obtained equating the variation of mass, linear momentum and total energy contained in the fixed control volume to the flux of those quantities entering in the domain through the surface $S = \partial V$.

This form will now be written in the vectorial form

$$\frac{\mathrm{d}}{\mathrm{d}t}\int_V \mathbf{U}\mathrm{d}V + \int_S (\mathbf{F} - \mathbf{F_v})\mathbf{n}\mathrm{d}S = 0. \tag{3.2}$$

This time the control volume does not change in time and the partial derivative inside the first term of equation (3.2) exits outside the integral and assumes the form of the ordinary differential operator $\mathrm{d}/\mathrm{d}t$.

Due to the presence of discontinuities that might propagate in space and time, equation (3.2) must be integrated also with respect to time. Considering the interval of time $[t_n, t_{n+1}]$ and thanks to the fundamental theorem of differential calculus, it leads to

$$\int_V \mathbf{U}(\mathbf{x}, t_{n+1})\mathrm{d}V - \int_V \mathbf{U}(\mathbf{x}, t_n)\mathrm{d}V + \int_{t_n}^{t_{n+1}} \mathrm{d}t \int_S (\mathbf{F} - \mathbf{F_v})\mathbf{n}\mathrm{d}S = 0. \tag{3.3}$$

Due to the use of the cell-centered numerical procedure and the existence of the generic finite volume, one can introduce the mean conservative variables for each control volume and for each time-step[3]; that is

$$\mathbf{U}_j^n = \frac{1}{V_j}\int_{V_j} \mathbf{U}(\mathbf{x}, t_n)\mathrm{d}V, \tag{3.4}$$

---

[2] The subscript $_v$ denotes the viscous fluxes.

[3] Here the subscript $_j$ indicates the flow quantity for the j-th control volume and the superscript ^{n} indicates the n-th time instant.

where V_j indicates the dimension of the j-th control volume.
Writing now equation (3.3) in terms of the mean conservative variables, it results in

$$\mathbf{U}_j^{n+1} V_j = \mathbf{U}_j^n V_j - \int_{t_n}^{t_{n+1}} \mathrm{d}t \int_S (\mathbf{F} - \mathbf{F_v})\mathbf{n} \mathrm{d}S = 0. \tag{3.5}$$

These equations must be written and solved for any finite volume in which the domain is discretized. The knowledge of the conservative variables in any volume leads then to the complete description of the flow [4].
It is important to notice that the variation of the conservative variables in the control volume depends only on the evaluation of the respective fluxes through the surface boundary surrounding it. If the same expression for the fluxes is used between two adjacent volumes, then the flux contribution on a shared surface is exactly one the opposite of the other.
An interesting property of the finite volume method is hence that the discretization does not introduce any error on the flow quantities that are conserved.
Writing the differential problem in this manner it is possible to introduce a new idea of solution, the *weak solution*.
The finite volume method suggested a numerical procedure for the solution of the compressible Navier-Stokes equations. Anyway, equations in the form of (3.2) still hide several difficulties that have to be addressed in order to obtain a correct numerical solution. First the fluxes $\mathbf{F}$ and $\mathbf{F_v}$ depend on the conservative variables $\mathbf{U}$ in a non-linear fashion. Furthermore the viscous fluxes still contain spatial derivatives in their formulation, leading to the mixed hyperbolic-parabolic nature of the system. Finally, the numerical time integration procedure must be handled properly.

3.3 The *foam-extend* Framework

The *foam-extend*[5] Computational Fluid Dynamics (CFD) software is part of an open-source library released under GNU library General Public License [6]. It has an extensive range of features to solve anything from complex fluid flows involving chemical reactions, turbulence and heat transfer, to solid mechanics and electromagnetic fields. For the present thesis, a suitable solver of the compressible Navier-Stokes equation has been chosen in order to compute a time dependent and accurate flow field solution.
The adoption of the finite volume method involves the substitution of the set of governing partial differential equations (PDEs) with a corresponding system of algebraic equations, obtaining the flow variables inside the control volumes and for finite instants of time. The coordinate system is fixed on a Cartesian frame of reference which does not change in time. The control volumes (or cells) can be of any polyhedral shape, with the flow variables that are stored at the center of these polyhedral cells. Therefore, the solution method is called cell-centered finite volume method.
Figure 3.1 represents an arbitrary cell in a finite volumes discretization of *foam-extend*. The quantity $\mathbf{S}_f$ represents the surface area vector, the vector $\mathbf{d}$, instead,

---

[4] Quantities such as the volume averaged velocity or total energy can simply be derived backwards from $\mathbf{u}_j^n = (\rho\mathbf{u})_j^n / \rho_j^n$ and ${e_j^t}^n = (\rho e^t)_j^n / \rho_j^n$.

[5] `https://sourceforge.net/p/openfoam-extend/wiki/Home/`

[6] `https://www.gnu.org/licenses/`

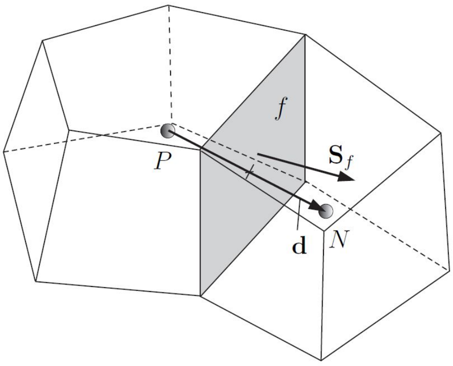

FIGURE 3.1: Generic neighboring control volumes in *foam-extend*, Figure from [26].

represents the distance vector between two cell centers. The labels P and N represent the cell centers points.

3.3.1 The *dbnsTurbFoam* Solver

The numerical simulations are performed using the fully coupled density based solver *dbnsTurbFoam*, developed within the *foam-extend* framework. The aim of this solver is to simulate the unsteady compressible effects within a turbomachinery vane passage.
The simulations are performed by solving the compressible Navier-Stokes equations in their conservative form, which is necessary for capturing possible discontinuities of the flow [27, 28]. The solver adopts the so-called *method of lines* to decouple spatial and temporal discretizations, reducing the governing equations to a system of ordinary differential equations (ODEs) [29]. The spatial convective discretization is performed with the Rusanov flux scheme [30], which is an approximation of the exact Rienman fluxes. This scheme is first order in space but the solver *dbnsTurbFoam* interpolates linearly the state from the cell center to the face center which makes the method of second order. In order to avoid spurious oscillations near regions with sharp gradients the Barth Jespersen limiter [31] is applied. The time integration is performed using an explicit 4-stage low-storage Runge-Kutta algorithm.
The solver has been previously validated on two canonical compressible flow simulations by Chandramouli *et al.* [32]. The present solver embeds Reynolds Averaged Navier-Stokes equations (with Favré averaging) and Large Eddy Simulations turbulence models for the discretization of the viscous fluxes. Viscous fluxes are resolved implicitly in time.

3.3.2 The Rusanov Flux

Due to the mixed hyperbolic-parabolic nature of the set of governing equations, the solution techniques in *dbnsTurbFoam* adopts Godunov's [33] like schemes for convective fluxes. Using the conservative form of Navier-Stokes equations, it is possible to obtain a discrete representation of the equations for the $j-$th control volume:

$$\mathbf{U}_j^{n+1}\, V_j = \mathbf{U}_j^{n}\, V_j - \sum_{k=1}^{N_f} \int_t^{t+\Delta t} \mathbf{F}(\mathbf{U})_k \cdot \mathbf{n}_k S_k \,\mathrm{d}t + \mathrm{RHS}(\mathbf{F_V}(\mathbf{U})), \tag{3.6}$$

where the term $\mathrm{RHS}(\mathbf{F_V}(\mathbf{U}))$ represents a generic contribution of the viscous fluxes, N_f is the number of faces and $(\mathbf{n}_k, S_k)$ are respectively the outward normal and the area of the $k-$th face [7].

The convective flux $\mathbf{F}(\mathbf{U})_k$ at each face is calculated by solving the Riemann problem for the face, that is an initial value problem with discontinuous initial conditions usually referred as *left* and *right* states (in this case they are the state of the two volumes separated by the surface S_k). In order to do that, approximate Riemann solvers are used by the solver.

For the present work, the *Rusanov* central scheme has been adopted for the approximation of the time integral of equation (3.6). Central schemes are suitable for capturing rarefaction waves, which can be either left or right going waves.

For a clearer comprehension, the attention will be moved on a simpler case for a scalar conservation law of the form

$$\frac{\partial U}{\partial t} + \frac{\partial}{\partial x}[f(U)] = 0. \tag{3.7}$$

Now the solution lies in the $x - t$ diagram, with one dimension in space and one dimension in time[8].

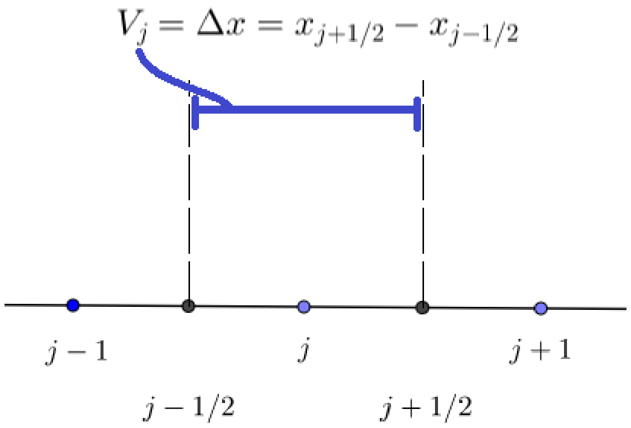

FIGURE 3.2: One-dimensional grid spacing indexing.

Consider, then, a uniform grid with uniform spacing $V_j = \Delta x = x_{j+1/2} - x_{j-1/2}$, the cell center is located in the $j-$th index, while the boundaries are at $j \pm 1/2$. The situation is pictured in Figure 3.2. In this case, the simple integral form of the scalar conservation law is given by

$$U_j^{n+1}\Delta x = U_j^n \Delta x - \Delta t(\tilde{F}_{j+1/2}^n - \tilde{F}_{j-1/2}^n), \tag{3.8}$$

---

[7] In some subsections of the present chapter, the quantity k is just an index and shall not be confused with the thermal conductivity k.

[8] The scalar product with the surface vector $\mathbf{n_k} S_k$ vanishes in the spatial 1D case.

where

$$\tilde{F}^n_{j+1/2} = \frac{1}{\Delta t}\int_t^{t+\Delta t} f[U(x_{j+1/2}, t)]\,\mathrm{d}t. \tag{3.9}$$

Following Godunov's reasoning [33], the numerical flux is constant in time and can be explicitly computed as

$$\tilde{F}^n_{j+1/2} = F^n_{j+1/2}, \tag{3.10}$$

being $F^n_{j+1/2}$ the Riemann flux of the Riemann problem originated at each cell boundary.

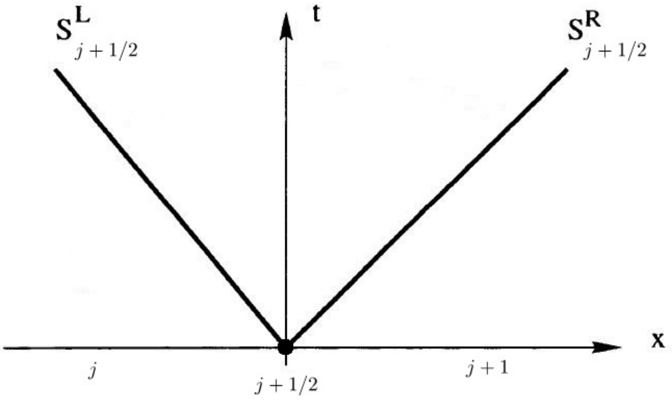

FIGURE 3.3: Schematic structure of the approximate Riemann solver.

The additional idea is to approximate the exact solution of the Riemann problem with two waves, one traveling to the left with speed $s^L_{j+1/2}$, and one traveling to the right $s^R_{j+1/2}$; see Figure 3.3. Then the solution is approximated with

$$U(x,t) = \begin{cases} U^n_j & \text{if} \quad x < s^L_{j+1/2}t \\ U^*_{j+1/2} & \text{if} \quad s^L_{j+1/2}t < x < s^R_{j+1/2}t \\ U^n_{j+1} & \text{if} \quad x > s^R_{j+1/2}t \end{cases}, \tag{3.11}$$

with the two states that are separated by the middle state $U^*_{j+1/2}$. The intermediate state can be determined by using Rankine-Hugoniot jump conditions:

$$f(U^n_{j+1}) - f^*_{j+1/2} = s^R_{j+1/2}(U^n_{j+1} - U^*_{j+1/2}) \tag{3.12}$$

$$f(U^n_j) - f^*_{j+1/2} = s^L_{j+1/2}(U^n_j - U^*_{j+1/2}), \tag{3.13}$$

in which $f^*_{j+1/2}$ is the intermediate flux. Requiring f^* to be an independent variable, equations 3.13 can be solved for the unknown $f^*_{j+1/2}$:

$$f^*_{j+1/2} = \frac{s^R_{j+1/2}f(U^n_j) - s^L_{j+1/2}f(U^n_{j+1}) + s^R_{j+1/2}s^L_{j+1/2}(U^n_{j+1} - U^n_j)}{s^R_{j+1/2} - s^R_{j+1/2}}. \tag{3.14}$$

The numerical flux is chosen to be equal to

$$F^n_{j+1/2} = F(U^n_j, U^n_{j+1}) = f^*_{j+1/2}. \tag{3.15}$$

Finally, the choice of the speeds $(s^R_{j+1/2}, s^L_{j+1/2})$ leads to different types of schemes. The Rusanov scheme locally selects the largest speeds in order to avoid interactions of the waves coming from two different Riemann problems. The speeds are given by

$$s^R_{j+1/2} = s_{j+1/2}, \qquad s^L_{j+1/2} = -s_{j+1/2}, \tag{3.16}$$

where

$$s_{j+1/2} = \max(|f'(U^n_j)|, |f'(U^n_{j+1})|). \tag{3.17}$$

The resulting flux is given by

$$F^n_{j+1/2} = F^{\mathrm{RUS}}(U^n_j, U^n_{j+1}) = \\ \frac{f(U^n_j) + f(U^n_{j+1})}{2} - \frac{\max(|f'(U^n_j)|, |f'(U^n_{j+1})|)}{2}(U^n_{j+1} - U^n_j). \tag{3.18}$$

This scheme is only first order accurate in space, i.e. $\mathrm{err} \propto o(\Delta x)$. In order to overcome this limit and improve spatial accuracy, one can use a piecewise linear reconstruction of the state U when defining the numerical flux F. Then, at the interface $x_{j+1/2}$, two states are obtained from the two linear approximations in each of the neighboring cells. These states are

$$U^L_{j+1/2} = U_j + \frac{\Delta x}{2}\zeta_j \tag{3.19}$$

$$U^R_{j+1/2} = U_j - \frac{\Delta x}{2}\zeta_{j+1}, \tag{3.20}$$

where (ζ_j, ζ_{j+1}) are appropriate slopes. By doing that, spurious oscillations might arise near discontinuities or extreme points. This can be rectified by applying a slope limiter in these regions.

3.3.3 The Barth-Jespersen Limiter

Barth and Jespersen [31] where the first to introduce a two-dimensional limiter wich allowed the computation of oscillation free solutions for transonic flows on irregular triangular meshes [34]. They proposed a limited formulation of the reconstructed solution at each control volume as

$$U(\mathbf{x})_j = U_j + \Phi_j \nabla U_j \cdot \Delta\mathbf{r}_j, \tag{3.21}$$

where U_j is the value at the centroid, and $\Delta\mathbf{r}_j$ is the distance of the flux integration points to the centroid of the cell. The idea is to find the largest possible Φ_j while accounting for the monotonicity principle for which the values of the linear reconstructed state must not exceed the maximum and minimum values of neighboring centroids [31, 35].
First, the differences $U^{\min}_j$ and $U^{\max}_j$ are computed:

$$U^{\min}_j = \min(U_j, U_{\mathrm{neighbours}}), \tag{3.22}$$

$$U^{\max}_j = \max(U_j, U_{\mathrm{neighbours}}). \tag{3.23}$$

Then the requirement

$$U^{\min}_j < U(\mathbf{x})_j < U^{\max}_j \tag{3.24}$$

is imposed.
For a linear reconstruction, the maxima occurs at the vertices of the cell surfaces. For

each vertex k, the quantity $U_k = U(\mathbf{x}_k)$ is computed and the limiting value Φ_j is calculated as $\Phi_j = \min(\overline{\Phi_j})$, with

$$\overline{\Phi_j} = \begin{cases} \min\left(1, \frac{U_j^{\max} - U_j}{U_k - U_j}\right) & \text{if } U_k - U_j > 0 \\ \min\left(1, \frac{U_j^{\min} - U_j}{U_k - U_j}\right) & \text{if } U_k - U_j < 0 \cdot \\ 1 & \text{if } U_k - U_j = 0 \end{cases} \tag{3.25}$$

This procedure guarantees that the reconstructed state variables satisfy the monotonicity principle when evaluated anywhere within a cell.

3.3.4 Treatment of Laplacian Terms

The Laplacian terms in *dbnsTurbFoam* (or more generally in the entire *foam-extend* distribution) are linearized and integrated over a control volume as follows [26]:

$$\int_{V_j} \nabla \cdot (\Gamma \nabla \phi) = \int_{S_j} (\Gamma \nabla \phi) \cdot \mathbf{n} \, \mathrm{d}S = \sum_{k=1}^{N_f} \Gamma_k (\nabla \phi)_k \cdot \mathbf{n}_k S_k, \tag{3.26}$$

in which ϕ is the scalar field of interest and Γ is scalar coefficient which might vary arbitrarily in space (e.g. viscosity). The surface gradient discretization is implicit when the distance vector $\mathbf{d}$ between the cell of interest P and the neighbor cell N is orthogonal to the face plane [26], i.e. simply

$$(\nabla \phi)_k \cdot \mathbf{n}_k S_k = \frac{\phi_N - \phi_P}{|\mathbf{d}|} |S_k|. \tag{3.27}$$

When the mesh is non-orthogonal, an additional explicit term is introduced: it interpolates cell center gradients, which are themselves calculated by central differencing cell center values [26].

3.3.5 Time Integration

The use of the method of lines allows the separation of spatial and temporal discretization of the governing equations. This leads to a system of coupled ordinary differential equation which, for a cell-centred scheme, can be written as [29]

$$\frac{\mathrm{d}}{\mathrm{d}t}(V_j \mathbf{U}_j) = -\mathbf{R}_j. \tag{3.28}$$

The quantity $\mathbf{R}_j$ represents the residual coming form the spatial discretization of convective and viscous fluxes.

The solver *dbnsTurbFoam* utilizes an explicit time integration scheme in order to compute the solution of a successive time-step. This means that the solution $\mathbf{U}^{n+1}$ (i.e. at time $t + \Delta t$) is calculated from a known solution $\mathbf{U}^n$ and from its corresponding residual $\mathbf{R}^n$. Therefore explicit schemes are very simple and easy to implement. In fact the resulting scheme is again formulated as

$$\mathbf{U}_j^{n+1} V_j - \mathbf{U}_j^n V_j = -\Delta t \mathrm{R}_j^n, \tag{3.29}$$

which is analogous to equation (3.6).

Moreover, the time integration adopts a four-stage Runge-Kutta time scheme, which

only stores the zeroth solution and the last residual in order to reduce memory requirements [29]. This schemes are therefore under the name of *low-storage* Runge-Kutta schemes.
The multi-stage scheme advances the solution as a sequence of updates as

$$\begin{aligned}
\mathbf{U}_j^{(0)} &= \mathbf{U}_j^n \\
\mathbf{U}_j^{(1)} &= \mathbf{U}_j^{(0)} - \beta 1 \frac{\Delta t}{V_j} \mathbf{R}_j^{(0)} \\
\mathbf{U}_j^{(2)} &= \mathbf{U}_j^{(0)} - \beta 2 \frac{\Delta t}{V_j} \mathbf{R}_j^{(1)} \\
&\vdots \\
\mathbf{U}_j^{n+1} = \mathbf{U}_j^{(m)} &= \mathbf{U}_j^{(0)} - \beta_m \frac{\Delta t}{V_j} \mathbf{R}_j^{(m-1)}.
\end{aligned} \tag{3.30}$$

The coefficients β_l (with $l = 1, 2, \ldots, m$) are the stage coefficients and the residual $\mathbf{R}_j^i$ means that it is evaluated with the solution $\mathbf{U}_j^{(i)}$ of the $i-$th stage.
For consistency it is only required that the last coefficient $\beta_m = 1$; moreover, second order accuracy in time can be achieved only by putting $\beta_{m-1} = 1/2$ [29]. The vector of coefficient β used by *dbnsTurbFoam* is

$$\beta = \begin{bmatrix} \beta_1 \\ \beta_2 \\ \beta_3 \\ \beta_4 \end{bmatrix} = \begin{bmatrix} 0.11 \\ 0.2766 \\ 0.5 \\ 1 \end{bmatrix}. \tag{3.31}$$

For explicit schemes, the time-step size Δt is strictly related to the governing equations and to the grid size: the solver *dbnsTurbFoam* treats viscous and convective fluxes separately, in addition the time integration of viscous quantities related to turbulence models are treated in an implicit manner; therefore, the time-step is limited by the largest characteristic appearing in the governing equation and the CFL condition [36] has to be satisfied as necessary condition for stability:

$$CFL = \frac{\max[\text{eig}(\mathbf{F}'(\mathbf{U}))]\Delta t}{\min(\Delta_j)} < 1, \tag{3.32}$$

where $\max[\text{eig}(\mathbf{F}'(\mathbf{U}))]$ is related to the maximum speed of the characteristics and $\min(\Delta_j)$ is related to the smallest cells of the discretized domain.

3.3.6 Solution Procedure Algorithm

The code architecture can be summarized by the following steps:

- First, the field is initialized in terms of primitive variables of pressure, temperature and velocity, (p, T, u_i), and in terms of the needed turbulent quantities. The thermodynamic model of the gas, as well as the adopted turbulence model, are also decided at the beginning of the work-flow.
- Then, the code computes the vector of conservative variables for each cell, starting from the primitive ones.

- In order to proceed with the time integration, the code reads if the size of the time-step can be adjustable according to a user defined fixed CFL number, or if it is directly defined by the user. In all simulation of the present thesis, the time-step is manually selected and kept constant throughout the single simulation in order to have $CFL < 0.5$.
- Sequentially, the approximated Riemann problem is solved for neighboring volumes; the convective flux at each cell face of the control volume is constructed by the mean of Rusanov scheme [30] and Barth-Jespersen limiter [31]. After that, the viscous fluxes are computed using the selected turbulence model and differencing schemes.
- At this point, the time integration of mass, momentum and energy conservation laws is performed using the low storage, four-stage Runge-Kutta scheme. The conservative variables are updated.
- Finally, the primitive variables are computed thanks to the complete physical description of the flow available in the model. The solver returns as an output the same set of primitive variables given as input.
- The procedure is iterated until the condition $t_{\text{run}} < t_{\text{final}}$ is satisfied, where t_{run} is the actual physical time of the simulation and t_{final} is the final physical time selected by the user.

3.4 Turbulence Modeling

Turbulent flows pervade a large number of cases of both fundamental and applied research. Simulating and understanding turbulent flows is therefore a key tool for fluid-mechanics and it is still a significant problem, despite the deterministic nature of the chaotic fluctuations.

In turbulent flows, the fluid moves along irregular paths in a chaotic fashion. This extensive mixing of different fluid layers may also results in higher skin friction along solid walls, as well as enhanced heat transfer compared to laminar flows.

The onset of turbulence is characterized by a non dimensional quantity called the *Reynolds number*. The Reynolds number is the ratio of inertial forces to viscous forces within a fluid which is subjected to relative internal movement due to different fluid velocities. It is a very useful quantity used to identify whether the flow is *laminar* or *turbulent*, and it is also used to predict the transition between the two regimes. The definition of the Reynolds number is

$$Re = \frac{\rho V_c L_c}{\mu}, \tag{3.33}$$

in which ρ and μ are respectively the density and the dynamic viscosity of the fluid, while V_c and L_c are the characteristic velocity- and length-scale of the flow.

In order to resolve the complexity of Navier-Stokes equations with *Direct Numerical Simulations* (DNS), the required number of turbulence degrees of freedom in space is of the order $Re^{9/4}$ and of the order of $Re^{3/4}$ in time; which is prohibitive for very large Reynolds numbers, even for modern supercomputers.

In this case, other alternatives need to be found and turbulence must be taken into account in an approximate manner. For this purpose, several *turbulence models* are easily available in literature. In the present work, two principal classes of these models will be treated. Respectively, they are the *multiple equation* models and *Large-Eddy*

Simulations (LES).
It is important to specify that there exist no turbulence model which can reliably predict any kind of turbulent flow and each of them has its strengths and weaknesses. In the present subsection, first the basic equations for turbulent flows will be introduced as a result from mass averaging (Favré averaging) of the governing equations. Then, the *Boussinesq hypotesis* and the two-equation $K-\omega$SST model will be briefly discussed. Finally, the LES approach will be discussed due to the specific interest in the actual work and because of its actual increasing interest and use in engineering applications.

3.5 Averaged Navier-Stokes Equations

One of the first approaches to turbulent flows was first proposed by Osburne Reynolds in 1895. Its idea was to decompose the flow variables q_i into a mean and a fluctuating part, i.e.

$$q_i = \overline{q_i} + q_i'. \tag{3.34}$$

Then, the governing equations are solved for the mean variables, which are often of greater interest. The mean values can be obtained from averaging procedures and there are three forms of Reynolds averaging [29]:

- Time averaging, appropriate for statistically steady turbulence.
  The mean variable is defined as

  $$\overline{q_i} = \lim_{T\to\infty} \frac{1}{T} \int_t^{t+T} q_i \,\mathrm{d}t. \tag{3.35}$$

  The limit for T that goes to infinity means that the averaging interval should be much larger than the temporal scale of turbulent fluctuations.

- Spatial averaging, appropriate for homogeneous turbulence.
  Here, the mean quantity is

  $$\overline{q_i} = \lim_{\Omega\to\infty} \frac{1}{\Omega} \int_\Omega q_i \,\mathrm{d}\Omega, \tag{3.36}$$

  where Ω is the size of the control volume.

- Ensemble averaging, appropriate for general turbulence.
  The mean variable is defined as

  $$\overline{q_i} = \lim_{N\to\infty} \frac{1}{N} \sum_{m=1}^{N} q_i. \tag{3.37}$$

For all the approaches, it results that the average of the fluctuating part is equal to zero, that is $\overline{q_i'} = 0$. Anyhow, the general quantity $\overline{q_i' q_j'} \neq 0$ if the two variables are correlated.
Compressible flows are usually associated with significant density variations, therefore it is advisable to adopt a mass averaging (or Favré) approach for certain quantities [29, 37], instead of the Reynolds averaging procedure. This approach is used in order to avoid the appearance of correlation terms involving the density fluctuations. An usual way to obtain the averaged governing equations, is to use Reynolds

averaging for density and pressure, while using Favré averaging for other variables [29]. For instance, the Favré averaged velocity component is given by

$$\tilde{u_i} = \lim_{T\to\infty} \frac{\int_t^{t+T} \rho u_i \,\mathrm{d}t}{\int_t^{t+T} \rho \,\mathrm{d}t}. \tag{3.38}$$

This decomposition reads, hence

$$u_i = \tilde{u_i} + u_i'', \tag{3.39}$$

where $\tilde{u_i}$ represents the mean value (in the Favré sense) and u_i'' is the fluctuating part. Again the Favré averaged fluctuation is equal to zero, i.e. $\tilde{u_i''} = 0$; but in general $\widetilde{u_i''u_j''} \neq 0$. Some useful relations can be derived using both Reynolds and Favré averaging

$$\widetilde{\rho u_i} = \overline{\rho}\tilde{u_i}, \quad \overline{\rho u_i''} = 0, \quad \text{but} \quad \overline{u_i''} \neq 0, \tag{3.40}$$

which will be used in order to derive the averaged governing equations.
In compressible turbulence modeling, it is often common to assume that the Morkovin's hypothesis holds [29, 37]. It states that the turbulent structures are not largely affected by density fluctuations in the boundary layer if $\rho' \ll \overline{\rho}$. In this study, the Morkovin's hypothesis is assumed to be valid throughout all the simulations.
The application of Reynolds[9] and Favré[10] averaging to the system of governing equations, yields [29] to

$$\begin{gathered}
\frac{\partial\overline{\rho}}{\partial t} + \frac{\partial}{\partial x_j}(\overline{\rho}\tilde{u_j}) = 0, \\
\frac{\partial}{\partial t}(\overline{\rho}\tilde{u_i}) + \frac{\partial}{\partial x_j}(\overline{\rho}\tilde{u_i}\tilde{u_j} + \overline{p}) = \frac{\partial}{\partial x_j}(\tilde{\Sigma_{ij}} - \overline{\rho}\widetilde{u_i''u_j''}), \\
\frac{\partial}{\partial t}(\overline{\rho}\tilde{e^t}) + \frac{\partial}{\partial x_j}(\overline{\rho}\tilde{u_j}\tilde{h^t}) = \frac{\partial}{\partial x_j}\left(k\frac{\partial\tilde{T}}{\partial x_j} - \overline{\rho}\widetilde{u_j''h''} + \widetilde{\Sigma_{ij}u_i''} - \overline{\rho}\widetilde{u_j''K}\right) + \\
\frac{\partial}{\partial x_j}[\tilde{u_i}(\tilde{\Sigma_{ij}} - \overline{\rho}\widetilde{u_i''u_j''})].
\end{gathered} \tag{3.41}$$

The set (3.41) is referred as the Reynolds averaged Navier-Stokes equations with Favré averaging. For conciseness, they will often simply be referred as RANS.
The Reynolds stress tensor concept is also extended to the compressible case, i.e.

$$\Sigma_{ij}^F = -\overline{\rho}\widetilde{u_i''u_j''}, \tag{3.42}$$

which is known as the Favré averaged Reynolds stress tensor. For the molecular viscous stress tensor $\tilde{\Sigma_{ij}}$, its component are calculated using Favré averaging.
Adopting now the averaged kinetic energy expression as

$$\overline{\rho}\tilde{K} = \frac{1}{2}\overline{\rho}\widetilde{u_i''u_i''}, \tag{3.43}$$

the total averaged energy can be expressed as

$$\overline{\rho}\tilde{e^t} = \overline{\rho}\tilde{e} + \frac{1}{2}\overline{\rho}\tilde{u_i}\tilde{u_i} + \frac{1}{2}\overline{\rho}\widetilde{u_i''u_i''} = \overline{\rho}\tilde{e} + \frac{1}{2}\overline{\rho}\tilde{u_i}\tilde{u_i} + \overline{\rho}\tilde{K}. \tag{3.44}$$

---

[9] For density and pressure.

[10] For the others variables.

Analogously, the averaged total enthalpy is defined as

$$\bar{\rho}\tilde{h^t} = \bar{\rho}\tilde{h} + \frac{1}{2}\bar{\rho}\tilde{u}_i\tilde{u}_i + \frac{1}{2}\widetilde{\bar{\rho}u_i''u_i''} = \bar{\rho}\tilde{h} + \frac{1}{2}\bar{\rho}\tilde{u}_i\tilde{u}_i + \bar{\rho}\tilde{K}. \tag{3.45}$$

In the compressible RANS equations (3.41), it is possible to identify individual terms with the following physical meaning [29]:

$$\begin{aligned}
\frac{\partial}{\partial x_j}\left(k\frac{\partial \tilde{T}}{\partial x_j}\right) &\quad - \text{molecular diffusion of heat.}\\
\frac{\partial}{\partial x_j}(\widetilde{\bar{\rho}u_j''h''}) &\quad - \text{turbulent transport of heat.}\\
\frac{\partial}{\partial x_j}(\widetilde{\Sigma_{ij}u_i''}) &\quad - \text{molecular diffusion of } \tilde{K}.\\
\frac{\partial}{\partial x_j}(\widetilde{\bar{\rho}u_j''K}) &\quad - \text{turbulent transport of } \tilde{K}.\\
\frac{\partial}{\partial x_j}(\tilde{u}_i\tilde{\Sigma_{ij}}) &\quad - \text{work done by the molecular stresses.}\\
\frac{\partial}{\partial x_j}(\tilde{u}_i\Sigma_{ij}^F) &\quad - \text{work done by the Reynolds stresses.}
\end{aligned}$$

The diffusion and turbulent transport of $\tilde{K}$ are often neglected, which is a valid approximation for transonic and supersonic flows [29].

Finally, in order to close the complete RANS set of equations, the six components of the compressible Reynolds stress tensor, together with the three components of the turbulent heat flux, have to be supplied for turbulence modeling.

3.5.1 Eddy-Viscosity Hypothesis

One of the first contribution for turbulence closure models was first introduced for incompressible flows by Boussinesq. This hypothesis assumes that the turbulent stresses are related to the mean strain rate in a linear fashion (the same as laminar flow). In this case the proportionality constant is called *eddy* or *turbulent* viscosity. The formulation for compressible flows can be written as

$$\Sigma_{ij}^F = -\widetilde{\bar{\rho}u_i''u_j''} = 2\mu_T\tilde{S_{ij}} - \frac{2}{3}\mu_T S_{mm}\delta_{ij} - \frac{2}{3}\bar{\rho}\tilde{K}\delta_{ij}, \tag{3.46}$$

where $\tilde{S_{ij}}$ and $\tilde{K}$ are respectively the Favré averaged strain rate and turbulent kinetic energy. The eddy viscosity μ_T represents no physical characteristic of the fluid but it is a function of the local flow. Additionally, μ_T is strongly affected by hysteretic effects.

The additional relations for the turbulent heat flux vector are instead based on

$$\widetilde{\bar{\rho}u_j''h''} = -k_T\frac{\partial \tilde{T}}{\partial x_j}, \tag{3.47}$$

with the turbulent thermal conductivity defined as

$$k_T = c_p\frac{\mu_T}{Pr_T}. \tag{3.48}$$

The quantity Pr_T is the turbulent Prandtl number and, in general, is assumed to be constant over the entire flow field. The air turbulent Prandtl number utilized by the solver *dbnsTurbFoam* is equal to $Pr_T = 1.0$.
Applying the eddy viscosity model, the governing equations are simply derived by substituting the *effective* viscosity to the dynamic viscosity coefficient:

$$\mu_{eff} = \mu + \mu_T. \tag{3.49}$$

Furthermore, the effective thermal conductivity replaces the thermal conductivity k. It is defined as

$$k_{eff} = k + k_T = k + c_p \frac{\mu_T}{Pr_T}. \tag{3.50}$$

The Boussinesq hypothesis is very attractive since it reduces the turbulence modeling to the single quantity μ_T.
Anyhow, the limitations of the eddy viscosity model are immediately noticed in the assumption of equilibrium between turbulence and the averaged strain rate. The model is also independent on the rotation tensor $\tilde{\Omega_{ij}}$.

3.5.2 Two Equations $K - \omega$ SST Model

The $K - \omega$ Shear Stress Transport (SST) turbulence model was introduced by Menter [38] with the aim of blending the positive features of standard $K - \omega$ [39] and $K - \epsilon$ [40] models. The main purposes and features are highlighted by Blazek in reference [29] and they will be briefly summarized. The $K - \omega$ SST model employs the $K - \omega$ approach in the viscus sublayer of the boundary layer, with higher numerical stability than the $K - \epsilon$ model. The standard $K - \omega$ is also used in the logarithmic region of the boundary layer where it is evaluated to be better in adverse pressure gradients and for compressible flows. On the other hand, the $K - \epsilon$ model is adopted in the wake region, for which the standard $K - \omega$ is found to be very sensitive to the freestream values of ω. The $K - \epsilon$ model is also used in free shear layers.
The peculiar characteristic of the SST model, is related to its modified turbulent eddy viscosity function. The aim is to accurately predict flows with strong adverse pressure gradients and flows with pressure induced separation. The formulation is based on Bradshaw observation that the principal shear stress is proportional to the turbulent kinetic energy. The transport equations[11] for the turbulent kinetic energy K and for the specific dissipation rate ω read [29]

$$\frac{\partial}{\partial t}(\rho K) + \frac{\partial}{\partial x_j}(\rho u_j K) = \frac{\partial}{\partial x_j}\left[(\mu + \sigma_K \mu_T)\frac{\partial K}{\partial x_j}\right] + \Sigma^F_{ij} S_{ij} - \beta^* \rho \omega K \tag{3.51}$$

$$\begin{aligned}\frac{\partial}{\partial t}(\rho \omega) + \frac{\partial}{\partial x_j}(\rho u_j \omega) = \frac{\partial}{\partial x_j}\left[(\mu + \sigma_\omega \mu_T)\frac{\partial \omega}{\partial x_j}\right] + \frac{C_\omega \rho}{\mu_T} \Sigma^F_{ij} S_{ij} \\ - \beta \rho \omega^2 + 2(1 - f_1)\frac{\rho \sigma_{\omega 2}}{\omega}\frac{\partial K}{\partial x_j}\frac{\partial \omega}{\partial x_j}.\end{aligned} \tag{3.52}$$

The turbulent eddy viscosity is then obtained by

$$\mu_T = \frac{a_1 \rho K}{\max(a_1 \omega, f_2 ||\nabla \times \mathbf{u}||_2)}. \tag{3.53}$$

---

[11] The overline and the tilde symbols will be omitted for the sake of clarity.

This definition of the turbulent viscosity comes from the consideration that the Bradshw's assumption is satisfied. That is the shear is proportional to the kinetic energy, i.e. $\tau_{\text{shear}} = a_1 \rho K$. This condition is also guaranteed in an adverse pressure gradient boundary layer, where the production of K is larger than the specific dissipation ω (hence $a_1\omega < ||\nabla \times \mathbf{u}||_2$). The term f_1, then, corresponds to a function which is responsible of blending the $K - \omega$ coefficients in boundary layers with the (transformed) coefficients of the $K - \epsilon$ model in freestream and free shear layers. Its definition is

$$f_1 = \tanh[(arg_1)^4], \tag{3.54}$$

with

$$arg_1 = \min\Big[\max\Big(\frac{\sqrt{K}}{0.09\omega d_w}, \frac{500\mu}{\rho\omega d_w^2}\Big), \frac{4\rho\sigma_{\omega 2}K}{CD_{K\omega}d_w^2}\Big], \tag{3.55}$$

in which d_w is the distance to the nearest wall and $CD_{K\omega}$ is the positive defined cross-diffusion term defined as

$$CD_{K\omega} = \max\Big(2\frac{\rho\sigma_{\omega 2}}{\omega}\frac{\partial K}{\partial x_j}\frac{\partial \omega}{\partial x_j}, 10^{-20}\Big). \tag{3.56}$$

The second function f_2 is given by

$$f_2 = \tanh[(arg_2)^2], \tag{3.57}$$

with

$$arg_2 = \max\Big(\frac{2\sqrt{K}}{0.09\omega d_w}, \frac{500\mu}{\rho\omega d_w^2}\Big). \tag{3.58}$$

The other model constants are then defined as follows

$$a_1 = 0.31, \;\; \beta^* = 0.09, \;\; \kappa = 0.41. \tag{3.59}$$

Finally, all the coefficients in the SST model (β, C_ω, σ_{Ki} and $\sigma_{\omega i}$) are obtained by blending the coefficients of their respective models. Denoting with ϕ_1 the ones for the K_ω model, and with ϕ_2 the ones of the $K - \epsilon$ modes, the resulting relation reads

$$\phi = f_1\phi_1 + (1 - f_1)\phi_2. \tag{3.60}$$

The $K - \omega$ model coefficients are

$$\sigma_{K1} = 0.85, \;\; \sigma_{\omega 1} = 0.5, \;\; \beta_1 = 0.075, \;\; C_{\omega 1} = \frac{\beta_1}{\beta^*} - \sigma_{\omega_1}\frac{\kappa^2}{\sqrt{\beta^*}} = 0.533. \tag{3.61}$$

Instead, the coefficients for the $K - \epsilon$ model are

$$\sigma_{K2} = 1.0, \;\; \sigma_{\omega 2} = 0.856, \;\; \beta_2 = 0.0828, \;\; C_{\omega 2} = \frac{\beta_2}{\beta^*} - \sigma_{\omega_2}\frac{\kappa^2}{\sqrt{\beta^*}} = 0.440. \tag{3.62}$$

It is possible, indeed,to provide an integral formulation for the variables of the SST model. For a control volume V, with a surface $S = \partial V$, the $K - \omega$ SST model reads

$$\frac{\mathrm{d}}{\mathrm{d}t}\int_V \mathbf{U_T}\,\mathrm{d}V + \int_{\partial V}(\mathbf{F}_{,\mathbf{T}} - \mathbf{F}_{\mathbf{v},\mathbf{T}})\cdot \mathbf{n}\,\mathrm{d}S = \int_V \mathbf{Q_T}\,\mathrm{d}V, \tag{3.63}$$

with the vector of conservative variables being.

$$\mathbf{U_T} = [\rho K \;\; \rho\omega]^T. \tag{3.64}$$

For a more detailed insight of the integral form, the reader is invited to consult the $K-\epsilon$ model description in reference [29]; the extension to the $K-\omega$ SST model can be conducted in the very same way.

3.6 Large Eddy Simulations

The use of the Large Eddy Simulations (LES) approach was already employed in 1963 by Smagorinsky [41], in his works on meteorology. LES are based on the observation that the character of small turbulent scales is more universal than the large eddies. The idea is then to capture (filter) the contribution of the large (energy carrying) turbulent structures to momentum and energy transfer in the flow. The effect of small scales, instead, is modeled, and they are not resolved numerically. The models of the small scales of turbulence are the so-called *subgrid-scale* (SGS) models.
LES describe a 3D, time-dependent solution of the governing equations. In comparison to the RANS equations, they require a much finer discretization in order to resolve a substantial range of turbulent scales. They are, however, considerably less expensive than DNS. This aspect makes the use of LES models appealing for solving engineering problems at a reasonable computational cost.

3.6.1 Spatial Filtering

LES are based on a spatial filtering operation, which decomposes any flow variables u_i into a filtered (resolved) part $\overline{u_i}$ and into a sub-filtered (unresolved) variable u_i':

$$u_i = \overline{u_i} + u_i'. \tag{3.65}$$

The filtered quantity at a spatial location $\mathbf{x_0}$ is defined as

$$\overline{u_i}(\mathbf{x_0}, t) = \int_\Omega u_i(\mathbf{x}, t) G(\mathbf{x_0}, \mathbf{r}, \Delta)\,\mathrm{d}\mathbf{r}, \tag{3.66}$$

in which Ω denotes the flow domain, G is the filter function and $\mathbf{r}$ is the position vector with respect to $\mathbf{x_0}$. The filter function determines the size and structure of the small scales. The filter depends on the difference $\mathbf{x_0} - \mathbf{r}$ and on the width $\Delta = \sqrt[3]{\Delta_1\Delta_2\Delta_3}$, with Δ_i being the filter width in the $i-$th direction. The *foam-extend* framework implicitly uses the simple tophat filter defined as

$$G = \begin{cases} 1/\Delta^3 & \text{if} |(x_0)_i - r_i| \leq \Delta_i/2 \\ 0 & \text{otherwise} \end{cases} \tag{3.67}$$

3.6.2 Filtered Governing Equations

If LES are applied to compressible flows, the Favré averaging procedure has to be used together with the spatial filtering. Otherwise, the resulting governing equation would contain products between density and other variables. In this case, energy, temperature and the velocity components are decomposed using Favré averaging, e.g.

$$u_i = \tilde{u}_i + u_i''. \tag{3.68}$$

The filtered variable at the location $\mathbf{x_0}$ in space is then

$$\tilde{u_i}(\mathbf{x_0}, t) = \frac{\overline{\rho u_i}}{\overline{\rho}} = \frac{1}{\overline{\rho}} \int_\Omega \rho(\mathbf{x}, t) u_i(\mathbf{x}, t) G(\mathbf{x_0}, \mathbf{r}, \Delta)\, \mathrm{d}\mathbf{r}, \tag{3.69}$$

where the overline denotes the filtering operation. The filtered Navier-Stokes equation, using Favré averaging, then read

$$\begin{gathered}
\frac{\partial \overline{\rho}}{\partial t} + \frac{\partial}{\partial x_j}(\overline{\rho}\tilde{u_j}) = 0, \\
\frac{\partial}{\partial t}(\overline{\rho}\tilde{u_i}) + \frac{\partial}{\partial x_j}(\overline{\rho}\tilde{u_i}\tilde{u_j} + \overline{p}) - \frac{\partial \hat{\sigma}_{ij}}{\partial x_j} = -\frac{\partial \Sigma_{ij}^{SF}}{\partial x_j} + \frac{\partial}{\partial x_j}(\overline{\sigma_{ij}} - \hat{\sigma}_{ij}), \\
\frac{\partial}{\partial t}(\overline{\rho}\tilde{E}) + \frac{\partial}{\partial x_j}[u_j(\overline{\rho}\tilde{E} + \overline{p})] - \frac{\partial}{\partial x_j}(\hat{\sigma}_{ij}\tilde{u_i}) + \frac{\partial \hat{q}}{\partial x_j} = \\
-\frac{\partial}{\partial x_j}[(\overline{\rho u_j E} - \overline{\rho}\tilde{u_j}\tilde{E}) + (\overline{u_j p} - \tilde{u_j}\overline{p}) - (\overline{\sigma_{ij} u_j} - \hat{\sigma}_{ij}\tilde{u_j}) - (\overline{q_j} - \hat{q}_j)],
\end{gathered} \tag{3.70}$$

with

$$\begin{aligned}
\overline{\sigma_{ij}} &= \overline{2\mu S_{ij}} - \overline{\frac{2}{3}\mu S_{mm}\delta_{ij}}, \\
\hat{\sigma}_{ij} &= 2\tilde{\mu}\tilde{S_{ij}} - \frac{2}{3}\tilde{\mu}\widetilde{S_{mm}}\delta_{ij}, \\
\tilde{S_{ij}} &= \frac{1}{2}\Big(\frac{\partial \tilde{u_i}}{\partial x_j} + \frac{\partial \tilde{u_j}}{\partial x_i}\Big), \\
\overline{q} &= -k\overline{\frac{\partial T}{\partial x_j}}, \\
\tilde{q_j} &= -\tilde{k}\frac{\partial \tilde{T}}{\partial x_j}, \\
\Sigma_{ij}^{SF} &= \overline{\rho}(\widetilde{u_i u_j} - \tilde{u_i}\tilde{u_j}).
\end{aligned}$$

The right-hand side of the filtered Navier-Stokes equations contains terms that have to be modeled or contain the subgrid heat flux, diffusion, pressure-dilatation and viscous dissipation. A very extensive treatment about those term can be found in the work of Sagaut [37], Blazek [29] and Martin *et al.* [42].

3.6.3 Subgrid-Scale Modeling

Most of the theoretical tools used in LES modeling are developed in the homogeneous turbulence framework. It is where the majority of the SGS models has been set-up. The scenario describing the energy transfer across scales can be framed in the following description [37]: the largest eddies extract the kinetic energy from the mean flow. Such structures, which can be found in areas with high strain-rates, are initially thick and flatten into vortex sheets. The sheets are unstable and tend to roll-up into vortex tubes, which, with their stretching, tend to produce filamentary-like structures. Energetically speaking, this process results in an energy transfer from the largest to the smallest scales.

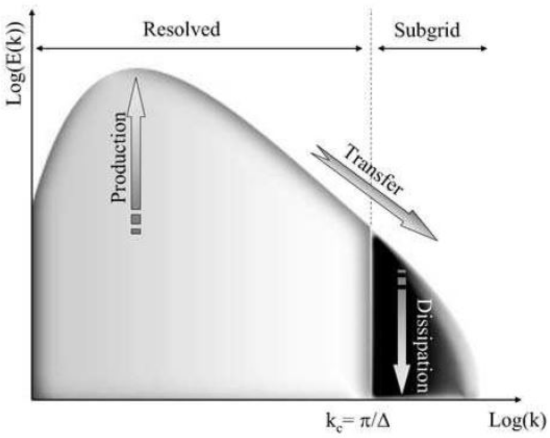

FIGURE 3.4: Typical spectrum for homogeneous turbulence, Figure from [37].

A typical spectrum for homogeneous turbulence is represented in Figure 3.4.
It involves a production zone (at the smallest wavenumber[12] k), an energy transfer zone (where the energy is transferred from the large eddies to the small ones), and eventually a dissipation zone at the smallest scales (largest wavenumbers). The transfer zone is also called *inertial* zone, in which the spectral energy density, E_k, decreases with the Kolmogorov law $E_k \propto k^{-5/3}$.
It is important to state that there might exist an energy transfer from the small scales to the large ones (inverse-cascade, *backscatter*) but its intensity is much weaker than the normal scattering of energy from large to small scales.
Considering a sharp cut-off filter, SGS models are constructed by assuming that the cut-off wave number $k_c = \pi/\Delta$ is located in the inertial range, Figure 3.4, and that the smallest scales are isotropic. This isotropy hypothesis implies some universality of the SGS models. Moreover, the location of the cut-off in the inertial zone allows to assume that the energy transfer throughout the cut-off range is equal to the dissipation rate of the smallest scales. Finally, the smallest scales are assumed to be in energetic equilibrium with the large ones.

3.6.4 Eddy-Viscosity Models

These type of models are able to represent the global dissipative nature of the small turbulent eddies, but they cannot reproduce the local details of energy exchange [37, 29]. For the compressible Navier-Stokes equations, the Favré averaged SGS stress tensor is approximated as

$$\Sigma_{ij}^{SF} - \Sigma_{mm}^{SF}\frac{\delta_{ij}}{3} = -2\bar{\rho}\nu_T\tilde{S}_{ij} + \frac{2}{3}\bar{\rho}\nu_T\widetilde{S_{mm}}\delta_{ij}. \qquad (3.71)$$

Again, the turbulence modeling is moved from the components of the SGS stress tensor to the turbulent viscosity ν_T.

---

[12] Here the use of k should not be confused with the thermal conductivity k used in the governing equations or in the thermodynamic description. The use of the letter k is typical for wavenumbers representation.

It is important to state that for the resulting modeled SGS heat flux, a similar approach can be adopted. The subgrid heat flux can be written as

$$Q_j = \frac{c_p \mu_T}{Pr_T} \frac{\partial \tilde{T}}{\partial x_j}, \tag{3.72}$$

in which the turbulent Prandtl number is again equal to $Pr_T = 1.0$.

3.6.5 One Equation Eddy Model for K_{sgs}

For the present work, a one-equation model for the subgrid-scale kinetic energy $\overline{\rho} K_{sgs} = (1/2)\overline{\rho}(\widetilde{u_i u_i} - \tilde{u_i}\tilde{u_i})$ is adopted for the closure of LES modeling:

$$\frac{\partial}{\partial t}(\overline{\rho} K_{sgs}) + \frac{\partial}{\partial x_j}(\overline{\rho} u_j K_{sgs}) = \frac{\partial}{\partial x_j}(\mu_{eff} \frac{\partial K_{sgs}}{\partial x_j}) - \overline{\rho}\tilde{S_{ij}} B_{ji} - C_{\epsilon}\overline{\rho}\frac{K_{sgs}^{3/2}}{\Delta}, \tag{3.73}$$

where

$$\begin{gathered} B = \frac{2}{3} K_{sgs}\delta_{ij} - 2\,\nu_T\,\mathrm{dev}(\tilde{S_{ij}}) \\ \nu_T = C_k \sqrt{K_{sgs}}\Delta \\ \mu_T = \overline{\rho}\nu_T \\ \mu_{eff} = \mu + \mu_T, \end{gathered} \tag{3.74}$$

with the operator $\mathrm{dev}()$ indicating the deviatoric part of the tensor of interest. The constants of the model are respectively $C_k = 0.094$ and $C_\epsilon = 1.048$. An important feature of the model is reported by Kim and Menon [43]: the present model has no assumption of local equilibrium between the subgrid-scale energy production and dissipation rate. It can account for some non-local history effects which might be neglected by algebraic models.

Chapter 4

Transonic Flow Features in a NGV Passage

4.1 Problem Definition

In an aero-engine, the NGV corresponds to the stator part in a stage of a high pressure turbine. A schematic representation of the investigated zone of interest is pictured in Figure 4.1.

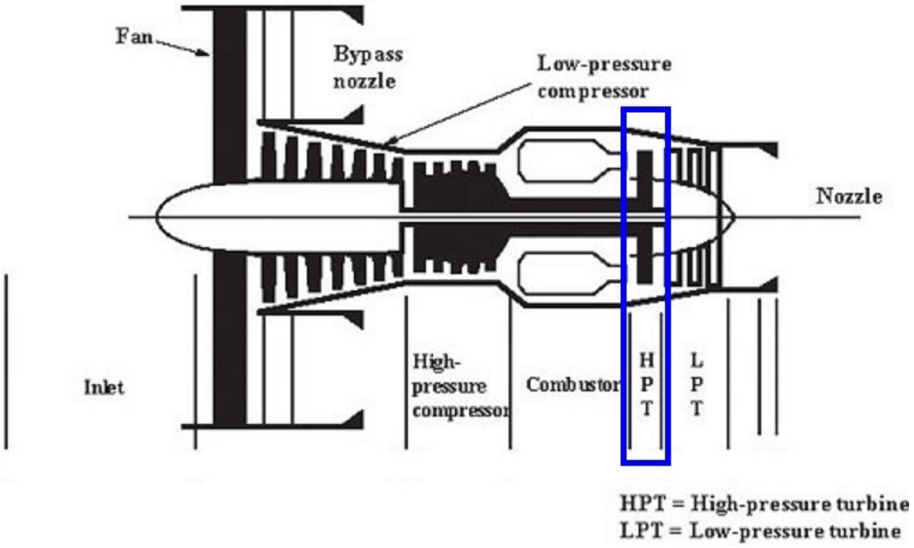

FIGURE 4.1: Schematic Representation of a modern turbofan (highlighted HPT section).

The geometry adopted in the present study consists in a simplified topology of a real NGV cascade, for which experimental data were assessed by Yasa et al. [44] in the KTH transonic test tunnel facility.

The primary aim of the experimental study was the quantification of aerodynamic kinetic energy losses, due to secondary flow structures within the vane passage. Moreover, flow measurements were carried out downstream the passage in order to characterize flow unsteadiness (e.g. vortex shedding). The experiments were conducted for both subsonic and off-design transonic conditions. At transonic conditions compressibility effects and complex flow features might arise. These features interact with each other and the main stream. Increasing the exit Mach number affects not only the shock losses but it also increases the total pressure loss downstream of the vane due to higher advection speeds [44].

4.1.1 Experimental Setup

A three-dimensional view of the real passage is presented in Figure 4.2.

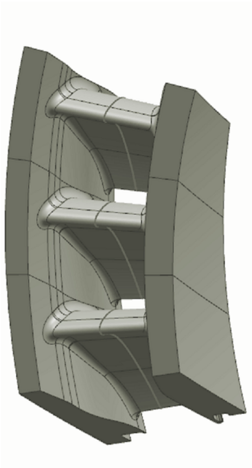

FIGURE 4.2: 3D representation of the studied NGV passage.

The vane was experimentally investigated at subsonic and transonic off-design conditions in an annular sector at the Royal Institute of Technology (KTH). The sketch of the test section with some measurement locations is depicted in Figure 4.3.

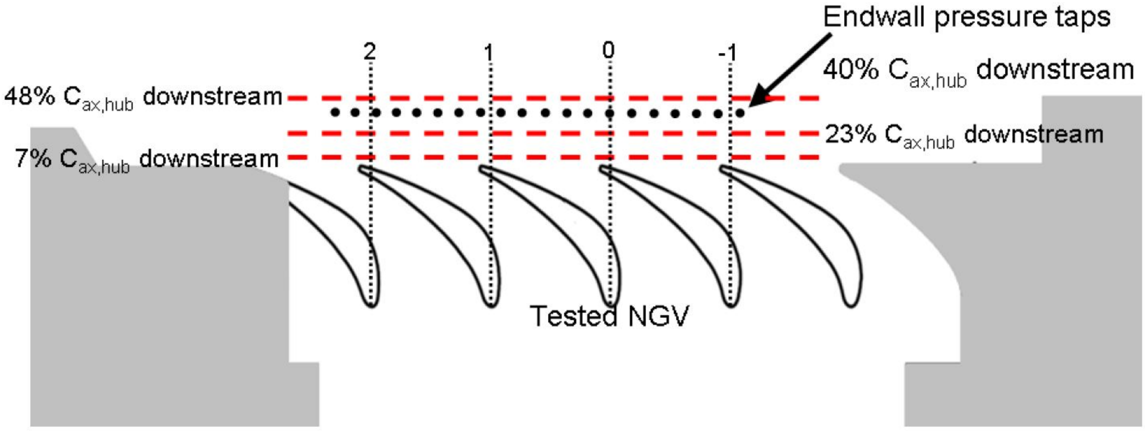

FIGURE 4.3: Test section configuration, Figure from [44].

The description of the facility is clearly addressed in the paper of Yasa *et al.* [44] and will be repeated here for the sake of clarity. The air flow is supplied by a compressor powered by a 1 MW electric motor. The compressor exhaust air temperature can vary from 300[K] to 450[K] thanks to an air cooler installed in the system. At this condition a maximum available flow of 4.7 [kg/s] is achieved at 4 [bars]. The mass flow to the facility can be controlled by two inlet valves and two bypass valves. Pressurized air enters into the settling chamber after passing by honeycomb and five mesh

TABLE 4.1: NGV main parameters

Parameter	Value	Unit
$C_{ax,\text{mid}}$	0.0657	[m]
$C_{ax,\text{hub}}$	0.0606	[m]
d	0.0022	[m]
H	0.08345	[m]

screens. The honeycomb serves as flow straightener and woven wire mesh screens enable the distribution of the airflow equally by breaking the rotating airflow caused by the fan. A transition duct is placed downstream of the settling chamber to adapt the circular cross section to the annular sector inlet section. A turbulence grid can be mounted to the upstream of the test section to vary the inlet conditions. The experiments are conducted without turbulence grid. The downstream pressure can be lowered (about 15000 [Pa]) by using two exhaust gas fans. The cascade consists of 5 airfoils and the measurements are concentrated on the flow field of the mid-NGV (phase 0). The NGV design parameters of interest for the present study are the axial chord $C_{ax,\text{mid}}$ at mid-span and $C_{ax,\text{hub}}$ at the hub, the trailing edge diameter d and the blade to blade distance at mid-span H, where the blade to blade distance represents the pitchwise distance at midspan from the leading edges of two consecutive blades. These parameters are summarized in Table 4.1.

The operating conditions of the vane have been assessed by looking at different measurements at specific locations. The inlet stagnation pressure was derived with data monitored at the settling chamber, while pneumatic taps located at $40\% C_{ax,\text{hub}}$ downstream of the trailing edge were used to setup the operating conditions [44].

The study was carried out for six different cases, each one corresponding to a different outlet pressure, from subsonic to transonic conditions. Each case is represented by the isentropic Mach number $M_{2\text{is}}$ at $40\% C_{ax,\text{hub}}$. It is defined as

$$M_{2\text{is}} = \sqrt{\frac{2}{\gamma-1}\left[\left(\frac{p_{01}}{p_2}\right)^{\frac{\gamma-1}{\gamma}} - 1\right]}, \tag{4.1}$$

where p_2 is the local static pressure and p_{01} is the inlet total pressure. The range for $M_{2\text{is}}$ goes from 0.6 to 1.2. The investigated case of the present thesis focuses on the value $M_{2\text{is}} = 0.95$.

Finally, a set of data is available from the experimental investigations; they will be used for the validation of the numerical solver described in section 3.3. They consist in the blade loading ad mid-span, the circumferential pressure distribution at $40\% C_{ax,\text{hub}}$ downstream the passage and wake measurements in terms of the total pressure ratio

$$\Pi = \frac{p_0}{p_{01}}, \tag{4.2}$$

in which p_0 is the total pressure in the location of the measurements.

For the experiments, the coordinate system defined by Glodic [45] is respected when presenting the acquired flow data.

The NGV loading (pressure) distribution is measured at mid-span location using pneumatic taps around the blade (highlighted gray line in Figure 4.2). The loading is expressed in terms of the isentropic Mach number M_{is}, which has an analogous

definition to equation (4.1). In this case the pressure p_2 is substituted with the pressure p measured on the blade. The value M_{is} is plotted versus the non dimensional distance $x/C_{ax,\text{mid}}$, where the x-direction is aligned with the flow at the inlet.
The experimental pressure readings on the blade are presented in Figure 4.4.

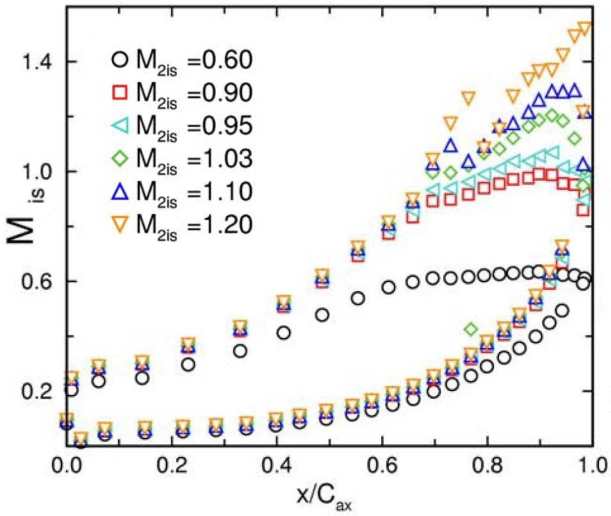

FIGURE 4.4: Blade loading in terms of the isentropic Mach number M_{is} at different operating conditions, Figure from [44].

The circumferential pressure distribution data were acquired at a distance $40\% C_{ax,\text{hub}}$ downstream the NGV, corresponding to the discharge plane of the passage, where $M_{2,\text{is}}$ is defined. Pneumatic taps were used to collect pressure measurements. Once again they are expressed in terms of the isentropic Mach number. Figure 4.5 shows the collected readings along the vane phase.

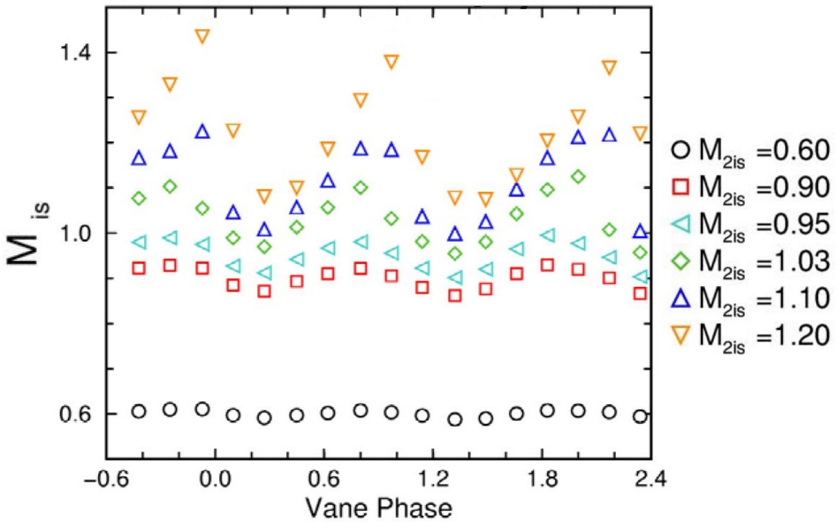

FIGURE 4.5: Circumferential pressure distribution in terms of the isentropic Mach number M_{is} at different operating conditions, Figure from [44].

Finally, a 5-hole Pitot tube with a Kulite sensor is used for total pressure and unsteady flow measurements downstream the passage. Total pressure ratio profiles were collected at several locations. The present study will refer to the two locations at $7.1\%C_{ax,\text{hub}}$ and $48.4\%C_{ax,\text{hub}}$ downstream. The profiles are available in an exhaustive internal report [46]. They are represented in Figure 4.6.

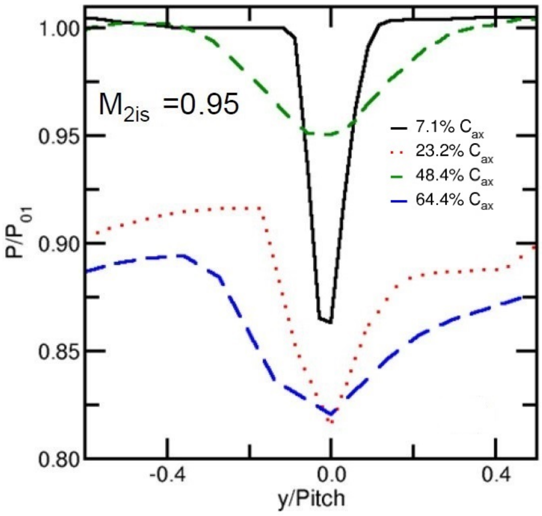

FIGURE 4.6: Total pressure profiles at different downstream locations (as in the legend), Figure from [46].

Experimental unsteady data were also acquired for the characterization of vortex shedding. The shedding frequency found by Yasa *et al.* is equal to 19.7 [kHz] for the subsonic design case, while it increases up to $21 - 22$ [kHz] for higher velocities [44].

4.2 Baseline Case

The geometry adopted in the present study consists in a simplified topology of the real NGV passage.

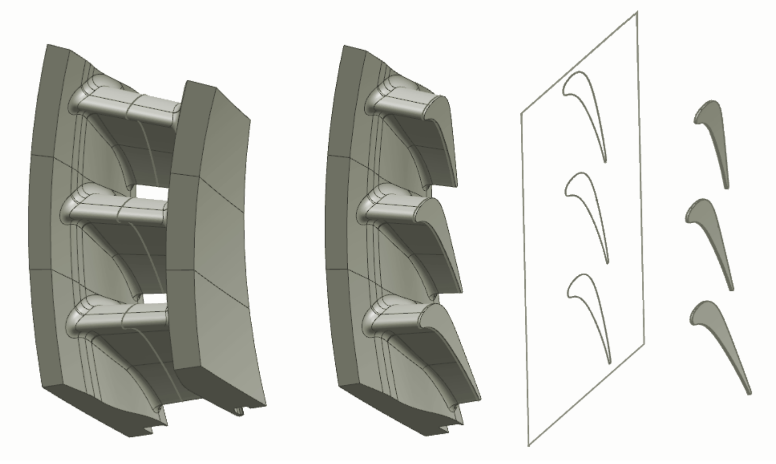

FIGURE 4.7: Three-dimensional CAD geometry and simplified manifold.

The baseline case refers to numerical simulations reproducing only the transonic off-design condition of the experiments.

The validation of the numerical solver settings against the available experimental data consists in the starting point for evaluating the indirect combustion noise mechanism on the same simplified topology.
The simplified model is a two-dimensional manifold of the blade geometry at mid-span: i.e. the real geometry was cut by a cylindrical front at mid-span and then projected onto a plane. This approximation can be made when the height of the annulus enclosing the guide vanes is small compared to the inner radius of the cascade [47]. In the current model the annulus height is one order of magnitude lower than the inner radius, justifying the use of the linear cascade topology.
The CAD model was realized with the SIEMENS-NX software. First, three vanes were assembled in order to reproduce the real geometry of the passage, as illustrated in Figure 4.2. Then a sectioning cylindrical front was constructed; the front sectioned the three vanes at a radial distance corresponding to the mid-span. Finally, the mid-section profiles were projected on a plane; the plane was parallel to the tangent surface of the central cut blade. The linear cascade model is hence obtained.
A schematic representation of the procedure is illustrated in Figure 4.7.

4.2.1 Computational Domain and Mesh

At this point, the geometry of the fluid domain and the respective mesh have been created. The adopted procedure was to consider the central unwrapped airfoil on the planar surface and to construct a smart block structure around it. This strategy, which consists of only one single passage, simulates an infinite linear cascade (along the projected circumferential direction). The front view of the domain, together with the reference frame are depicted in Figure 4.8.

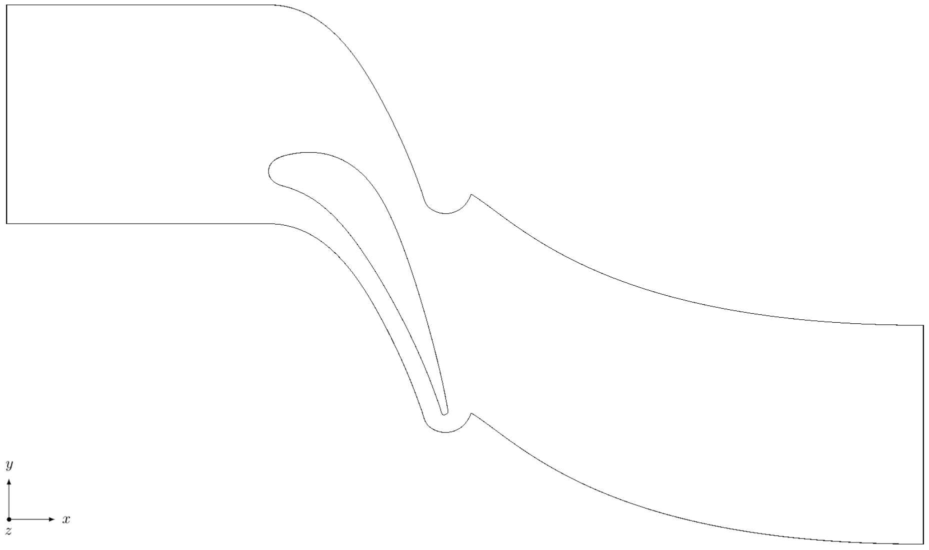

FIGURE 4.8: Front view of the computational domain.

In order to apply periodic boundary conditions, the lower and upper boundaries of the domain in Figure 4.8 have to satisfy one constraint: i.e. the spatial discretization along the tangential direction of the edges must be exactly the same. Moreover, the height between the lower and upper boundary must correspond to the blade-to-blade distance H. This outer block revealed itself particularly suitable for such task. The final internal blocking structure was build via ICEMCFD®, which allows the creation of structured *hexa*-meshes[1]. Structured grids are highly space efficient, exhibit good convergence and have high spatial resolution [48]. These cells can be arbitrarily aligned along the local flow direction, capturing flow gradients in a very accurate manner. It is important, therefore, to align the cells vertical edges along the wall-normal direction of the airfoil, such that the boundary layers are accurately resolved. It is also desirable that the edges of two neighboring cells exhibit the lowest non-orthogonality.

The internal blocking structure (18 blocks) with the respective boundaries is depicted in Figure 4.9.

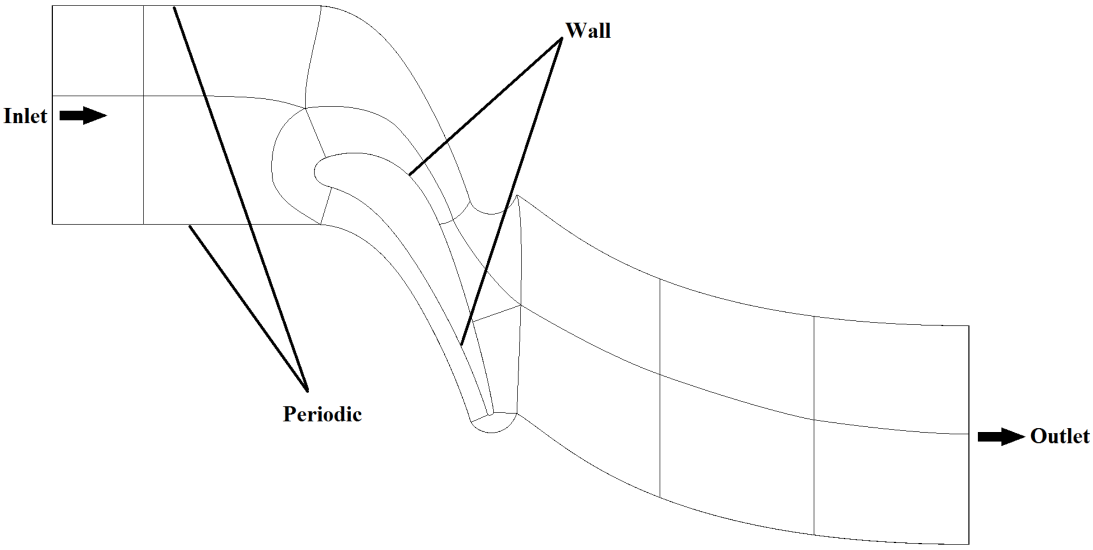

FIGURE 4.9: Internal blocking strategy, two-dimensional front view.

The next step is to create the two-dimensional mesh that will then be extruded in the spanwise direction (z-direction in Figure 4.8). The choice of the height of the first cell around the airfoil (wall) is also crucial: it has to be sufficiently small in order to resolve the boundary layer features correctly and in the present work the use of wall function for turbulence modeling is avoided. The near wall normal distance is characterized by the non-dimensional parameter Δy^+. This distance depends on some other parameters and the next phase is to determine them.

Another important dimensionless number is the Reynolds number, crucial for the characterization of turbulence (defined in section 3.4). In this particular setup the Reynolds number is based on sonic conditions of the baseline simulation: assuming a polytropic ideal gas behavior of the fluid and isentropic flow, the relation between total temperature T_0 and static temperature T is

$$\frac{T_0}{T} = 1 + \frac{\gamma - 1}{2} M^2, \tag{4.3}$$

---

[1] A hexahedron (often called *hexa*) is a topological cube with 8 vertices, 12 edges and 6 quadrilateral faces.

where γ is the specific heat ratio and M is the Mach number defined as the ratio between the modulus of the flow velocity $||\mathbf{u}||$ and the speed of sound c.

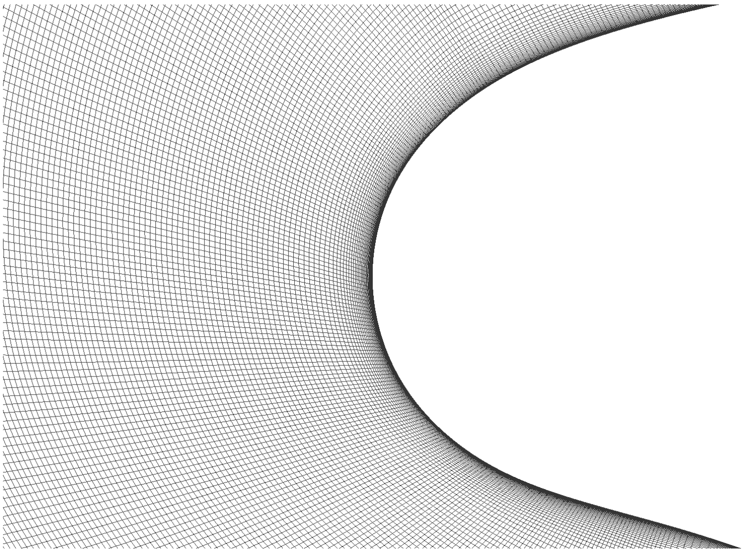

(A)

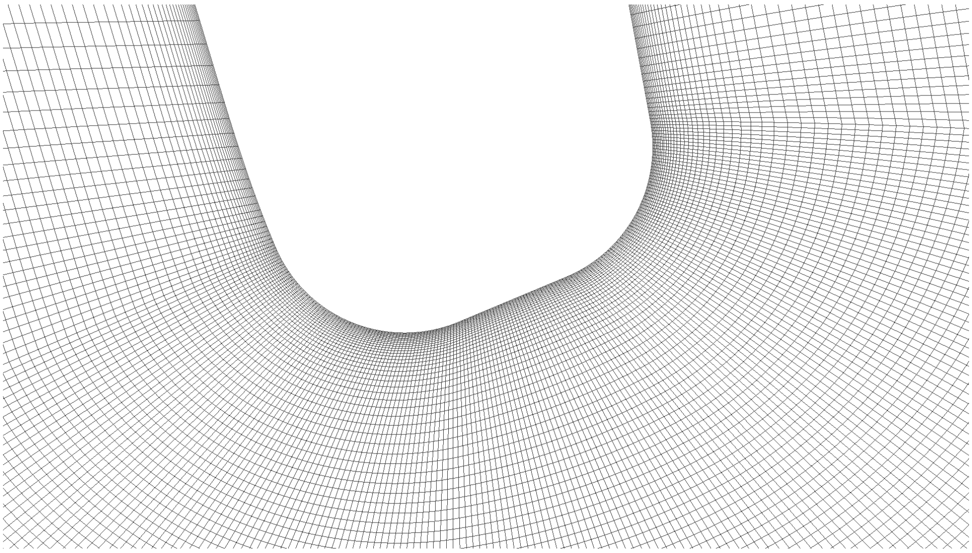

(B)

FIGURE 4.10: Mesh Details, leading edge (A) and trailing edge (B) views.

Then, at sonic conditions[2], it results $M = 1$ and $T_0/T^* = 1.2$ for the specific heat ratio $\gamma = 1.4$. Recalling the definition of speed of sound and the perfect gas model, it results

$$c^2 = \frac{\partial P}{\partial \rho}\Big|_s = \gamma RT. \tag{4.4}$$

For the baseline simulation the inlet total temperature will correspond to $T_0 = 304.51$[K], leading to a sonic temperature $T^* = 253.76$ [K] and to a speed of sound $c = 319.33$

---

[2] Usually indicated with superscript *.

[m/s]. The definition of the Reynolds number at sonic condition is then

$$Re^* = \frac{\rho^* U^* L}{\mu^*} = \frac{\rho^* c\, C_{ax,\mathrm{mid}}}{\mu^*}. \tag{4.5}$$

Using again isentropic relations and the thermodynamic model for the polytropic ideal gas, the resulting Reynolds number is $Re^* \approx 10^6$. The Reynolds number is large enough to consider the flow turbulent. Through empirical relations the skin friction coefficient can be evaluated for the flow of interest. Its definition is

$$C_f = \frac{\tau_w}{\frac{1}{2}\rho (U^*)^2}, \tag{4.6}$$

where here τ_w is the wall shear stress at sonic conditions defined as

$$\tau_w = \mu^* \frac{\partial u_{//}}{\partial y}\bigg|_{y=0}, \tag{4.7}$$

in which $u_{//}$ is the velocity component parallel to the wall.
For the skin friction coefficient estimation the $1/7$ power law with experimental calibration [49] will be used:

$$C_f = 0.0592\, (Re^*)^{-1/5}. \tag{4.8}$$

Then the wall shear stress can be calculated and the friction velocity u_τ is found by

$$u_\tau = \sqrt{\frac{\tau_w}{\rho^*}}. \tag{4.9}$$

Finally, aiming for a non-dimensional wall distance $\Delta y^+ \approx 1$, it results from the definition of Δy^+

$$\Delta y = \frac{\mu^* \Delta y^+}{\rho^* u_\tau} = \frac{\mu^*}{\rho^* u_\tau}. \tag{4.10}$$

The first cell height was finally set to $\Delta y = 5e^{-6}$ [m]. A posteriori evaluations on the numerical solution showed that this value corresponds to an average $\Delta y^+_{\mathrm{avg}} \approx 5$. A detail of the mesh at the leading and trailing edge can be visualized in Figure 4.10.
Finally, the 2D mesh is extruded for a number of 75 layers in the spanwise direction in order to represent correctly the three-dimensional features of turbulence. The depth of the cells in the z-direction is set based on an estimation of the transverse Taylor micro-scale

$$\lambda_g = \sqrt{\frac{10\mu^* L}{\rho^* k^{1/2}}} = \sqrt{\frac{10\mu^* C_{ax,\mathrm{mid}}}{\rho^* k^{1/2}}}. \tag{4.11}$$

The total number of elements is $n_{\mathrm{elems}} = 739500 \times 75 = 55462500$. The final mesh characteristics are summarized in Table 4.2.
Sponge zones with gradual grid stretching are used at the inlet and at the outlet boundaries in order to damp spurious reflections.
The mesh was hence exported in the *foam-extend* framework for the set-up of the numeric calculations.
Once exported, the mesh required the specification of periodic boundaries. Therefore the upper and lower boundaries of the domain were grouped together in the single patch *PERIODICUPDOWN* via the command *createPatch* (with its respective dictionary *createPatchDict*)[3]. The same procedure has also been applied to the left

---

[3] A reference for the procedure details can be found in `https://openfoamwiki.net/index.php/CreatePatch`

TABLE 4.2: Mesh characteristics

Parameter	Average	Maximum
Δy^+	5	8
Non-Orthogonality	22[°]	53.8[°]
Aspect Ratio	< 30	49.4
Δx^+	$15\Delta y^+_{\text{avg}}$	–
Δz^+	$20\Delta y^+_{\text{avg}}$	–

and right boundaries (the lateral boundaries in the spanwise direction), resulting in the single periodic *LEFTRIGHT* patch. The periodic boundary conditions in the lateral patches of the domain are used to represent a blade of infinite span.

4.2.2 Initial Conditions

The initial conditions for the baseline case consist on the solution of the Reynolds Averaged Navier-Stokes equations (with Favré averaging) on the two-dimensional domain representing the vane passage. The field is initialized with an internal velocity $\mathbf{U}_{\text{int}} = (52.35, 0, 0)^T$[m/s], an internal static pressure $p_{\text{int}} = 104370$[Pa] and an internal static temperature $T_{\text{int}} = 303.15$[K]. The internal values for velocity and temperature correspond to the inlet velocity $\mathbf{U}_1 = (M_1 c_1, 0, 0)^T$ and to the static temperature T_1 from the experimental operating conditions. The internal static pressure correspond to the static pressure p_{out} at discharge of the vane, also from experimental operating conditions. The fluid is considered to be a polytropic ideal gas with

$$\gamma = \frac{c_p}{c_v} = \frac{7/2R}{5/2R} = \frac{7}{5}. \tag{4.12}$$

4.2.3 Boundary Conditions

The boundary conditions for both the RANS and LES simulations are summarized as following:

- **No slip adiabatic wall**, for the blade; i.e. $\mathbf{U}_{\text{wall}} = (0, 0, 0)^T$ and $\nabla T \cdot \mathbf{n}|_{\text{wall}} = 0$.
- **Average static pressure outlet**, set equal to $p_{\text{out}} = 104370$[Pa]. This "weaker" condition for the outlet static pressure is commonly used for turbomachinery applications since the value of static pressure across the entire outlet is not precisely monitored and controlled during experimental readings. Moreover, the *fixedMean* boundary condition, which is used in *foam-extent*, extrapolates field to the patch using the near-cell values and adjusts the distribution to match the specified, optionally time-varying, mean value [4]. This takes into account the fact that a non stationary wake can exit the fluid domain.
- **Stagnation inlet** , Total pressure and total temperature are specified, their values are respectively $p_{01} = 187100$[Pa] and $T_{01} = 304.51$[K]. The total pressure corresponds to the one matching the effective experimental condition. The total temperature is estimated from the static value $T_1 = 303.15$[K] specified in the experiments and the inlet Mach number $M_1 = 0.15$ through isentropic

---

[4] `http://www.openfoam.com/documentation/user-guide/standard-boundaryconditions.php`.

relation (4.3). The specification of total conditions is widely used in turbomachinery and internal flows. Furthermore, the specification of stagnation properties at the inlet and static pressure at the outlet consists in a well-posed set of boundary conditions for the problem of interest. Hence the velocity at the inlet is not specified. In *foam-extend* the boundary condition *pressureInletOutletVelocity* can be applied to patches where the total pressure is specified. It calculates directly the velocity from the mass flux entering in the domain, normal to the inlet boundary.

- **Periodic upper-lower boundaries**, the *cyclic* boundary conditions is applied to enforce a periodic condition between the upper and lower pair of boundaries enclosing the fluid domain. This condition simulates an infinite linear cascade.
- **RANS left-right boundaries**, for the solution of the RANS, the lateral patches are specified as *empty*, due to the two-dimensional nature of the problem and the 2D fluid domain adopted.
- **LES periodic left-right boundaries**, for the solution of the LES, the *cyclic* boundary conditions is applied to enforce a periodic condition between the lateral pair of boundaries enclosing the fluid domain. This condition simulates the effect of a blade of infinite span. Hence, the lateral patches are specified as physical boundaries with translational periodicity in the spanwise direction.

In addition, a turbulence intensity of $I = u'/U = 1\%$ was specified at the inlet for the calculation of the RANS solution; where u' is the root-mean-square of the turbulent velocity fluctuations and U is the mean velocity (in this case the module of the inlet velocity U_1).

4.3 Results

The numerical results obtained with the numerical set-up of the baseline case are shown in the present section with the aim of understanding the transonic flow features in the vane passage. Moreover, probes sampling lines and 2D front slices or planes of the fluid domain are placed in the domain in order to compare numerical results with experimental data and to allow a comprehensive post-processing of the results.

4.3.1 Flow Features

Figure 4.11 shows the instantaneous Mach number field for a two-dimensional slice defined by the spanwise z-direction normal.

The flow is subsonic at the inlet of the domain and the local Mach number is equal to $M_1 = 0.15$, corresponding to the velocity of $U_1 = 52.35$ [m/s] which matches the experimental conditions. Then the flow is accelerated up to sonic condition at the throat of the nozzle guided vane passage (at $x/C_{ax,\mathrm{mid}} \approx 0.75$). Passed the throat the flow interacts with compression and expansion waves emitted from the shed vortices at the trailing edge, as shown in Figure 4.13. These waves are also impinging on the suction side of the blade and then are reflected back towards the normal direction of the surface. The flow accelerates further on the suction side due to a Prandtl-Mayer expansion. Almost at the end of the suction side, it is possible to observe compressibility effects: a system of weak shocks interacting with the wake is present throughout the final part of the suction side. By looking at the animation

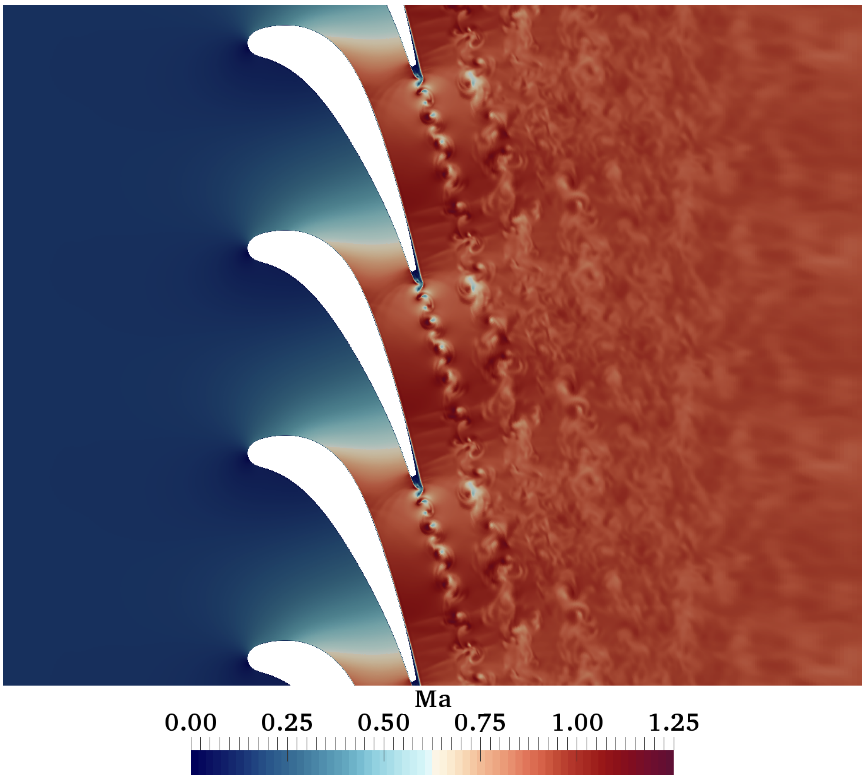

FIGURE 4.11: Instantaneous Mach number field.

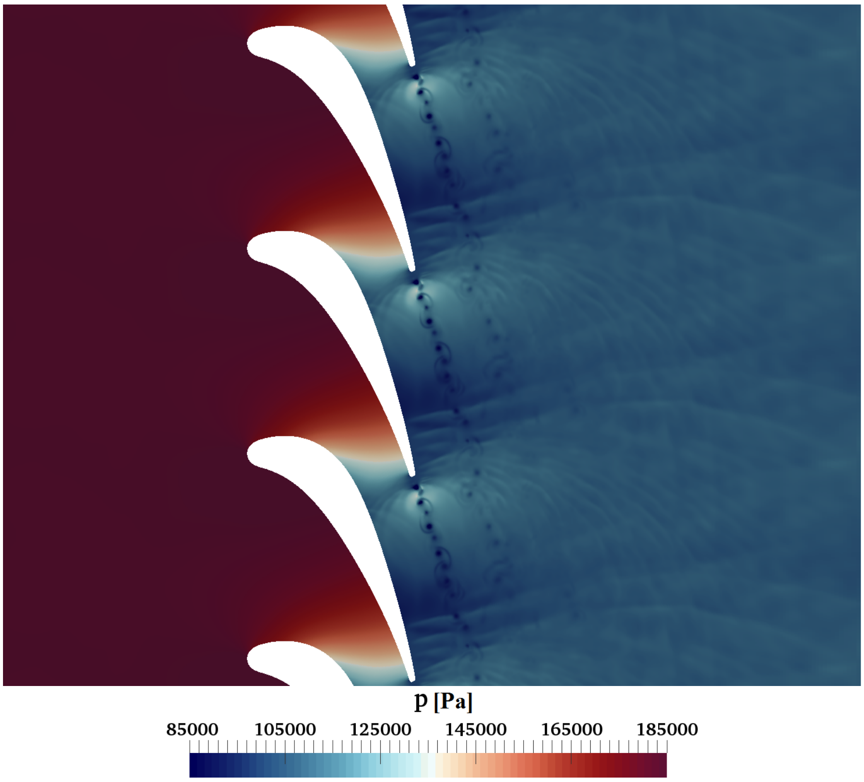

FIGURE 4.12: Instantaneous pressure field.

corresponding to Figure 4.13, it seems that the system of weak shocks is moving with a characteristic dynamics.

The pressure waves' pattern emitted from the shed vortices can be seen more in the instantaneous pressure field in Figure 4.12. Moreover, an overall Von Karman vortex street-like pattern is visible in both figures of the Mach number and the pressure field. This trend starts directly from the rounded trailing edge and last until an axial distance corresponding to $x/C_{ax,\mathrm{mid}} = 0.2$ downstream the blade, then the overall two-dimensional organization starts to break down in smaller and less organized eddies. This is further corroborated by the flow depicted in Figure 4.13.

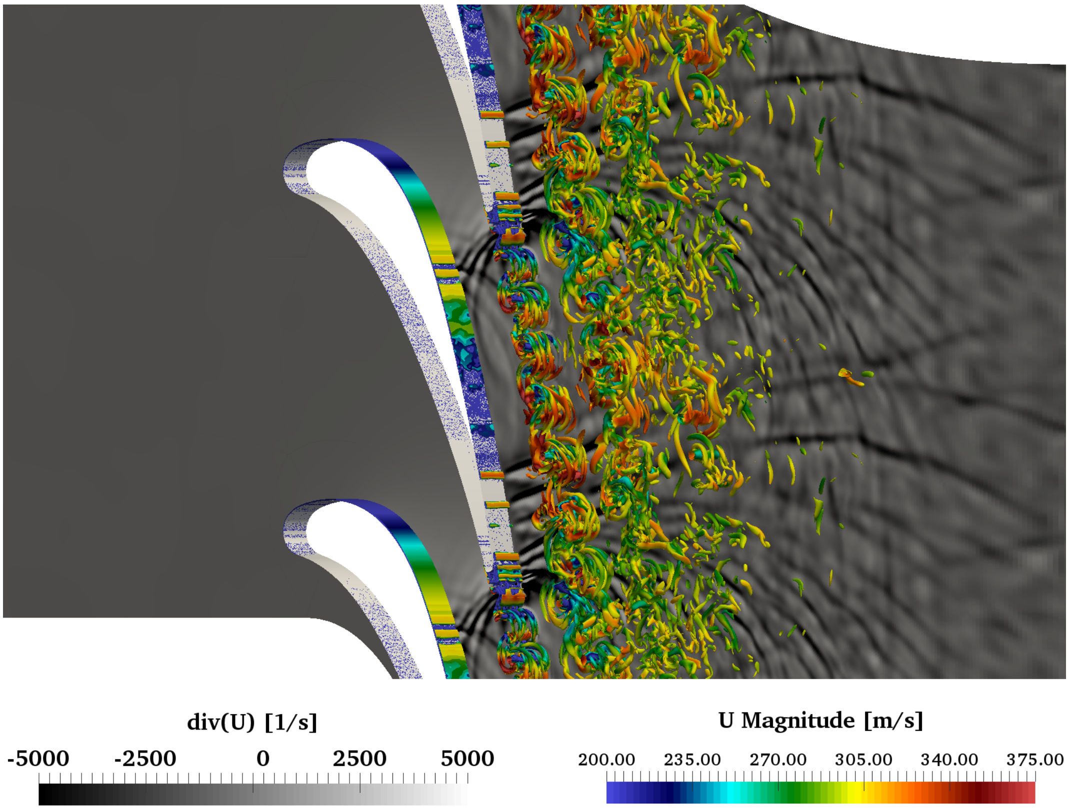

FIGURE 4.13: Isocontours of Q-criterion (coloured with the velocity magnitude) superimposed on the divergence of the velocity field.

Turbulent structures in the spanwise direction are three-dimensional. Thus, the selected discretization in the spanwise direction is able to capture the correct three-dimensional features of turbulence. In the first part of the wake 3D structures are also present but their organization form the overall 2D vortex street.

The shedding frequency predicted by the 3D LES is of $f_s = 24$ [kHz], corresponding to a Strouhal number of $St_s = f_s d/U = 0.176$. The Strouhal number is calculated with the length scale $d = 0.0022$ [m] being the trailing edge diameter and the velocity scale U being equal to the one calculated from the exit Mach number of 0.95. The shedding frequency found experimentally [44] was equal to $21 - 22$ [kHz] for this operating condition.

The mean (time-averaged) pressure distribution and the mean total pressure ratio Π are shown in Figure 4.14. The time average and statistics were calculated over a time series corresponding to a period of time $t_{\mathrm{sim}} \approx 200 t_s$, where t_{sim} is the real time length of the simulation $(0.0083$[s]) and $t_s = 1/f_s$ is the shedding period

$(1/24000 = 4.17e^{-5}[\mathrm{s}])$.

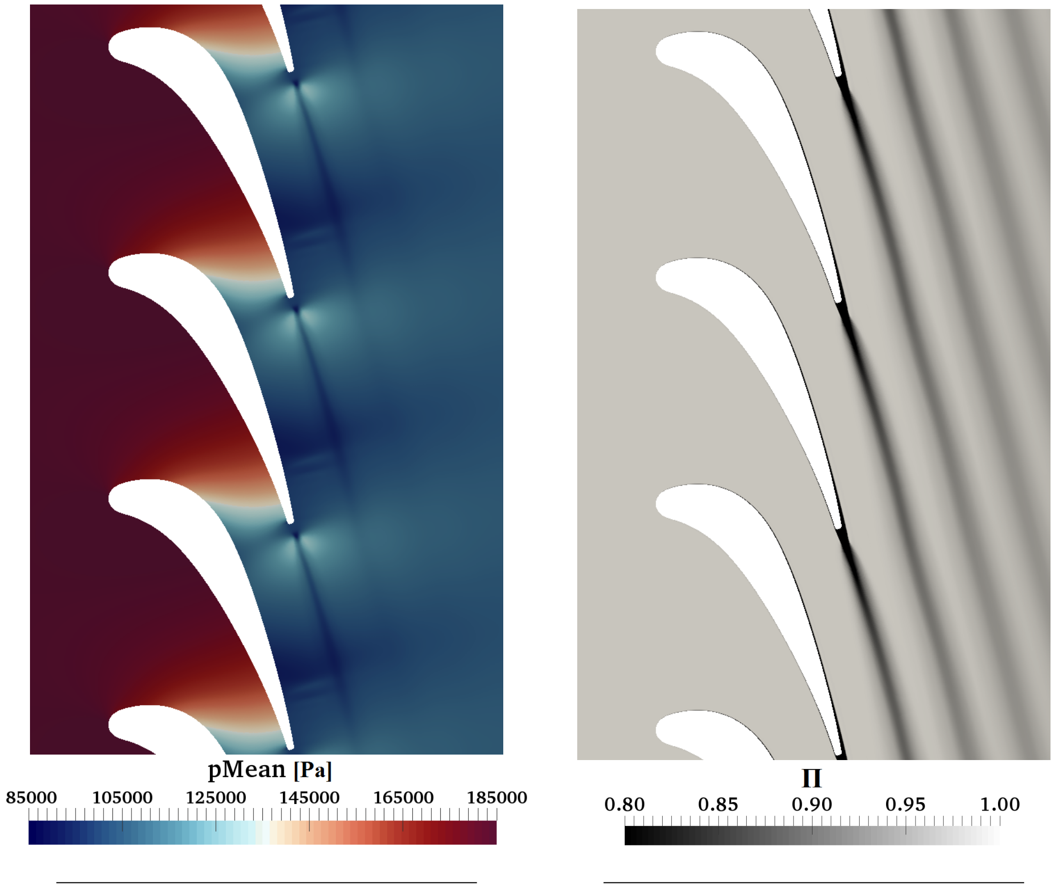

(A)

(B)

FIGURE 4.14: Time averaged pressure distribution (A) and total pressure ratio (B).

The wake region is clearly visible in both figures. Moreover, the pressure distribution shows the presence of a weak shock on the suction side towards the end of the blade. The shock is not visible, instead, in the averaged total pressure distribution. It is also worth to notice the direction of the wake: in both fields of Figure 4.14 the first part of the wake seems to curve slightly; after passing the trailing edge, the wake straightens itself and proceeds downstream the cascade.

4.3.2 Comparison With Experiments

The results from the 2D RANS (used for the initialization) and the 3D LES are now compared with the experimental data.
First, the NGV blade loading at mid-span and the circumferential pressure distribution are presented in terms of the isentropic Mach number M_{is}

$$M_{\mathrm{is}} = \sqrt{\frac{2}{\gamma - 1}\left[\left(\frac{p_{01}}{p}\right)^{\frac{\gamma-1}{\gamma}} - 1\right]}, \tag{4.13}$$

in which p is the local time averaged pressure.
The blade loading is expressed as a function of the axial normalized coordinate $x/C_{ax,\mathrm{mid}}$, while the circumferential pressure distribution is expressed as a function

of the vane phase (as in the experiments).
Figure 4.15 shows the mid-span slice of the numerical fluid domain where the time averaged quantities to compare where obtained.

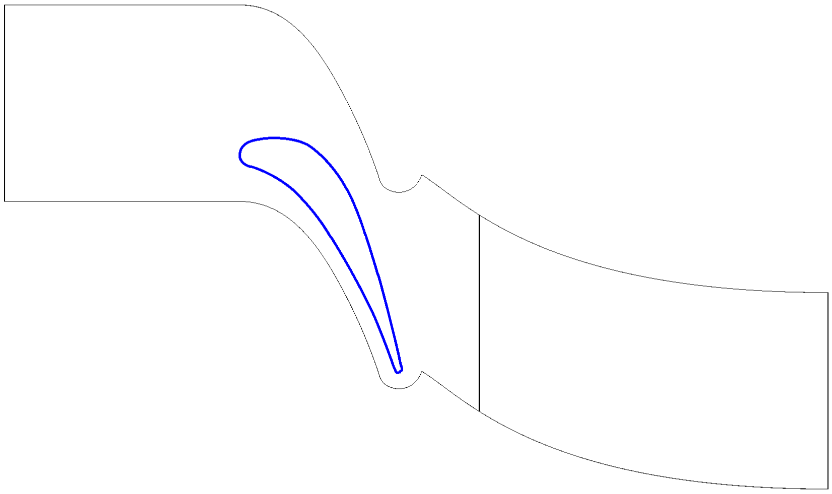

FIGURE 4.15: Location of NGV loading (blue) and circumferential pressure distribution (black) data collection.

The comparison with the experiments can instead be visualized from Figure 4.16.

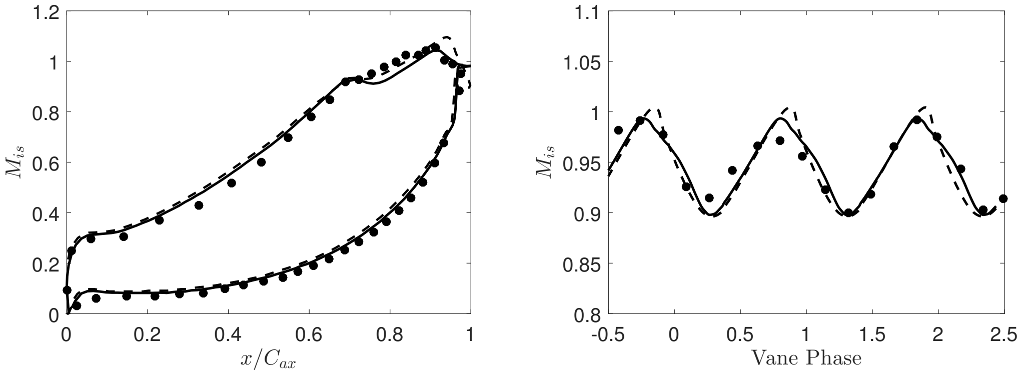

(A)

(B)

FIGURE 4.16: NGV blade loading (A) and circumferential pressure distribution (B); (●) experimental data; (- -) 2D RANS; (—) 3D LES.

For the pressure side, notably, a very good agreement is found between the experiments and both numerical simulations. The matching is also good on the suction side, with a slight underprediction after the throat region. The pressure distribution along the blade involves different features due to the physics of the flow field. On the pressure side the flow is accelerated up to sonic conditions at almost the end of the blade; the entire pressure sides behaves like a converging portion of a nozzle. On the suction side, the flow accelerates up to chocking conditions until $x/C_{ax,\text{mid}} = 0.75$. Finally, the Mach number is increased due to an expansion on the final part of the blade. Then the Mach number drops just below sonic conditions due to the presence

of a weak normal shock at approximately $x/C_{ax,\mathrm{mid}} = 0.95$. The location of the shock is just slightly overpredicted by the 2D RANS.
Regarding the circumferential pressure distribution, the topology of the domain allows, by construction, to reproduce only one passage, and the subsequent resulting trend is periodic. The experimental data are available for almost three complete passages. It can be noticed that the LES result are in perfect agreement in phase 2; 2D RANS also show a good agreement in that region. The experimental results are not perfectly periodic in the pitchwise direction.
Then, the experimental wake losses in terms of the total pressure ratio Π (4.2) are compared with the results of the numerical simulations. The locations of the measurements are two planes respectively at $7.1\%C_{ax,\mathrm{hub}}$ and $48.4\%C_{ax,\mathrm{hub}}$ downstream the NGV. Again the location of the measurements' plane at the mid-span slice can be visualized in Figure 4.17.

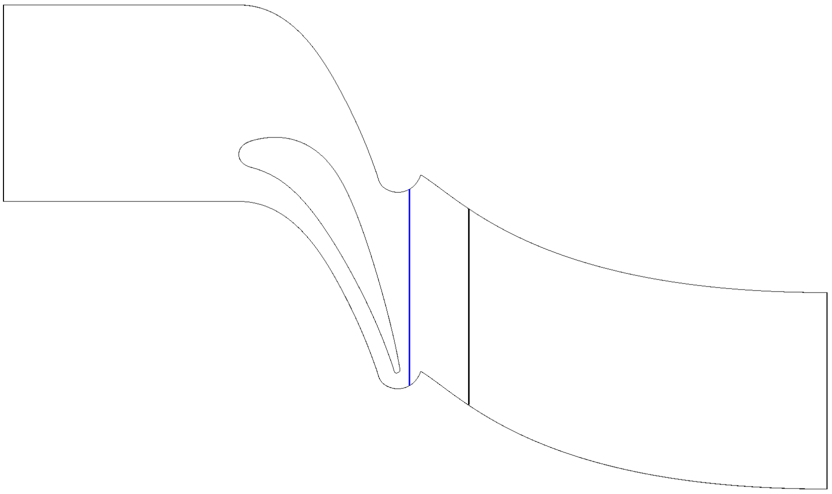

FIGURE 4.17: Downstream location of total pressure losses data collection; $7.1\%C_{ax,\mathrm{hub}}$ (blue), $48.4\%C_{ax,\mathrm{hub}}$ (black).

The wake losses profile are shown in Figure 4.18.
The increasing wake region extension downstream the NGV passage can be clearly seen from the pictures. The total pressure losses are also reduced thanks to the enhanced mixing in the wake region. The asymmetric profile at the closest location to the trailing edge is very well captured by the 3D LES. The resulting profile from the 2D RANS appears slightly more symmetric. In the furthest location, the 3D LES exhibits a closer profile to the experimental data than the 2D RAND; where the wake width is underpredicted. Overall, a very good agreement is found for both LES and RANS results in terms of wake width at $7.1\%C_{ax,\mathrm{hub}}$ downstream the passage. Instead, at $48.4\%C_{ax,\mathrm{hub}}$, the LES results agree better with experimental data than the RANS ones.
Regarding the maximum pressure losses, both simulation results overpredict them at $7.1\%C_{ax,\mathrm{hub}}$, while the LES results are closer to the experimental ones at $48.4\%C_{ax,\mathrm{hub}}$.

4.3.3 Space-Time Correlations

In order to evaluate the convection speed of the turbulent structures in the wake, points were sampled along the wake at the mid-span of the numerical fluid domain.

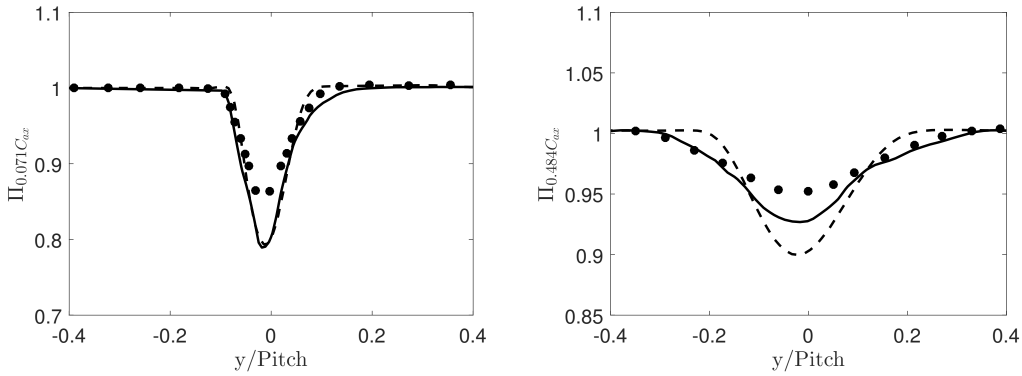

(A) (B)

FIGURE 4.18: Total pressure ratio at different downstream locations: $7.1\%C_{ax,\text{hub}}$ (A) and $48.4\%C_{ax,\text{hub}}$ (B) ; (●) experimental data; (- -) 2D RANS; (—) 3D LES.

The direction of the line was chosen accordingly to the discharge direction $\theta_2 = 75[°]$ of the vane. The zone of interest can be visualized in Figure 4.19. The probes sampled the signal of the three velocity components (u, v, w). Then the two-dimensional velocity magnitude along the direction θ_2 was calculated as

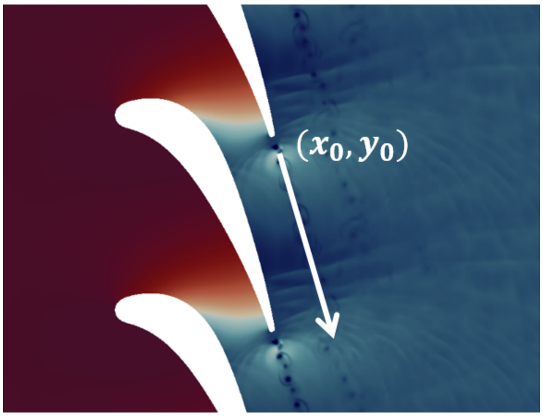

FIGURE 4.19: Sampling line along the wake for the evaluation of space-time correlations, 75 points starting from $(x_0, y_0, \overline{z}_{\text{mid}})$.

$$U_v = u\sin(\theta_2) - v\cos(\theta_2), \tag{4.14}$$

and its fluctuating part was taken as $U_v' = U_v - \overline{U_v}$.

The general cross correlation coefficient for two locations and two times is defined as

$$R(\mathbf{r}, \Delta t) = \frac{\langle U_v'(\mathbf{x}, t_0) U_v'(\mathbf{x} + \mathbf{r}, t_0 + \Delta t)\rangle}{\sqrt{U_v'(\mathbf{x}, t_0)^2}\sqrt{U_v'(\mathbf{x} + \mathbf{r}, t_0 + \Delta t)^2}}. \tag{4.15}$$

Figure 4.20 shows the aforementioned correlation coefficient taking as reference point $\mathbf{x}$ the coordinates (x_0, y_0) and as reference time the instant $t_0 = 0$.

The spatial distance in the figure corresponds to the length of the sampling line and was adimensionalized by the trailing edge diameter d, while the time scale was made non-dimensional by using the following definition $\tau^* = tU/d$, where U is

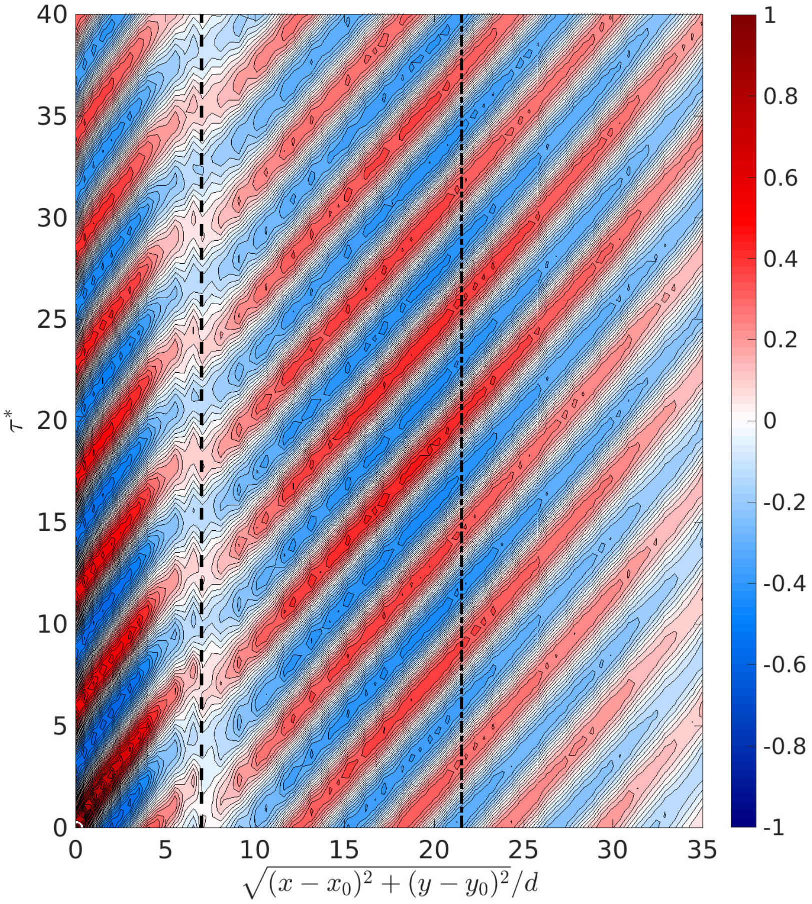

FIGURE 4.20: Cross correlation coefficient for two locations and two times; reference point (x_0, y_0) at $t_0 = 0$.

again the velocity calculated from $M_{\text{is}} = 0.95$.

Two lines are also marked in Figure 4.20. The line which is furthest downstream represents the location where the convected voritces first pass through the system of shocks. There is no drastic change in slope in the isosurfaces of the correlation coefficient.

The line closest to the reference point, instead, shows a region where the correlation coefficient drops. It also shows a change of phase in the correlation between the vortical structures which pass across it.

Then, the same correlation coefficient was calculated with two generic reference points on the sampled line at a generic time instant $\bar{t}$. The first point was taken 15 trailing edge diameters downstream the point (x_0, y_0) while the second one 34 diameters downstream. The resulting correlation isocontours for the first point are depicted in Figure 4.21.

Instead, the resulting correlation isocontours for the second point are shown in Figure 4.22.

Finally, the convection velocity of the turbulent structures is evaluated following the maximum value of the correlation coefficient in the space -time diagram. This velocity is simply estimated by the ratio $dist_{\max}/\Delta t$, where $dist_{\max}$ is the distance along

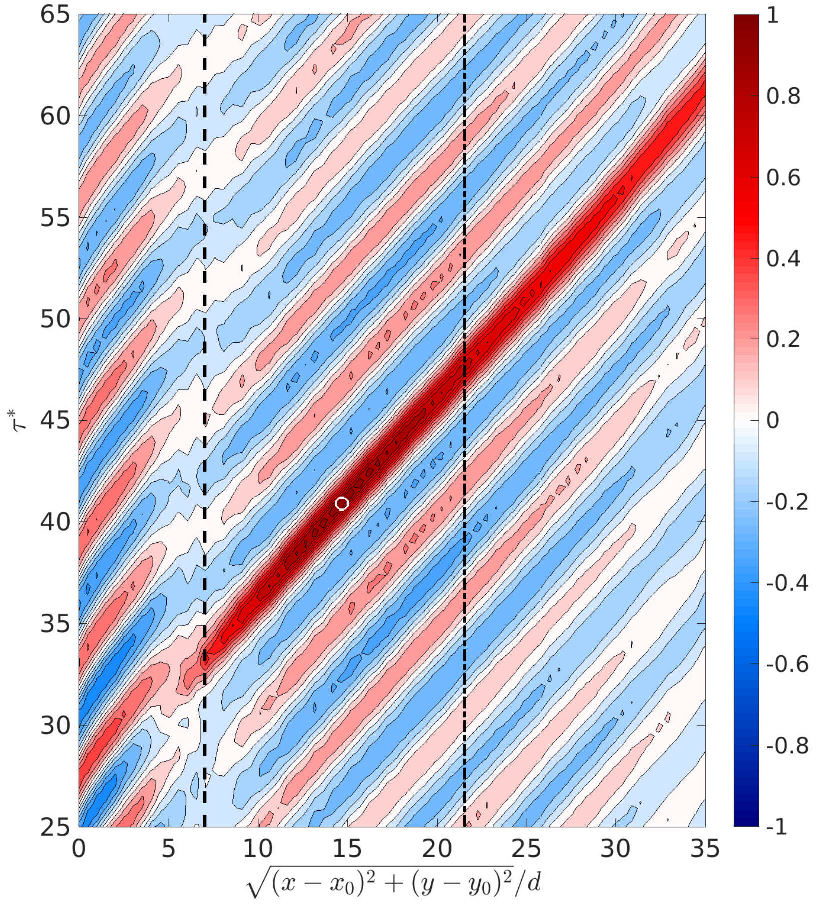

FIGURE 4.21: Cross correlation coefficient for two locations and two times; reference point 15 trailing edge diameters downstream the point (x_0, y_0) at $t_0 = \bar{t}$; white circle → reference point.

the sampled line separating two maxima of the correlation R and Δt is the time interval between them.

From the two Figures 4.21 and 4.22 it might seem that the velocity of the vortical structures might change across the shock. Instead it was found that the convection velocity is constant throughout the sampled line. This is shown in Figure 4.23, where the convection velocity is expressed in terms of the ratio U_v/U.

Figure 4.23a shows the convection velocity estimation before the vortical structures change of phase. Figure 4.23b shows its estimation from the reference point 15 diameters downstream to the final point 34 diameters downstream.

Overall strong correlations were found for the velocity signals sampled for the simulation, underling a global organization of the vortices along the discharge direction of the vane. In Figures 4.20, 4.21 and 4.22 a strong temporal periodicity is observed on the ordinate axis τ^*, with a separation $\Delta\tau^* = 5.68$, corresponding to the shedding frequency f_s.

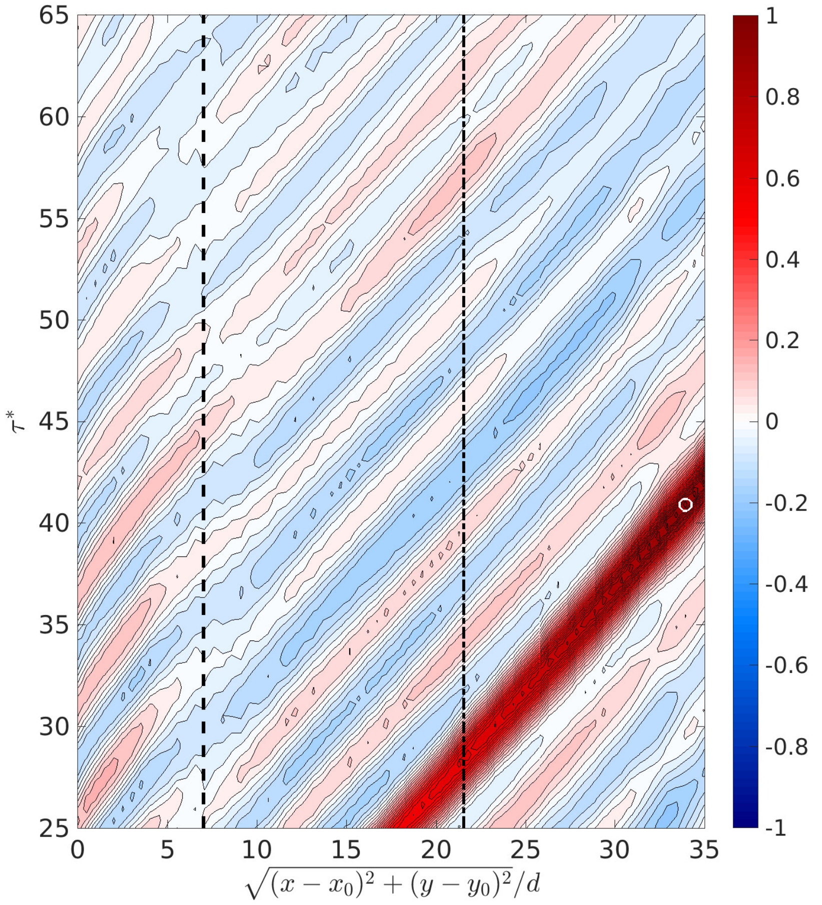

FIGURE 4.22: Cross correlation coefficient for two locations and two times; reference point 34 trailing edge diameters downstream the point (x_0, y_0) at $t_0 = \bar{t}$; white circle → reference point.

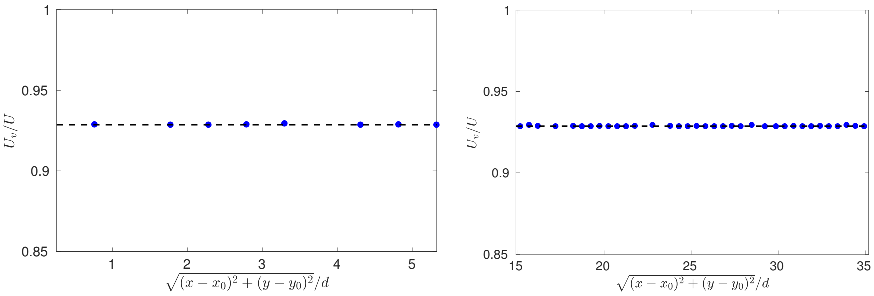

(A)

(B)

FIGURE 4.23: Convection velocity estimated along the sampled line; before the phase change (A), after the phase change (B).

Chapter 5

Indirect Combustion Noise

5.1 Fluctuating Inlet Temperature

After validating the solver settings with the baseline case, for which experimental results were available, the aim of the present work is to assess (numerically) the generation mechanism of indirect combustion noise, that is to observe the entropy to acoustic conversion of inflow disturbances through the NGV passage.

Hot and cold spots of air coming from the combustion chamber will be imposed as a planar sinusoidal wave train coming from the inlet boundary.

First, a similar numerical setup to the baseline case will be adopted for the "*forced*" scenario, with the only difference being the forcing (not-uniform) temperature at the inlet. The frequency content and the acoustic response of the blade row will be analyzed for both cases in order to observe the effects of the forcing.

Then, the effect of changing the inlet total temperature will be studied with the aim of simulating more realistic scenarios and to address the effects on the NGV acoustic response.

5.1.1 Forced Case

The term "*forced*" will refer to a particular case with almost identical numerical settings as for the baseline simulation. The important difference relies on the fact that entropy waves are now imposed at the inlet of the domain. The wave train direction is aligned with the incoming flow and entropy fluctuations are imposed by only forcing the temperature field. The shape of the forcing will be sinusoidal, with a characteristic frequency in time f_1 equal to 1000 [Hz]. The Strhoual number associated to the frequency f_1 for both baseline and forced case[1] is equal to $St_1 = f_1 d/U$ = 0.00733.

The equation relating entropy fluctuations and temperature is given by

$$\frac{s'}{c_p} = \log\left(1 + \frac{T'}{T}\right) - \frac{\gamma - 1}{\gamma}\log\left(1 + \frac{p'}{p}\right), \tag{5.1}$$

where the primed value represents the fluctuating part of the thermodynamic variables and the unprimed quantities are the local mean values. For the present case only temperature waves are imposed at the inlet, hence equation (5.1) assumes the form

$$\frac{s_1'}{c_p} = \log\left(1 + \frac{T_1'}{T_1}\right), \tag{5.2}$$

---

[1] Here the velocity scale U is again the one calculated from the isentropic Mach number $M_{2,\text{is}} = 0.95$.

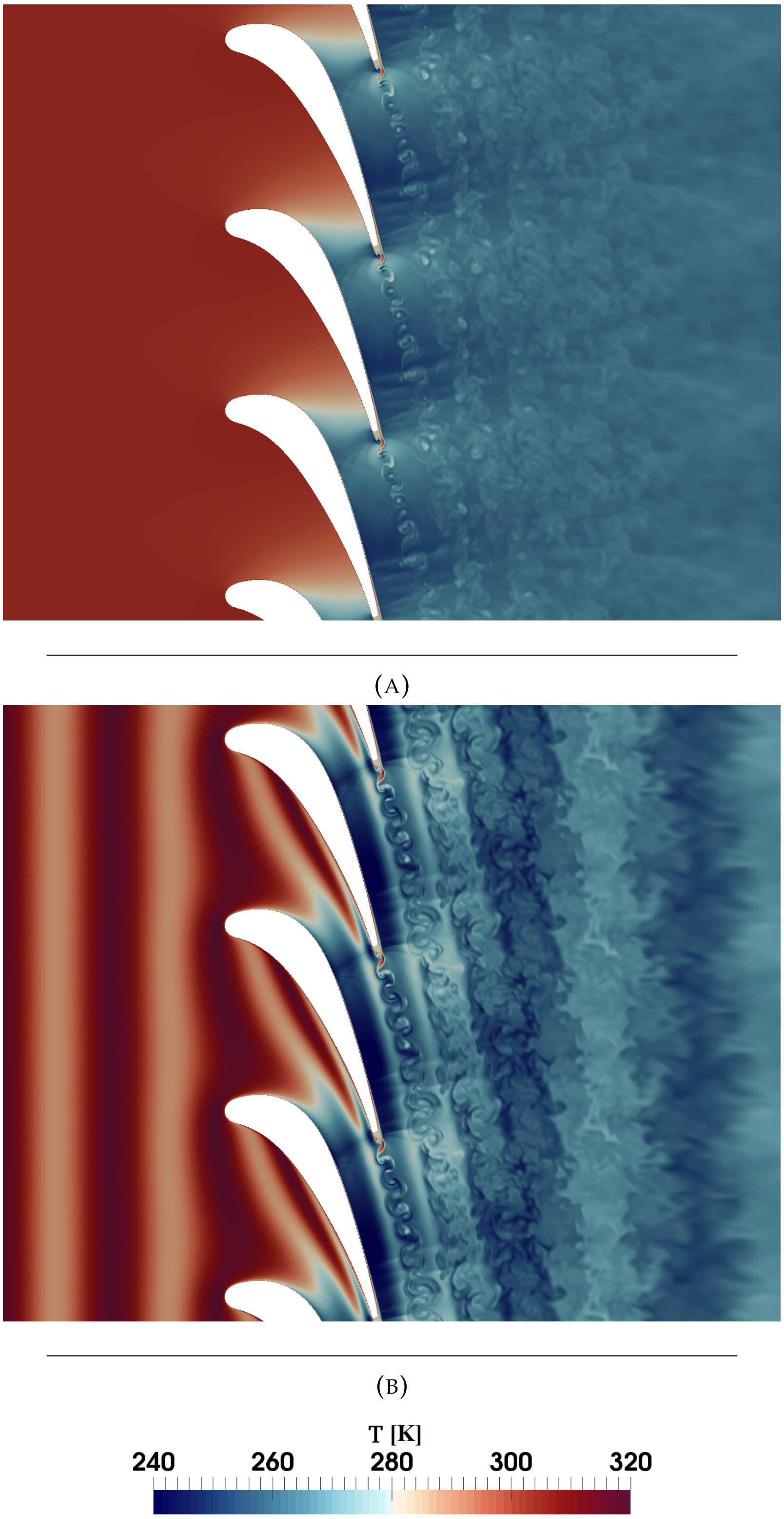

FIGURE 5.1: Instantaneous temperature field along a spanwise section, baseline case (A) and forced case (B).

in which the subscript $_1$ indicates the inlet station. The reference total and static temperatures at the inlet will be the same one of the baseline case, but the static temperature (and the total consequently) will now oscillate according to the expression given by

$$\tilde{T_1}(t) = T_1 + A\,T_1\,\sin(2\pi f_1 t), \tag{5.3}$$

where $\tilde{T_1}$ indicates the inlet static temperature function of time for the forced case, T_1 is the inlet static temperature of the baseline case and A is the amplitude of the disturbance, set to be equal to 4.8%. The choice of the frequency is dictated by the high computational cost of the 3D LES, which otherwise would have been prohibitively long. However, this frequency is still in the limit range of real case scenarios: previous studies in literature indicated that combustion noise has its peak intensity typically in the low frequency range around $200 - 1000$[Hz] [50, 51, 52, 53].

Similar simulations have been conducted by Papadogiannis *et al.* [54], which found that the limiting frequency for the validity of the compact assumption [18] is around 2200[Hz]. Thus, at the selected frequency, the same indirect noise generation mechanism as in classical aero-engines should arise. For the case of incoming planar entropy waves aligned with the flow direction at the inlet, the dispersion relation is simply given by $\lambda_s = U_1/f_1 = M_1 c_1/f_1$, where c_1 is the local speed of sound at the inlet and λ_s indicates the wavelength of the entropy waves. For the forced case, this wavelength corresponds to 76% the axial chord of the blade $C_{ax,\mathrm{mid}}$. The physical time of the simulation was chosen in order to reproduce the passage of ten planar waves through the cascade, corresponding to $t_{\mathrm{sim,forced}} \approx 10/f_1 = 0.01$[s].

Snapshots of the instantaneous temperature field in a spanwise section can be visualized in Figure 5.1 for both the baseline and the forced case.

For the baseline case in Figure 5.1a, it is possible to visualize the flow accelerating up to sonic conditions at the throat. Then the "diamond"-like pattern of waves, shed from the trailing edge vortices, is present just after the throat. Finally, a system of compression and expansion waves is visible at the end of the blade. Figure 5.1b shows instead the features of the flow-field with planar entropy waves injected at the inlet. The planar forcing is revealed at the inlet by the presence of vertical stripes in the temperature field, with the wavelength of the entropy waves λ_s corresponding exactly to the value predicted by the dispersion relation. Once the waves approach the blades they get distorted by the large flow gradients across the vane, becoming aligned with the flow direction at the end of the passage. Then, one axial chord downstream from the blade, it is possible to see almost-planar entropy waves propagating downstream of the passage. The entropy waves hence go back to their original planar organization even if the wavelength of the disturbances is only of the same order of the blade axial chord.

The vortex shedding frequency for the forced case is the same as the one for the baseline case.

Then, a temporal fast Fourier transform (FFT) has been applied on a set of two-dimensional snapshots of velocity, temperature and pressure fields, sampled at a frequency equal to four times the vortex shedding frequency, in order to avoid aliasing. This frequency is widely sufficient to capture possible features of the flow-field appearing at $f_1 = 1000$[Hz].

To evaluate the tones of interest appearing in the frequency content of the signal, an average integral amplitude coefficient, for the pressure fluctuation field p', was defined as

$$A_I(t) = \frac{1}{\gamma p_{01}} \int_{V_{\mathrm{slice}}} p'(t)\,\mathrm{d}\Big(\frac{V}{V_{\mathrm{slice}}}\Big), \tag{5.4}$$

in which V_{slice} is the volume of the sampled domain.

In Figure 5.2, the forced case shows clearly the appearance of a peak at the Strouhal number corresponding to the frequency of 1000[Hz], which was not present in the unforced simulation. Both cases show instead the same peak at the shedding frequency. Several peaks are also present after the tone at f_1, they are related to the shock dynamics at low frequency present in both simulations.

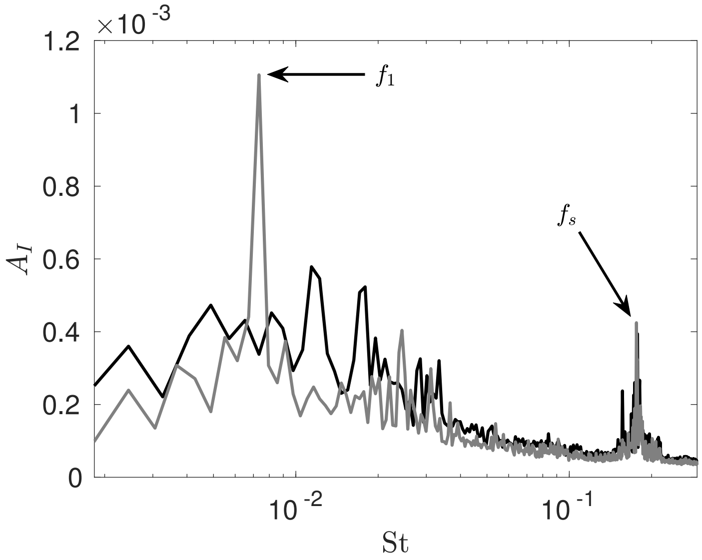

FIGURE 5.2: Average integral amplitude spectrum of the pressure fluctuation field p'; (—) baseline case; (—) forced case.

For both the baseline and the forced case, each field showed a distinct tone in the amplitude of the signal at the shedding frequency $f_s = 24$[KHz], ($St_s = 0.176$). Both cases also showed a frequency content in the range of frequencies among $200 - 7000$[Hz], but with the forced case exhibiting a distinct tone at the inlet forced frequency f_1.

Starting from the pressure fluctuations field p', the amplitude and the phase fields for both cases are shown in Figure 5.3. The amplitude field is expressed in decibels [dB], taking as reference pressure the value $p_{\text{ref}} = 20[\mu\text{Pa}]$.

For the unforced simulation (Figure 5.3a), it is possible to observe the presence of a low frequency dynamics at 1000[Hz] of the system of compression and expansion waves. The amplitude of the pressure fluctuations is instead negligible upstream of the NGV passage, up to the throat section.

As entropy waves are imposed at the inlet, instead, one can immediately notice several zones of interest in the amplitude field, which were not present in the baseline case.

First, there is a glowing white area towards the end of the blade (suction side), where the system of shocks is located; its amplitude is greater then 160[dB]. This suggest that the inlet forcing frequency can excite the dynamics of the flow in this region. Then, the convergent section of the vane passage exhibits amplitudes around 150[dB] up to the throat section. A possible explanation can be that entropy waves interacting with strong mean flow gradients give rise to an entropy-acoustic modal interaction. Considering for instance a weakly non linear Kovasznay decomposition [37, 55] of all compressible flow variables, acoustic production due to acoustic-entropy coupling can arise due to scattering: i.e. the acoustic waves are scattered by the convected entropy spots passing through the nozzle. According to Kovasznay decomposition [37, 55] the acoustic production scattering term is $\partial_t(\nabla \cdot s_e \mathbf{u_p})$,

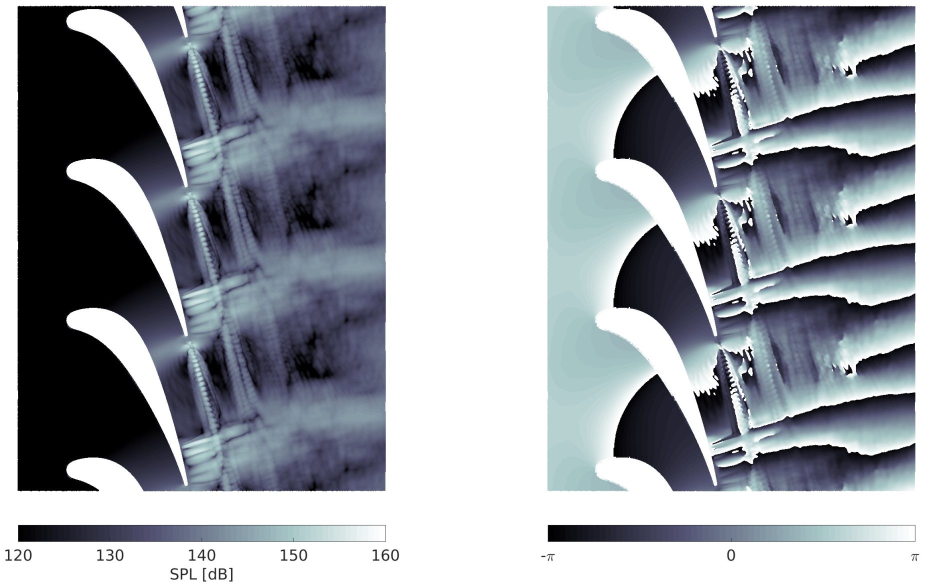

(A) Amplitude (left) and phase (right) fields of p' at the forcing frequency f_1, baseline case.

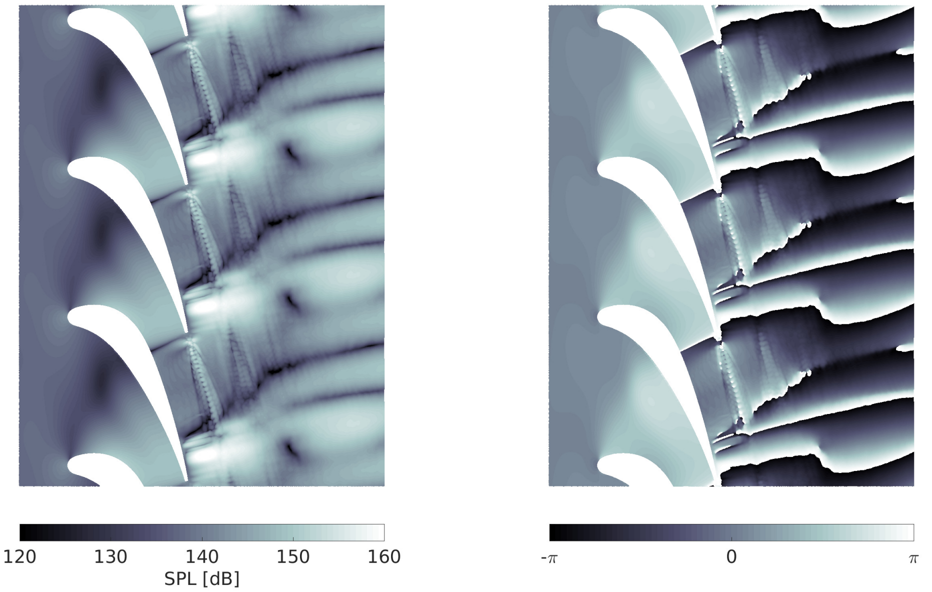

(B) Amplitude (left) and phase (right) fields of p' at the forcing frequency f_1, forced case.

FIGURE 5.3: FFT of the pressure fluctuation field at the forcing frequency f_1, baseline case (A) and forced case (B).

where s_e is entropy perturbation of the entropy mode and $\mathbf{u_p}$ is the velocity perturbation of the acoustic mode. Finally, the upstream region of the cascade also exhibits regions of noticeable amplitude which where absent in the baseline case, suggesting the presence of reflected acoustic waves propagating upstream. A dark line in the neighborhood of the sonic throat identifies also a region of lower amplitude,

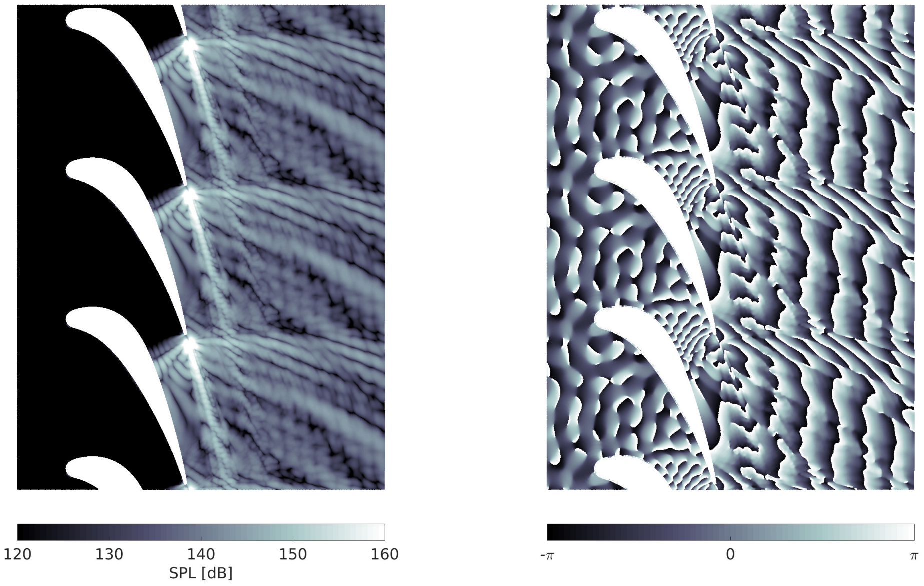

(A) Amplitude (left) and phase (right) fields of p' at the shedding frequency f_s, baseline case.

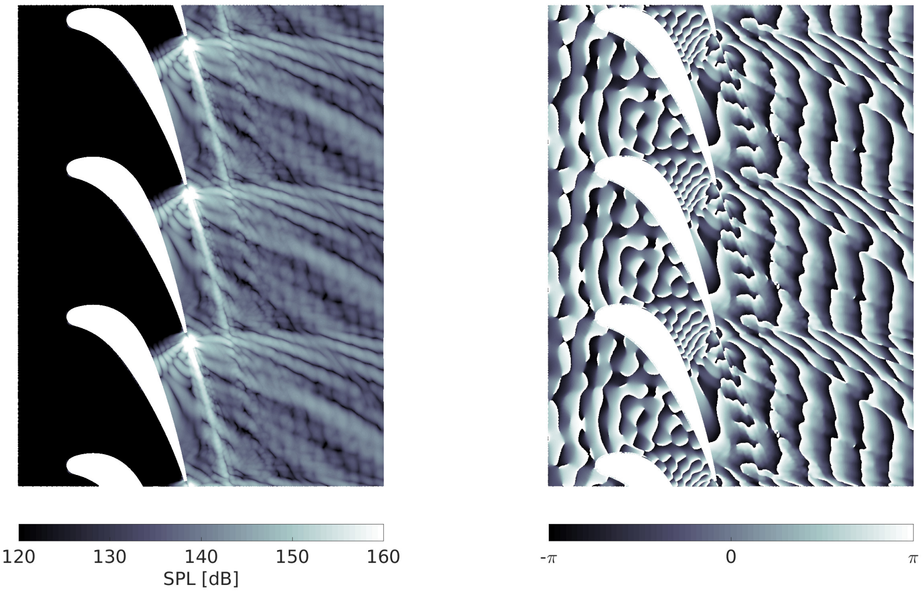

(B) Amplitude (left) and phase (right) fields of p' at the shedding frequency f_s, forced case.

FIGURE 5.4: FFT of the pressure fluctuation field at the shedding frequency f_s, baseline case (A) and forced case (B).

showing the decoupling between the convergent part of the vane and the discharge section.

At the shedding frequency f_s, both cases show practically identical features as it can be seen from Figure 5.4.

Regarding the fluctuation field of the velocity magnitude U'_{mag}, the same FFT at the

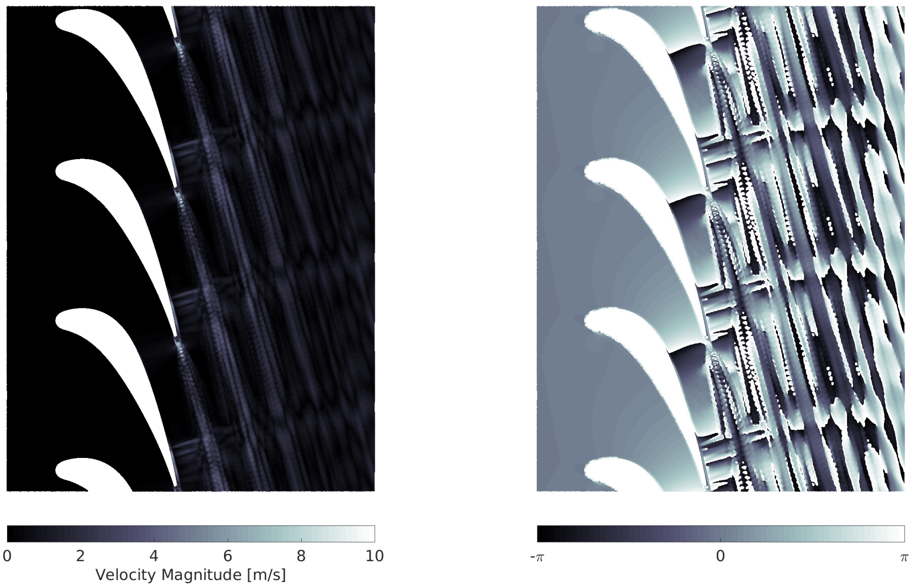

(A) Amplitude (left) and phase (right) fields of U'_{mag} at the forcing frequency f_1, baseline case.

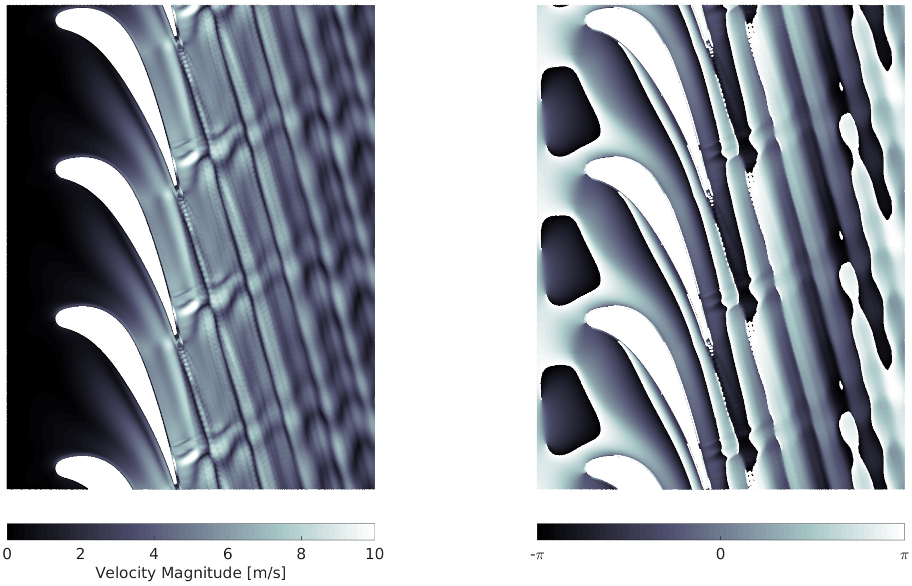

(B) Amplitude (left) and phase (right) fields of U'_{mag} at the forcing frequency f_1, forced case.

FIGURE 5.5: FFT of the velocity magnitude fluctuation field at the forcing frequency f_1, baseline case (A) and forced case (B).

inlet forcing frequency f_1 shows several difference between the two simulated cases. The unforced case of Figure 5.5a highlights again the presence of a latent dynamics of the system of shocks. The forced case of figure 5.5b, on the other end, presents higher amplitudes in this region. On the same figure, from the phase field, it is also

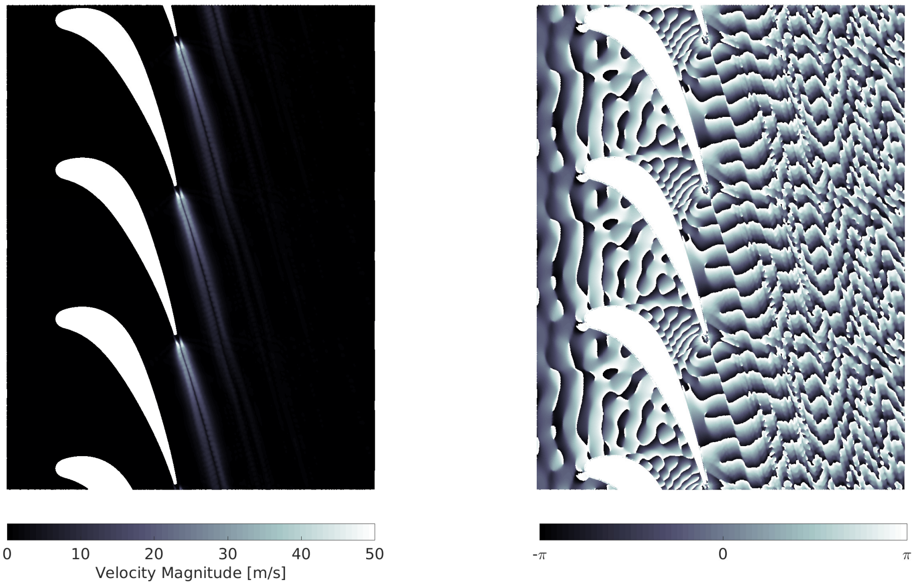

(A) Amplitude (left) and phase (right) fields of U'_{mag} at the shedding frequency f_s, baseline case.

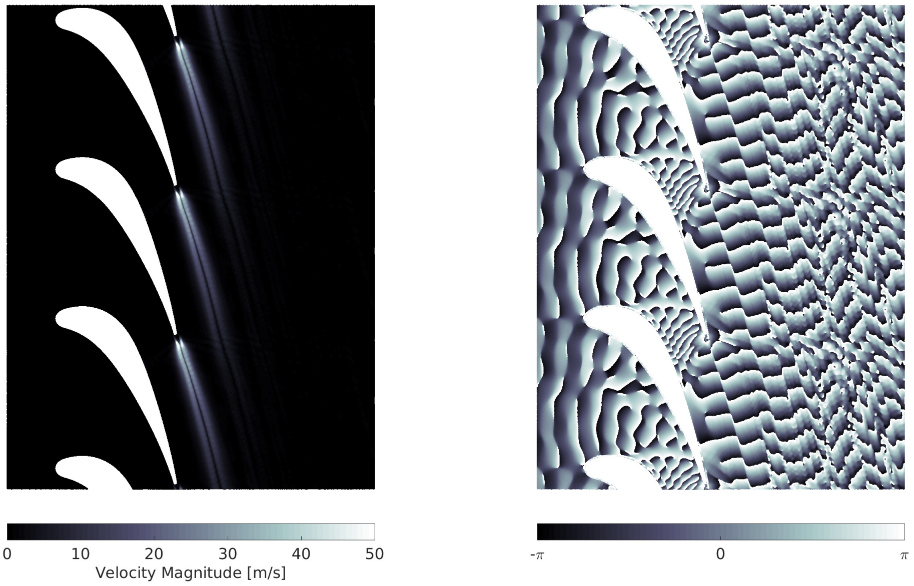

(B) Amplitude (left) and phase (right) fields of U'_{mag} at the shedding frequency f_s, forced case.

FIGURE 5.6: FFT of the velocity magnitude fluctuation field at the shedding frequency f_s, baseline case (A) and forced case (B).

possible to observe the "shape" of these fluctuations, which are in close resemblance to the temperature waves of Figure 5.1b.

Once more, the amplitude and the phase field of the FFT at the shedding frequency

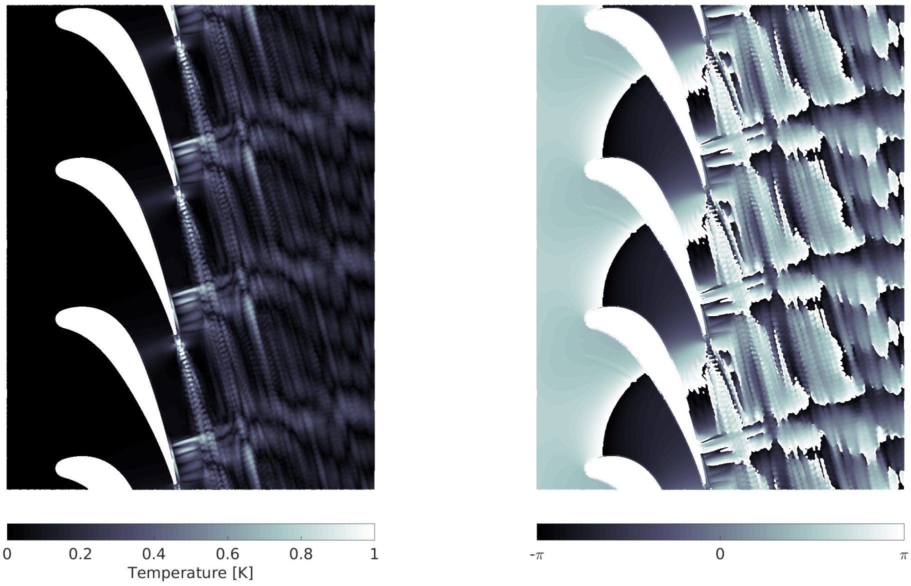

(A) Amplitude (left) and phase (right) fields of T' at the forcing frequency f_1, baseline case.

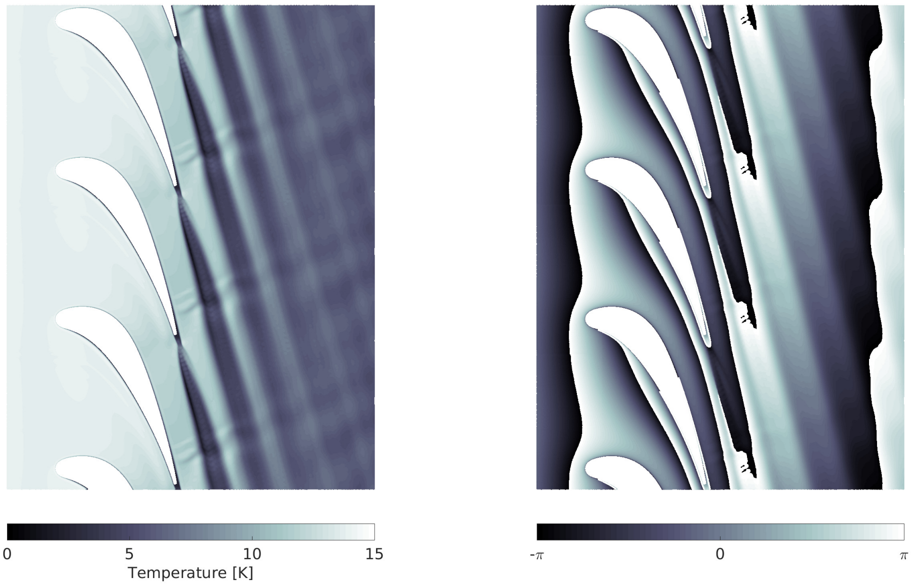

(B) Amplitude (left) and phase (right) fields of T' at the forcing frequency f_1, forced case.

FIGURE 5.7: FFT of the temperature fluctuation field at the forcing frequency f_1, baseline case (A) and forced case (B).

do not exhibit any detectable difference from each other and it possible to recognize the shear layers detaching from the blade.
The last analysis is then focused on the FFT of the temperature fluctuation field T'. Again, important difference are present at the inlet forcing frequency f_1, while similar features are present at the shedding frequency f_s.

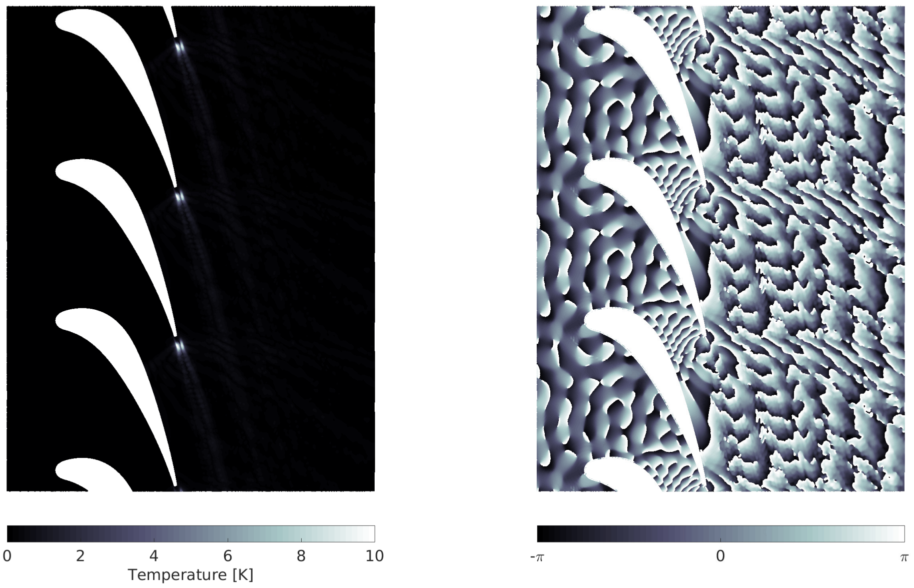

(A) Amplitude (left) and phase (right) fields of T' at the shedding frequency f_s, baseline case.

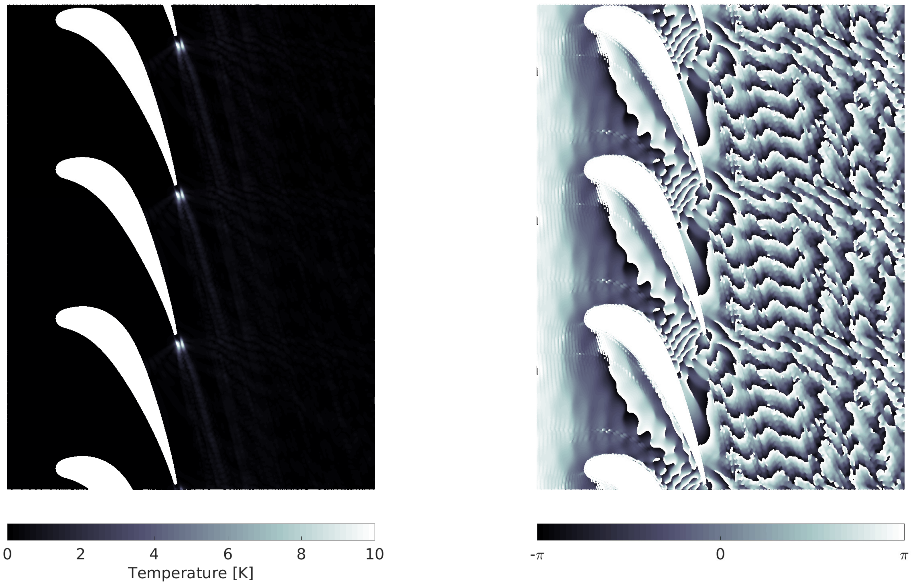

(B) Amplitude (left) and phase (right) fields of T' at the shedding frequency f_s, forced case.

FIGURE 5.8: FFT of the temperature fluctuation field at the shedding frequency f_s, baseline case (A) and forced case (B).

At f_1 the same low frequency dynamics as for pressure and velocity is visible in the amplitude field of Figure 5.7a (baseline case).
The amplitude field of the forced simulation (Figure 5.7b) shows that entropy waves reduce their intensity after passing the blade row. The interaction with the system of

shocks is also visible. On the other hand, the phase field at the same frequency shows the planar character of the incoming entropy waves; afterwards they get strongly distorted through the NGV passage and analogous "*jet/streaks*"-like structures as in the velocity phase field at f_1 are visible in the middle of the passage. The waves become almost planar again after approximately one axial chord $C_{ax,\mathrm{mid}}$ downstream of the blade row.

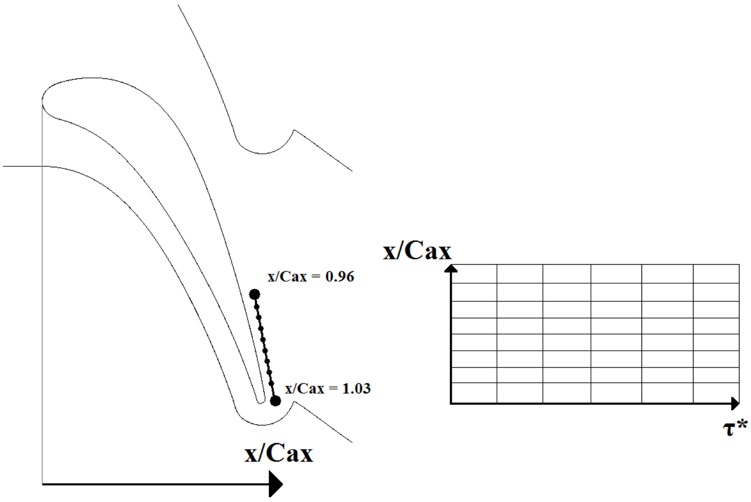

FIGURE 5.9: Schematic procedure for the analysis of shock dynamics.

In conclusion, the presence of acoustic production at the forcing frequency f_1, with noticeable amplitudes, is observed both upstream and downstream of the blade passage. The downstream generated noise might be emitted from the system of weak shocks on the suction side, while the upstream noise might be generated in the subsonic convergent region of the passage and then reflected backwards. Notably, all the fluctuating fields show significant differences in both phase and amplitude fields of the FFT at the forcing frequency f_1. No perturbation of the shedding dynamics is induced by the inlet forcing, maybe due to the very different frequencies involved in the respective phenomena.

From the previous analysis of the flow variables' frequency content, entropy waves seem to strongly interact with the system of weak normal shocks; therefore, a sampling line has been traced in that particular zone, where the pressure fluctuation amplitudes were the highest. For this line, the divergence of the velocity field has been sampled for a number of 100 points throughout the time evolution of the simulation. The sampling frequency is the same as the one used for the two-dimensional snapshots. Then, the sampled field is projected on a space-time grid where the spatial coordinate is represented by the non-dimensional distance $x/C_{ax,\mathrm{mid}}$ and the temporal coordinate by a non dimensional time $\tau^* = tU/d$. A graphic description of the procedure can be found in Figure 5.9. With this method, the characteristic dynamics of the system of normal shocks can be identified and the present analysis will be conducted for both the baseline and the forced case. The divergence of the velocity field is expressed in terms of its non dimensional counterpart defined as $\nabla \cdot \tilde{\mathbf{u}} = \nabla \cdot (\mathbf{u}\, d/U)$.

Figure 5.10 shows the non dimensional field $\nabla \cdot \tilde{\mathbf{u}}$ projected on the space-time diagram for both the baseline and the forced case. Only negative values are shown since they identify compression zones and hence the formation of shockwaves. Three regions of interest can be identified in the graph.

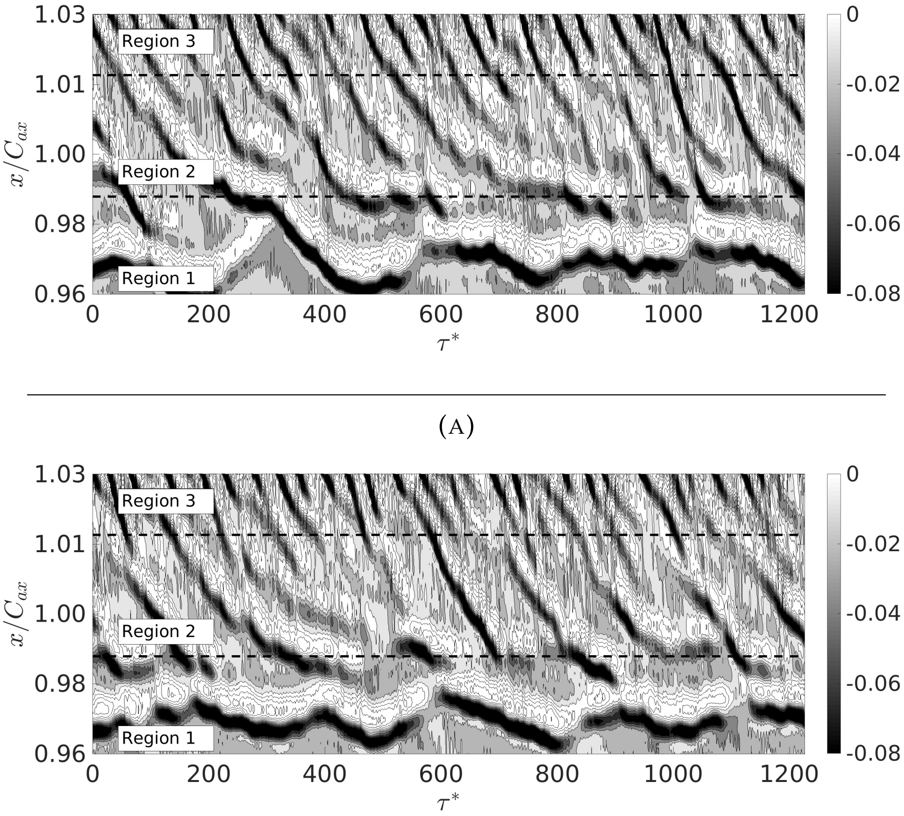

(A)

(B)

FIGURE 5.10: Isocontours of $\nabla \cdot \tilde{\mathbf{u}}$ in the space-time diagram; baseline case (A); forced case (B).

Region 1 corresponds to the zone where the position of the shock changes slowly during time; this region has fairly similar characteristics for both the baseline and the forced case. The frequency content in *Region* 1 is in the range of $200-900$[Hz]. *Region* 2, instead, corresponds to the glowing zone for which the amplitude of the pressure fluctuations is the highest in Figure 5.3b. For the forced case in Figure 5.10b, black stripes at regular intervals of time are visible in *Region* 2. The frequency of these intervals is evaluated by the means of a FFT at a fixed position in space: it corresponds exactly to the inlet forcing frequency $f_1 = 1000$[Hz]. Remarkably, this characteristic does not appear for the baseline case in Figure 5.10a and the shock movement is not organized at any particular frequency of interest; its frequency content is instead in the range of $500 - 3000$[Hz]. Finally, *Region* 3 corresponds to the initial part of the wake, where compression and expansion waves are emitted by vortical structures and appear with higher frequencies. The structure of *Region* 3 is similar for both cases and its dynamics is in the range of $3000 - 7000$[Hz].
These aspects of the shock dynamics in *Region* 2 justify the high amplitude found by the FFT at 1000[Hz]. A detailed image of *Region* 2 is pictured in Figure 5.11 for both simulations. A shock movement mechanism, with shocks appearing and then vanishing, was also documented in literature by the work of Panda [56] and the work of Risborg & Soria [57]. They underlined shock oscillations cycles in two different jet flows and this peculiar feature is referred as *splitting mechanism*.

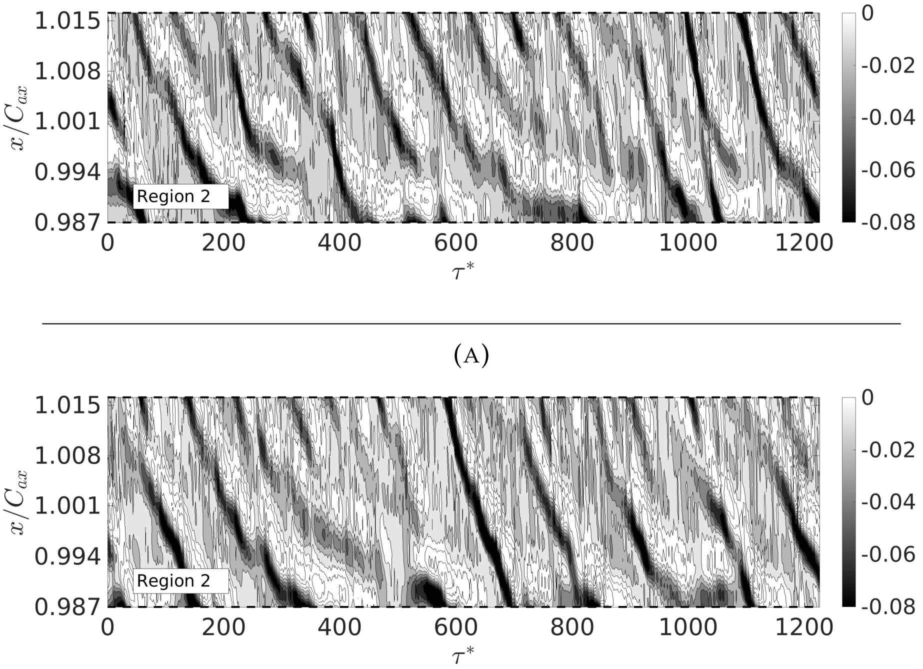

(A)

(B)

FIGURE 5.11: Isocontours of $\nabla \cdot \tilde{\mathbf{u}}$ in the space-time diagram, detail of *Region* 2; baseline case (A); forced case (B).

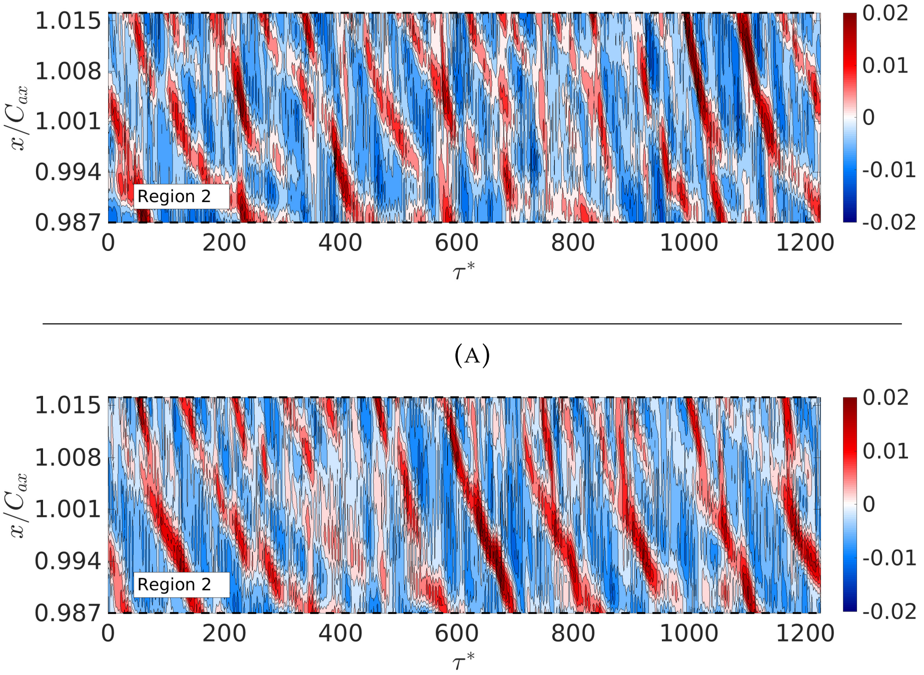

(A)

(B)

FIGURE 5.12: Isocontours of $p'/(\gamma\, p_{01})$ in the space-time diagram, detail of *Region* 2; baseline case (A); forced case (B).

The same dynamics can be visualized for the pressure fluctuation field p', as the detail of *Region* 2 in Figure 5.12 exhibits clearly; here the field p' has been made non dimensional by the expression $p'/(\gamma\, p_{01})$.
In the end, a similar analysis for the evaluation of the convection velocity of the vortical structures, emitted from the trailing edge, has been performed. The results were identical to the one of the baseline case presented in subsection 4.3.3.

5.1.2 Proper Orthogonal Decomposition

The flow-fields analyzed in the present work exhibit complex features with a wide range of temporal and spatial frequencies. Nowadays, it has become common practice in fluid-flow analysis to seek for physically relevant features (*modes*) for the description of these temporal and spatial characteristics.
In the previous section, only the FFT at two specific frequencies (f_1 and f_s) has been conducted, still providing a lot of information of the flow-fields and a large number of results to analyze.
In the present subsection, the modal analysis under the name of *Proper Orthogonal Decomposition* will be used in order to extract the most relevant modes appearing in the 2D snapshots sampled during the simulations. The study will be performed for both the unforced and the forced flow-fields.
The term modal decomposition refers to a mathematical technique with the aim of educing dynamically and energetically relevant features of the flow. In POD, the spatial modes are often referred as *topos*, while the temporal ones as *chronos*.
In the theory of stochastic processes, The Karhunen-Loève (KL) theorem defines an optimal representation of a stochastic process as an infinite linear combination of orthogonal functions. In 1967 Lumley [58] applied this technique to extract coherent structures from turbulent signals.
The POD is based on the optimization of the mean square error of the flow-field being examined. It is the discretized, finite form of the KL transform [59, 60] and provides an algorithm to decompose the dataset into a minimal number of basis functions, which capture the largest amount of energy (L^2 norm).
With the POD, one seeks to separate the field of interest in the form[2]

$$u(\mathbf{x},t) = \sum_j a_j(t)\phi_j(\mathbf{x}). \tag{5.5}$$

The classical POD method directly determines the set of spatial modes that can optimally represent the selected field, while it recovers the temporal coefficients a_j afterwards.
First, the fluctuating part of the field u is extracted at each time-step as

$$u'(\mathbf{x},t) = u(\mathbf{x},t) - \overline{u(\mathbf{x})} \in \mathbb{R}^n, \tag{5.6}$$

where the overline indicates the time averaged field. Then, the spatial collection u' at each sampled time is collected into a stacked matrix of the form

$$\mathbf{X} = [u'(\mathbf{x},t_1), u'(\mathbf{x},t_2), \ldots, u'(\mathbf{x},t_m)] \in \mathbb{R}^{n\times m}. \tag{5.7}$$

The goal of the POD is to determine the optimal basis vectors, with the least number of modes ϕ_j, that best represent the given data in $\mathbf{X}$. The solution leads to an

---

[2] It is important to notice that the form in equation (5.5) explicitly employs a separation of variables.

eigenvalue problem of the form [61]

$$\mathbf{R}\phi_j = \lambda_j \phi_j,\ \ \lambda_1 \geq \lambda_2 \geq \ldots \geq \lambda_n, \tag{5.8}$$

in which $\mathbf{R}$ is the covariance matrix of $\mathbf{X}$, defined as

$$\mathbf{R} = \frac{1}{m}\sum_{i=1}^{m} u'(\mathbf{x}, t_i) u'(\mathbf{x}, t_i)^T = \frac{1}{m}\mathbf{X}\mathbf{X}^T \ \in \mathbb{R}^{n\times n}. \tag{5.9}$$

The size n is equal to the number of spatial degrees of freedom of the sampled data. The eigenvectors found from problem (5.8) are the topo-modes. These modes are orthonormal, that is their inner product is equal to

$$\langle \phi_i, \phi_j \rangle = \int_V \phi_i, \phi_j \mathrm{d}V = \delta_{ij}. \tag{5.10}$$

Instead, the eigenvalues λ_j express how much "energy", of the original data, each eigenvector ϕ_j contains (in the L^2 sense). The total amount of energy represented by r modes can be calculated as

$$E^r_{L^2} = \sum_{j=1}^{r}\lambda_j / \sum_{j=1}^{n}\lambda_j. \tag{5.11}$$

The truncated series of the vector u' is hence

$$u'(\mathbf{x}, t) \approx \sum_{j=1}^{r} a_j(t)\phi_j(\mathbf{x}). \tag{5.12}$$

Finally, the temporal coefficients are determined by

$$a_j(t) = \langle u'(\mathbf{x}, t), \phi_j(\mathbf{x})\rangle. \tag{5.13}$$

It is important to notice that the aforementioned algorithm is strictly valid for a fluid flow placed on a uniform grid. This is very rarely the case for fluid flows around complex geometries, therefore the cell volume for for each data point needs to be included in the formulation to represent correctly the inner product (volume integral). Then, the covariance matrix needs to be modified accordingly to $\mathbf{R}^* = \mathbf{R}\mathbf{W} = (1/m)\mathbf{X}\mathbf{X}^T\mathbf{W}$, where $\mathbf{W}$ represents the spatial weights.

In numerical simulations, usually the number of spatial degrees of freedom n is very large compared to the number of snapshots m available. The resulting weighted covariance matrix $\mathbf{R}^* \in \mathbf{R}^{n\times n}$ also becomes ridiculously large, and the use of the classical method might be practically impossible to handle numerically.

In 1987, Sirovich [62] showed that the temporal correlation matrix gives rise to the same topo-modes, while reducing drastically the size of the arising eigenvalue problem, making it computationally more tractable. This approach is known as *method of snapshots*, and it reduces to solving the following eigenvalue problem[3]

$$\mathbf{X}^T\mathbf{W}\mathbf{X}\psi_j = \lambda_j\psi_j,\ \ \psi_j \in \mathbb{R}^m,\ m \ll n, \tag{5.14}$$

in which ψ_j is the j-th chrono-mode.

The size of the matrix $\mathbf{X}^T\mathbf{W}\mathbf{X}$ is now $m \times m$ instead of the much greater original size

---

[3] In the case of non-uniform grids.

$n \times n$. Moreover, the same non zero eigenvalues are shared between $\mathbf{X}^T\mathbf{W}\mathbf{X}$ and $\mathbf{X}\mathbf{X}^T\mathbf{W}$ and their eigenvectors are linked via the relationships that exists between the eigenvalue and singular value decompositions.
The topo-modes, in fact, can be recovered through

$$\phi_j = \mathbf{X}\psi_j \frac{1}{\sqrt{\lambda_j}}, \ \psi_j \in \mathbb{R}^n. \tag{5.15}$$

The totality of the topo-modes can be written in a matrix form as

$$\mathbf{\Phi} = \mathbf{X}\mathbf{\Psi}\mathbf{\Lambda}^{-1/2}. \tag{5.16}$$

Due to the significant reduction of the problem size, also computational and memory resources required reduces drastically. Therefore, the method of snapshots is the most-widely used for the POD.
In the present work the POD has been applied to the temperature, pressure and velocity magnitude field. The weighting matrix $\mathbf{W}$ was made non-dimensional by dividing the volume of each cell by the volume of the 2D domain extruded by Δz (i.e. one layer). The structure of the matrix is diagonal and each element is given by $\text{diag}(W_i) = V_i/V_{\text{slice}}$. Since only the diagonal has non-zero elements, the matrix has been stored in Matlab® via the command *spdiag*, which reduces significantly the memory allocation required. The discrete, generalized L^2 weighted product is defined as

$$\langle \mathbf{u}, \mathbf{v} \rangle_{\mathbf{W}} = \mathbf{u}^T\mathbf{W}\mathbf{v}, \tag{5.17}$$

and it is useful to remind that now the topo-modes are $\mathbf{W}$-orthogonal, i.e. with the inner product $\langle \phi_i, \phi_j \rangle_{\mathbf{W}} = \delta_{ij}$.
Furthermore, given the fact that the weighting matrix is non-dimensional, all the energy contained in the eigenvalues λ_j has the units of the matrix $\mathbf{X}$ squared[4]. Then, the resulting topo-modes from (5.16) are also non dimensional. A schematic description of the algorithm implemented in Matlab® is given in Table 5.1.

TABLE 5.1: POD algorithm

Algorithm	
Input:	Snapshots sequence $\mathbf{X}$ Weighting matrix $\mathbf{W}$
1. $[\mathbf{\Psi}, \mathbf{\Lambda}] = \text{eig}(\mathbf{X}^T\mathbf{W}\mathbf{X})$; 2. $\mathbf{\Phi} = \mathbf{X}\mathbf{\Psi}\mathbf{\Lambda}^{-1/2}$;	
Output:	Eigenvalues $\mathbf{\Lambda}$ Topo-modes $\mathbf{\Phi}$ Chrono-modes $\mathbf{\Psi}$

---

[4] The eigenvectors ψ_j forms an orthonormal basis and therefore $||\psi_j|| = 1$.

5.1.3 POD, Temperature Field

Starting with the temperature field, it is immediately possible to recognize the different features characterizing the baseline and the forced cases.

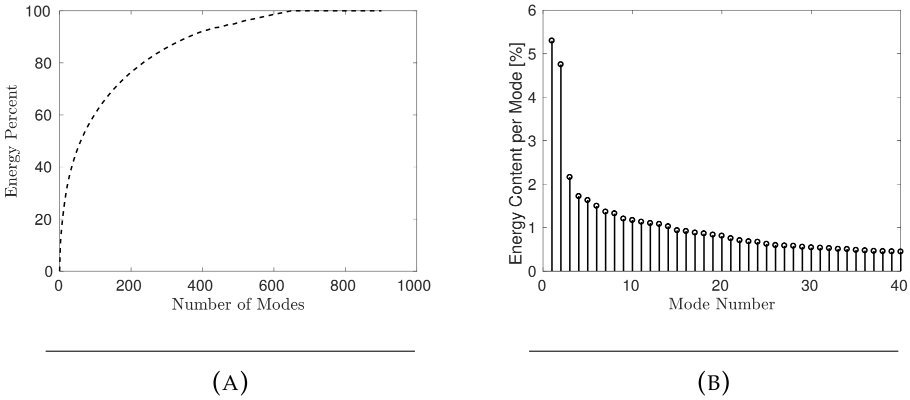

FIGURE 5.13: Energy percent retaining the first r modes (A), and energy associated to each mode (B). Temperature fluctuation field T'; baseline case.

The energy distribution among the temperature fluctuation modes, is shown in Figure 5.13 for the baseline case. One can see that the first 8 modes roughly capture 20% of the energy, with mode 1 and 2 containing the highest energy content per mode $\approx 5\%$. In order to capture 90% of the energy, 400 modes are needed, while the 99% of the energy is captured with 650 modes. An analysis of the chrono- and topo-modes showed that the first two POD modes have a similar periodicity (frequency content) and a similar structure in space, as it can be seen from Figure 5.14. The chrono-modes frequency content is expressed in terms of the Strouhal number with the usual definition $St = fd/U$. The dominant frequency is $St = 0.176$ as shown in the chrono-modes of Figure 5.14. From a physical point of view, these structures represent the vortex shedding phenomenon. The appearance of modes as a couple is an evidence that the modes represent a wave-like periodic structure of the flow: the POD modes are represented by real functions, and two modes are needed to describe a traveling wave, representing the real and complex parts respectively.

The following couple of modes $3 - 4$ is instead associated with the system of compression and expansion waves arising from the trailing edge. One could notice, in fact, the dark and light areas around the trailing edge in Figure 5.15. This region corresponds to *Region* 3 highlighted in Figure 5.10. The frequency content is around $St = 0.016$ corresponding to a frequency $f = 2180$[Hz]. Only the third mode will be showed in Figure 5.15 for the sake of clarity and conciseness.

The couple $5 - 6$ is also associated to the shock movement mechanism but with a lower frequency content at $St = 0.004$ corresponding to $f = 545$[Hz], Figure 5.16. In this case the darkest and lightest zones of the modes are related to the movement in *Region* 1, also highlighted in 5.10.

Then, the couple $7 - 8$ exhibits again some dominant dynamics of the shock movement at $St = 0.012 \rightarrow f = 1636$[Hz], Figure 5.17.

Finally, the last couple $9 - 10$ will be showed, once again exhibiting the dynamics of the shock motion at the dominant frequency $St = 0.028 \rightarrow f = 3818$[Hz] and at $St = 0.0081 \rightarrow f = 1100$[Hz], Figure 5.18.

From the previous results, one can clearly distinguish the modeshapes associated

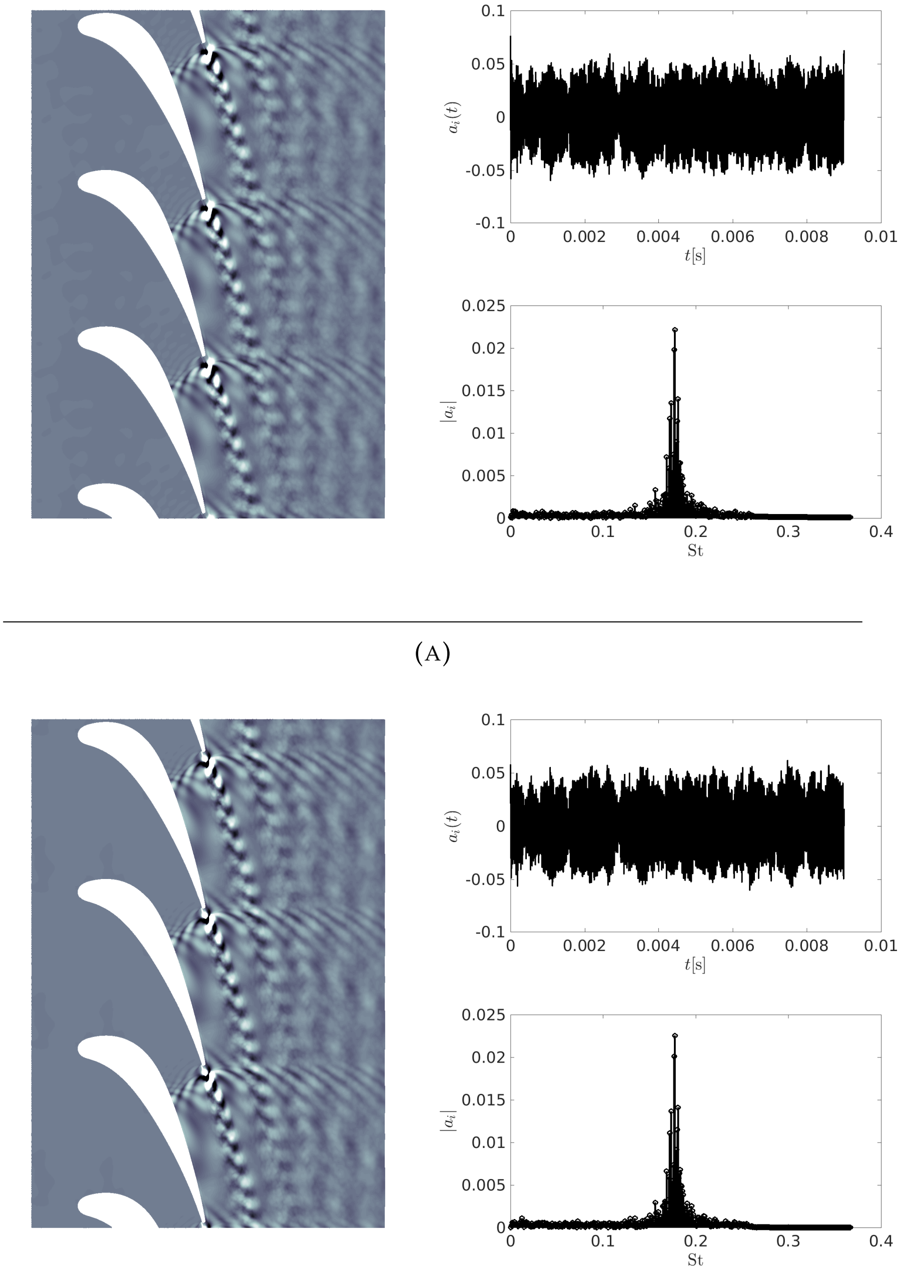

(A)

(B)

FIGURE 5.14: First (A) and second (B) POD modes of the temperature fluctuation field T'; baseline case.

with the shedding phenomenon and the shock movement. Moreover, their frequency content is well separated since there are no topo-modes which are associated to chrono-modes with both frequencies.

The frequency content of the modes representing the waves traveling at the end of the blade are not always associated to a single frequency, and even if dominant tones are distinguishable, several other frequencies appear in the temporal signal. In addition, the POD also shows that the frequency content of the shock movement is also in the frequency range ≤ 10 [kHz].

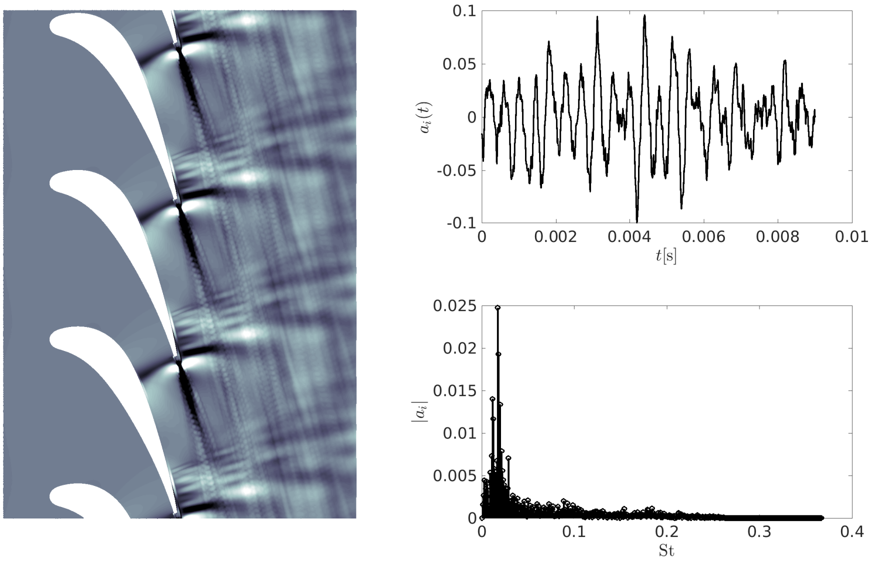

FIGURE 5.15: Third POD mode of the temperature fluctuation field T'; baseline case.

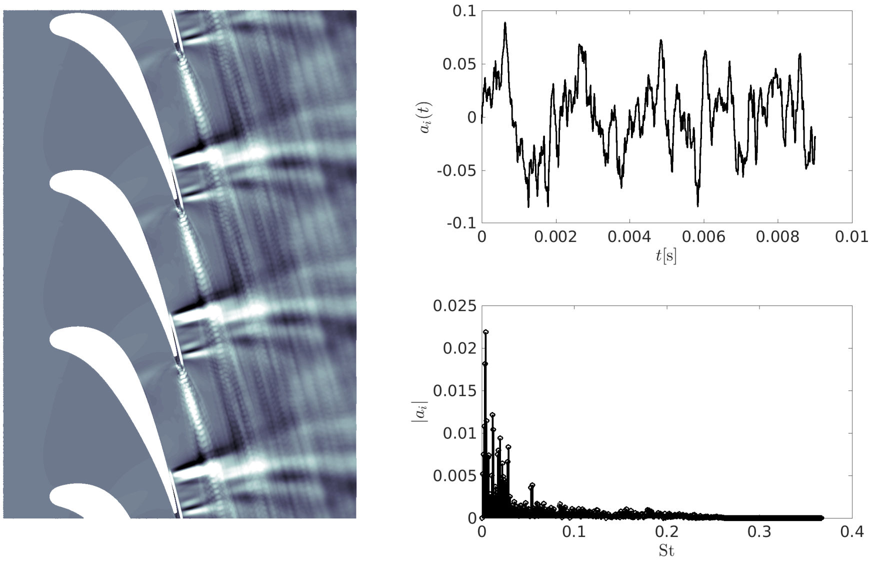

FIGURE 5.16: Fifth POD mode of the temperature fluctuation field T'; baseline case.

Moving the attention to the forced case, the situation changes significantly: now, almost the totality of the energy is associated to the first two modes, which contain more than 90% of the energy by themselves. The energy retained as function of the number of modes and the energy per mode are pictured in Figure 5.19 for the forced case. The topo-mode associated to the couple $1-2$ and its respective chrono-mode is shown in Figure 5.20.

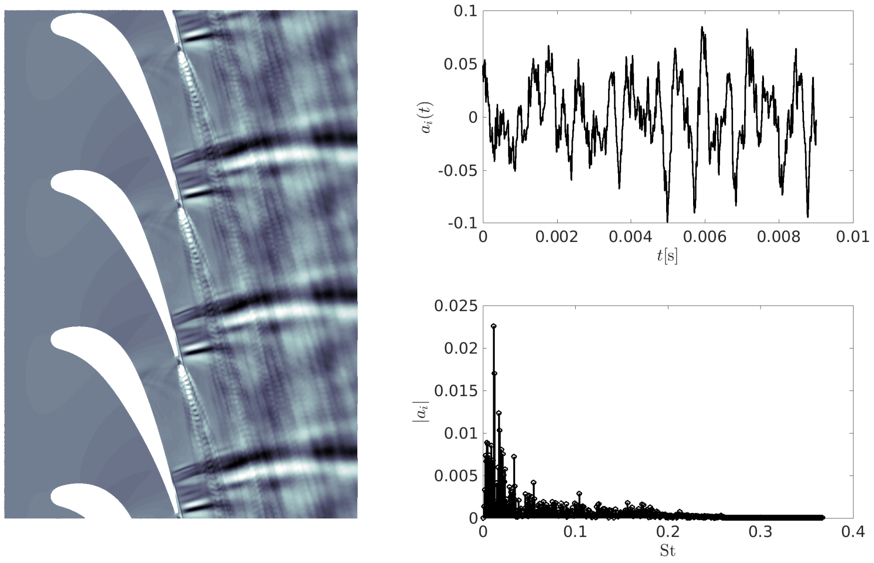

FIGURE 5.17: Seventh POD mode of the temperature fluctuation field T'; baseline case.

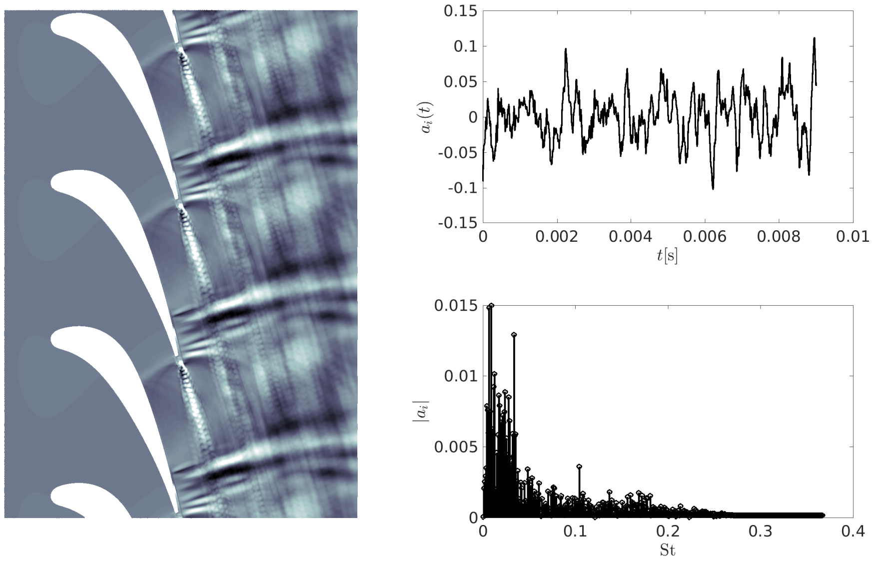

FIGURE 5.18: Ninth POD mode of the temperature fluctuation field T'; baseline case.

The time signal shows a perfectly periodic trend of the temporal coefficient associated to the single frequency of $f_1 = 1000$[Hz]. The spectrum of the temporal coefficient, in fact, shows the dominant tone at $St_1 = 0.00733$. The spatial modeshape also shows the incoming planar wave train of entropy waves which get strongly distorted as they approach the vane passage. The aforementioned topo-mode has strong resemblances with the instantaneous temperature field of Figure 5.1b, only missing the mixing feature caused by the vortex shedding.

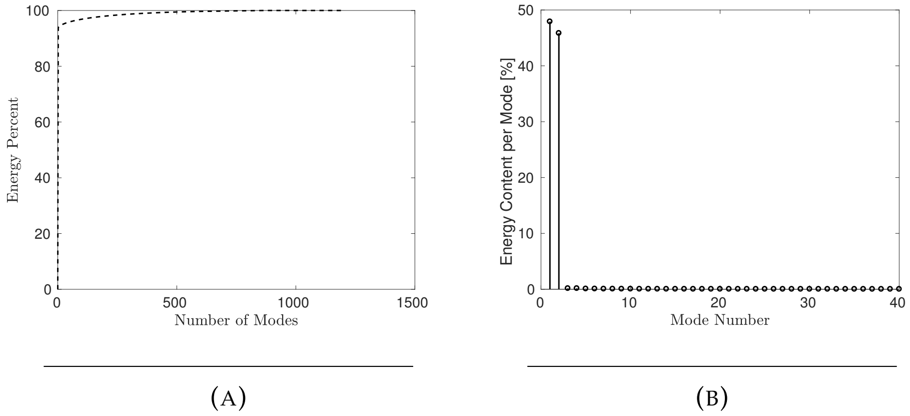

(A) (B)

FIGURE 5.19: Energy percent retaining the first r modes (A), and energy associated to each mode (B). Temperature fluctuation field T'; forced case.

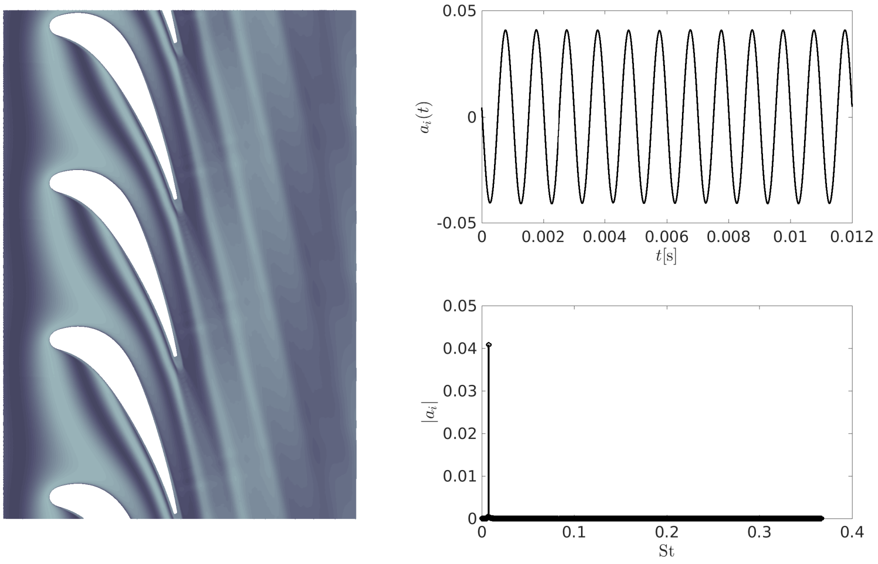

FIGURE 5.20: First POD mode of the temperature fluctuation field T'; forced case.

The other modes calculated with the POD algorithm are associated to the vortex shedding phenomenon and to the shock movement mechanism. Their modeshapes are similar to the ones showed for the baseline case and will not be repeated.

5.1.4 POD, Pressure Field

The analysis is focused now on the pressure fluctuation field p', for which the POD algorithm is applied and the same analysis as for the temperature fluctuation field is performed.
The POD modes for the baseline case are very similar to the ones individuated for the field T'. The energy associated to the modes is plotted in Figure 5.21.
The first couple, associated to the shedding mode, contains 17% of the total energy,

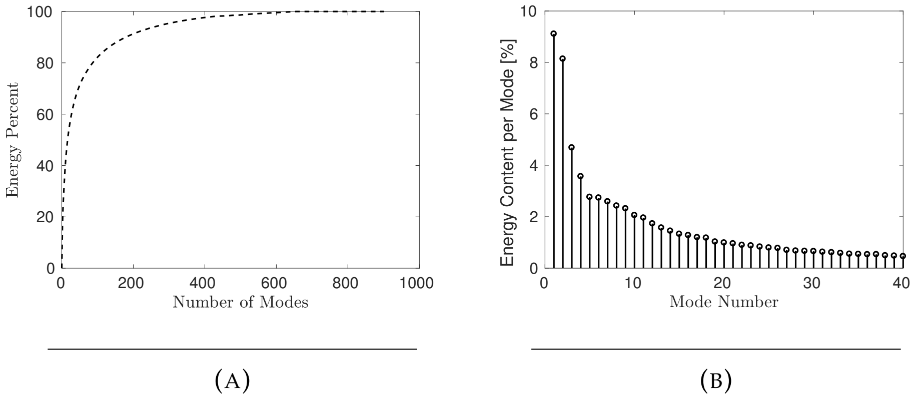

(A)

(B)

FIGURE 5.21: Energy percent retaining the first r modes (A), and energy associated to each mode (B). Pressure fluctuation field p'; baseline case.

while the energy content per mode drops below 5% for the successive ones. To represent 90% of the total energy, approximately 300 modes are needed.
The modeshape associated to the vortex shedding is pictured is Figure 5.22; once again the dominant tone is at $St = 0.176$.

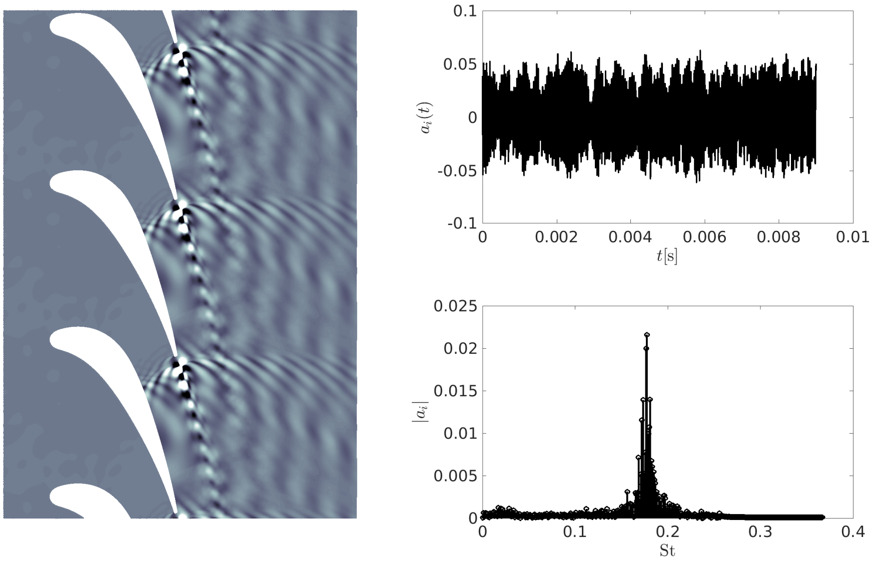

FIGURE 5.22: First POD mode of the pressure fluctuation field p'; baseline case.

The couple $3 - 4$, as for the temperature, is associated with the system of compression and expansion waves arising from the trailing edge, as depicted in Figure 5.23.
The couple $5 - 6$ is, again, associated to the shock movement at an axial position along the blade of $x/C_{ax,\mathrm{mid}} = 0.95$, with a frequency content at $St = 0.004$, Figure 5.24.
Other couples are also associated to the low frequency dynamics of the compression and expansion waves originating from the trailing edge and are analogous to the temperature topo-modes.

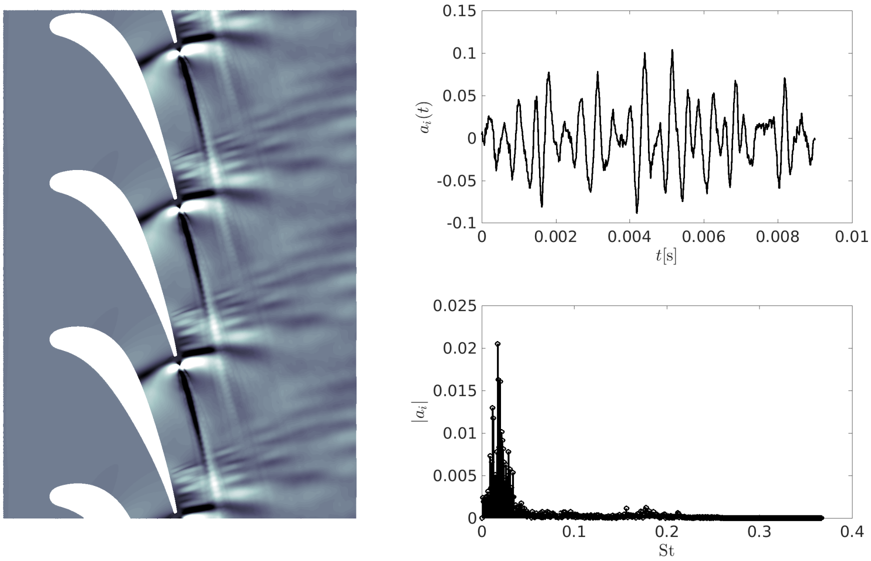

FIGURE 5.23: Third POD mode of the pressure fluctuation field p'; baseline case.

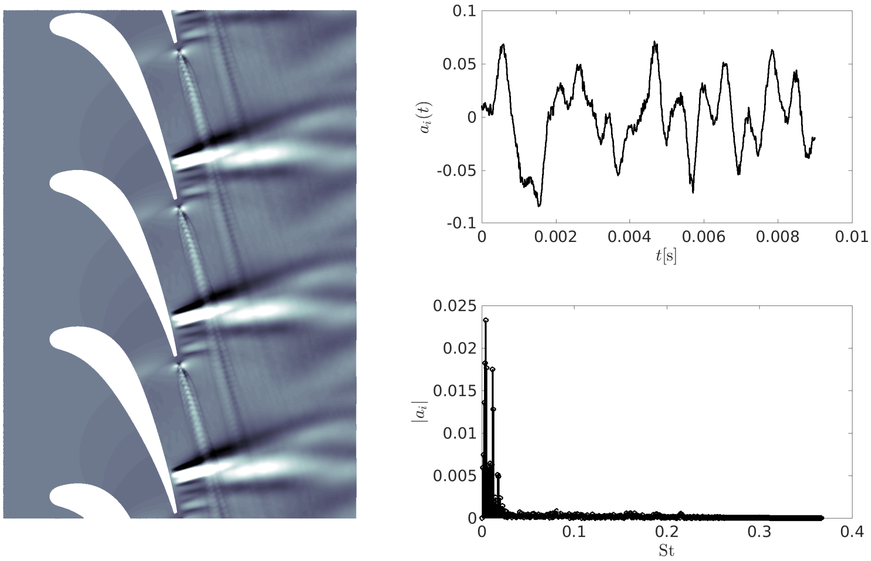

FIGURE 5.24: Fifth POD mode of the pressure fluctuation field p'; baseline case.

Looking now at the POD of the forced case, two additional modes have been found at the dominant tone $St_1 = 0.00733$, which were not present in the baseline case. The first couple is still associated with the shedding mode, but the couple $3-4$ exhibits now a topo-mode at the inlet forcing frequency f_1, associated to the shock movement. The temporal trend can be clearly visualized from the time history of the associated temporal coefficient in Figure 5.25. The chrono-mode is clearly characterized only by the forcing frequency f_1, underlining a strong correlation between

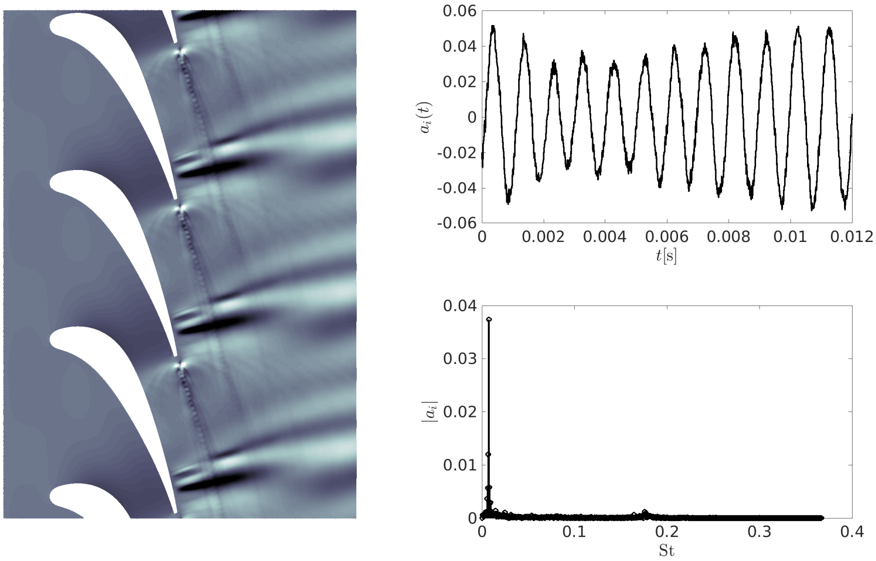

FIGURE 5.25: Third POD mode of the pressure fluctuation field p'; forced case.

the topo-mode and the presence of the forcing. From the modeshape, it is also possible to see the spatial area for which the pressure perturbations are dominant: this area corresponds to *Region* 2 highlighted in 5.11b, for which the shock movement is completely characterized at 1000[Hz].
Finally, the energy content of the POD for the forced case is shown in Figure 5.26.

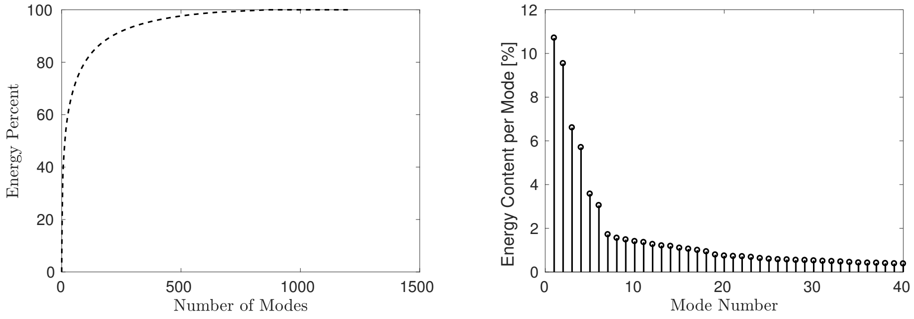

(A)

(B)

FIGURE 5.26: Energy percent retaining the first r modes (A), and energy associated to each mode (B). Pressure fluctuation field p'; forced case.

Now, the first 6 modes contain 38% of the total energy as compared to the 30% of the baseline case, with the couple $3-4$ retaining 12% of it, which was not present in the baseline simulation.

5.1.5 POD, Velocity Magnitude Field

Finally, the last POD has been conducted for the velocity magnitude field.

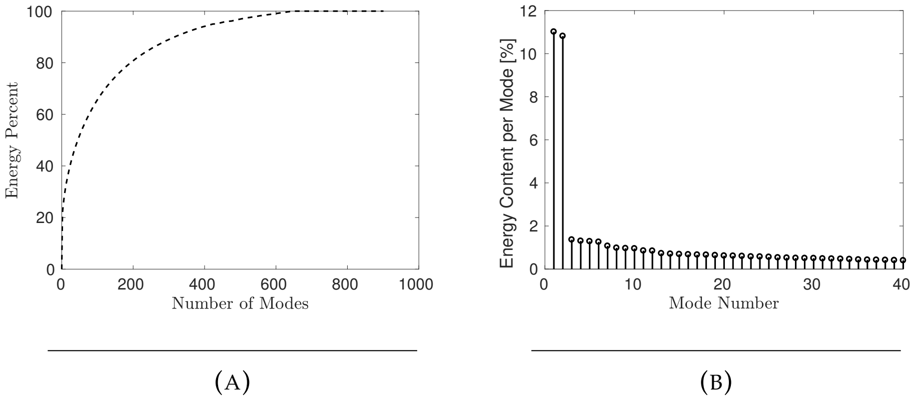

(A)

(B)

FIGURE 5.27: Energy percent retaining the first r modes (A), and energy associated to each mode (B). Velocity magnitude fluctuation field U'_{mag}; baseline case.

The baseline case shows a dominant couple of modes associated to the shedding frequency at $St = 0.176$, Figure 5.28.

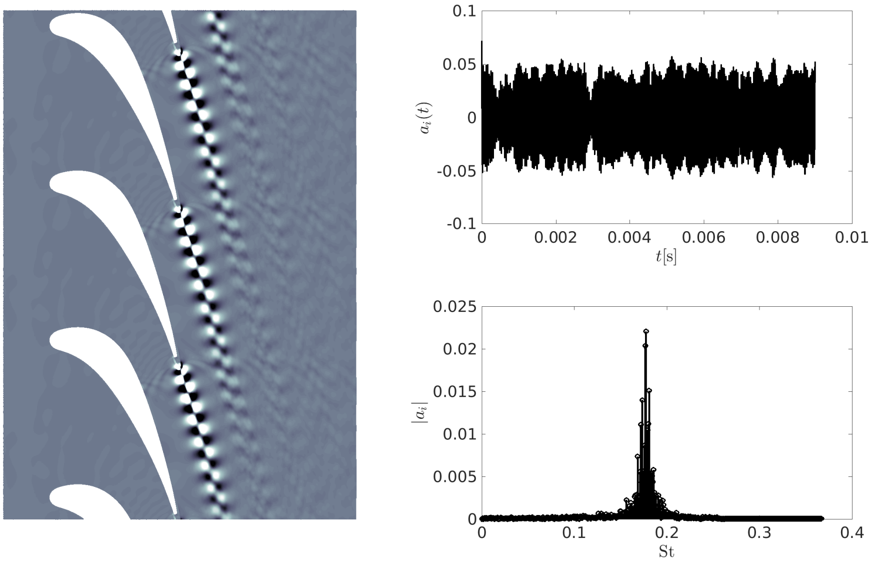

FIGURE 5.28: First POD mode of the velocity magnitude fluctuation field U'_{mag}; baseline case.

The first two modes contain 22% of the total energy as it can be seen from Figure 5.27.

The other couple of modes have an energy content below 2%. The couple $3-4$ shows a wide range low frequency dynamic mode interesting both the shock movement mechanism and the wake region; some frequency content is also present around the shedding tone $St = 0.176$. The corresponding topo- and chrono-modes are visualized in Figure 5.29.

Regarding the forced case, instead, the situation is similar to the pressure fluctuation analysis, with two modes appearing in position 3 and 4, related to the inlet forcing

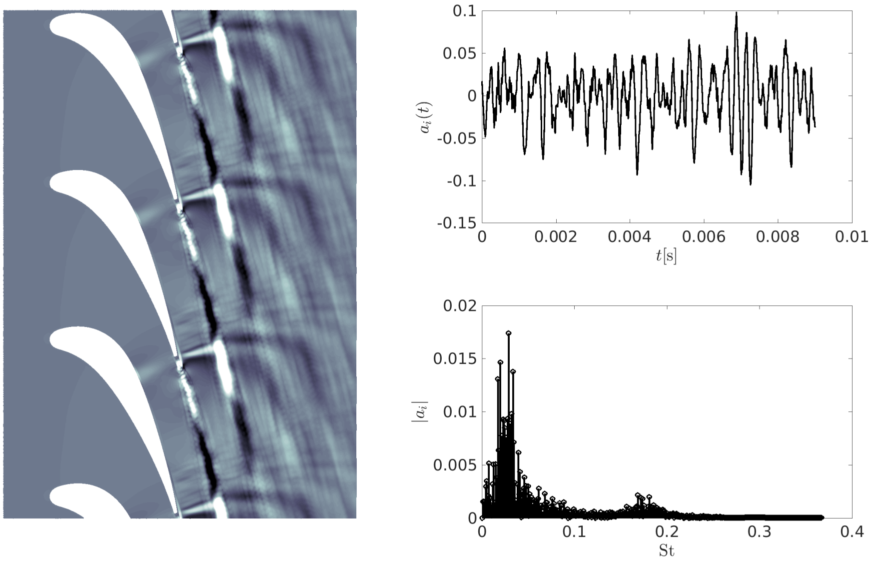

FIGURE 5.29: Third POD mode of the velocity magnitude fluctuation field U'_{mag}; baseline case.

frequency f_1. This couple contains 10% of the total energy, with the shedding associated modes still retaining 22% of the energy, Figure 5.31.
Finally, the modeshapes associated to the dominant tone $f_1 \rightarrow St_1 = 0.00733$ are shown in Figure 5.30.

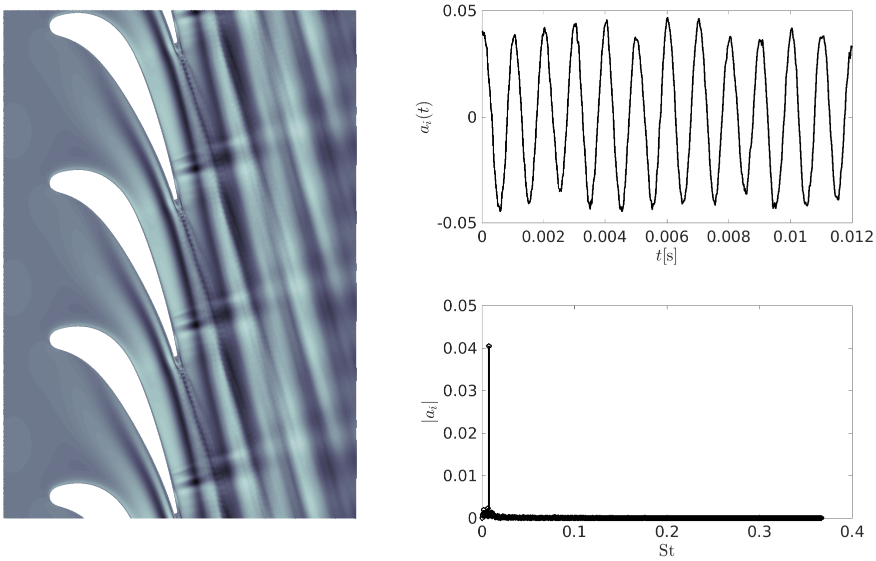

FIGURE 5.30: Third POD mode of the velocity magnitude fluctuation field U'_{mag}; forced case.

Analogously to the FFT of the forced case in Figure 5.5b, it is possible to observe the presence of distorted "*jet/streaks*"-like structures convected through the passage and the presence of the shocks.

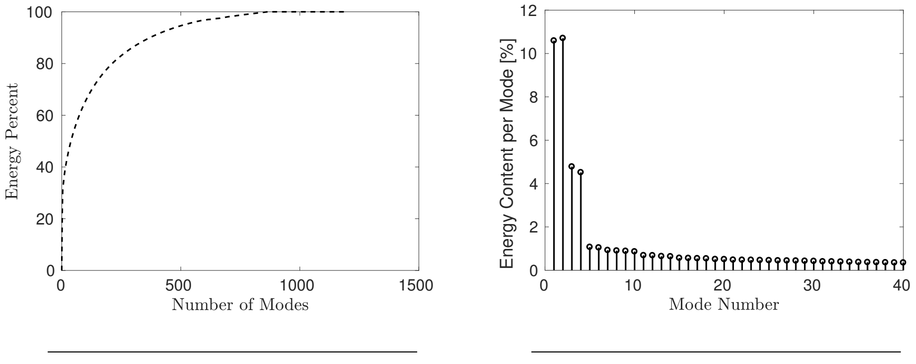

(A) (B)

FIGURE 5.31: Energy percent retaining the first r modes (A), and energy associated to each mode (B). Velocity magnitude fluctuation field U'_{mag}; forced case.

5.1.6 Inlet Temperature Effects

In the present work, a parametric study has been conducted in terms of the reference inlet temperature, in order to evaluate the generation of additional acoustic power. Moreover, the simulation setup will move towards higher inlet temperatures, simulating more realistic scenarios than the one with $T_1 = 303.15$[K].

Again the numerical setup is analogous to the one of the forced case, with the inlet static and total temperatures changing accordingly to the desired case to simulate. In addition, the specif heat ratio γ and the specific heat at constant pressure c_p will always be kept constant during the simulation, but with their values based on the selected inlet static temperatures.

The other two analyses have been performed, respectively, with the inlet temperatures being equal to $T_1 = 600$[K] and $T_1 = 900$[K].

In all simulated cases, the Mach numbers M_1 and $M_{2\text{is}}$ always keep their value of 0.15 and 0.95 respectively. The definition of the Strouhal number will change accordingly to the selected case, since sonic conditions are now based on different total temperatures and hence different velocity scales derived from $0.95M_{2\text{is}}$. In this manner it is also possible to evaluate the effects of different wavelengths of the incoming entropy waves: keeping the inlet forcing frequency ($f_1 = 1000$[Hz]) and the lenghtscale d constant, the Strouhal number associated to the incoming disturbances decreases since the velocity scale increases for higher inlet temperatures. The Strouhal number associated to f_1, for the three cases, is $St_1 = 0.00733$, $St_1 = 0.00524$ and $St_1 = 0.00431$ respectively.

The present parametric study will, therefore, be able to assess the different acoustic production mechanism as function of the ratio $\lambda_s / C_{ax,\text{mid}}$.

The same FFT and POD techniques will be applied to the resulting fields, and their results will be compared. Adequate sampling frequencies are used, for higher temperatures, in order to avoid aliasing.

Finally, the results obtained from the parametric study will be also used for comparisons with the analytical model, in section 5.2.

Figure 5.32 shows the static temperature ratio T/T_1 for the three forced simulations. At the inlet of the computational domain, the vertical stripes highlight the different

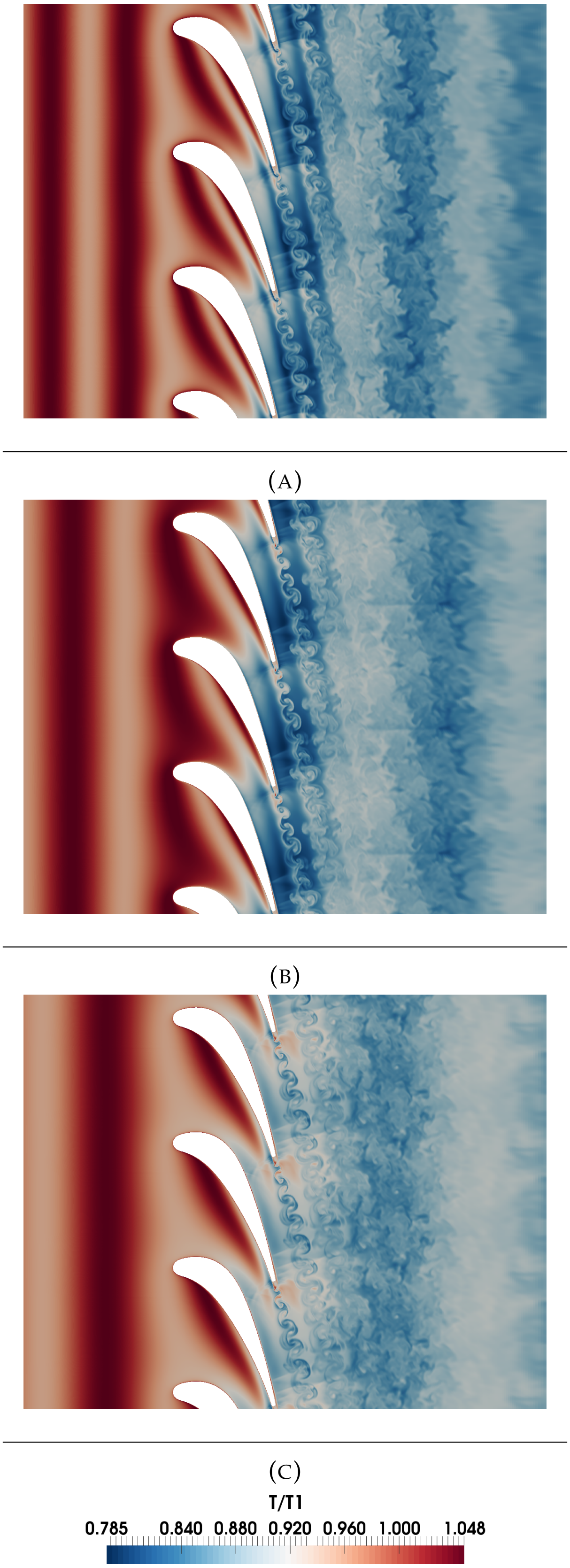
(A)

(B)

(C)

FIGURE 5.32: Instantaneous static temperature ratio T/T_1; forced inlet temperature $T_1 = 303.15$[K] (A), $T_1 = 600$[K] (B) and $T_1 = 900$[K].

wavelengths of the entropy waves, given by the dispersion relation $\lambda_s = M_1 c_1 / f_1$. Since the inlet Mach number is equal to $M_1 = 0.15$ for all cases, the local inlet speed of sound c_1 changes accordingly to its definition $c_1 = \sqrt{\gamma R T_1}$. The wavelengths normalized by the axial chord $C_{ax,\mathrm{mid}}$ are then $\lambda_s / C_{ax,\mathrm{mid}}|_{300[\mathrm{K}]} = 0.76$, $\lambda_s / C_{ax,\mathrm{mid}}|_{600[\mathrm{K}]} = 1.11$ and $\lambda_s / C_{ax,\mathrm{mid}}|_{900[\mathrm{K}]} = 1.36$. It is also possible to observe that these waves tends to return to their planar organization downstream of the vane, in all cases. The flow features are similar to the ones described in subsection 5.1.1, with the hottest spots of the entropy waves traveling more and more downstream as the wavelength λ_s increases. In fact, it is distinctly possible to notice hot spots of air convected after the sonic line in Figure 5.32c. This aspect is less evident for the other two inlet temperatures. The wake region seems also to be thicker for higher inlet temperatures. The shedding frequency increases from $f_s = 33.6[\mathrm{KHz}]$ to $f_s = 37[\mathrm{KHz}]$, for $T_1 = 600[\mathrm{K}]$ and $T_1 = 900[K]$ respectively. The associated Strhouhal numbers are $St_s = 0.173$ and $St_s = 0.16$.
The FFT of the two dimensional snapshots, at the inlet forcing frequency f_1 is now compared for the temperature and pressure fields.

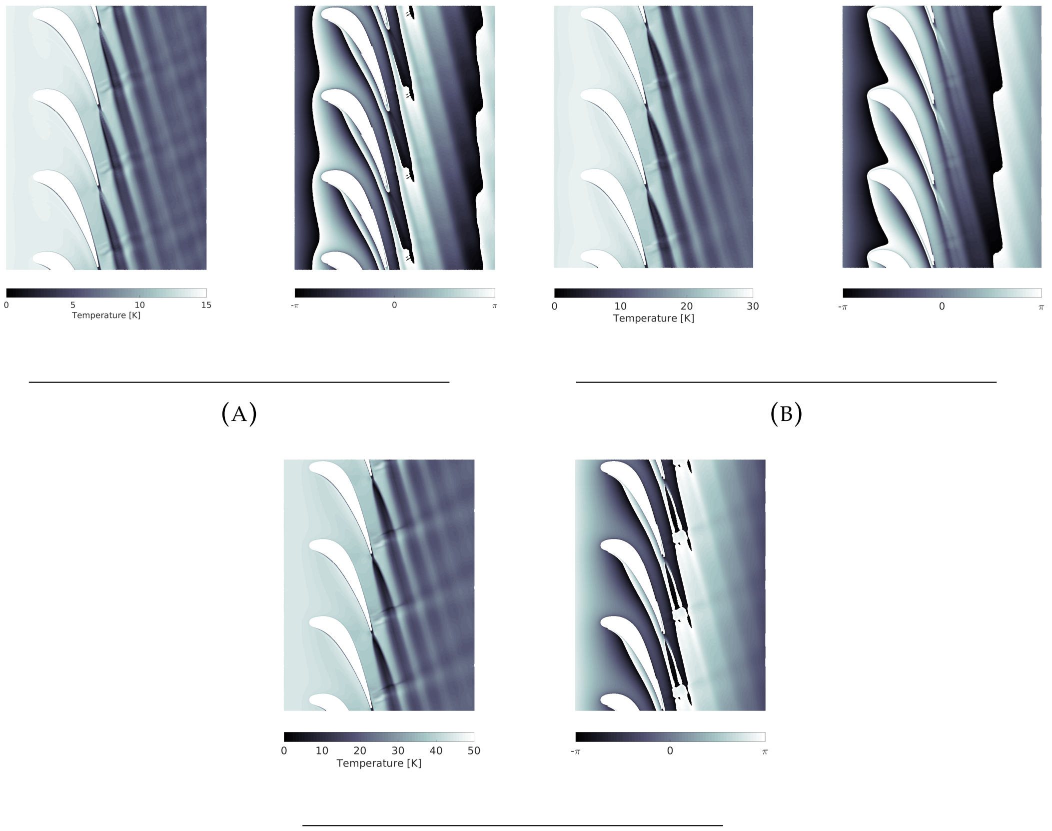

(A)

(B)

(C)

FIGURE 5.33: Amplitude (left) and phase (right) of the FFT of the temperature fluctuation field at f_1; forced inlet temperature $T_1 = 303.15[\mathrm{K}]$ (A), $T_1 = 600[\mathrm{K}]$ (B) and $T_1 = 900[\mathrm{K}]$ (C).

Starting from the temperature field, Figure 5.33, the features of the amplitude are similar for all three cases, with an increasing wake region as mentioned above. For all the forced cases, the maximum amplitude magnitude divided by its respective inlet temperature is 4.8% since the maximum temperature is registered at the inlet, where the forcing is imposed. The phase field identifies, instead, the incoming wavefronts which are then distorted and finally propagated downstream.

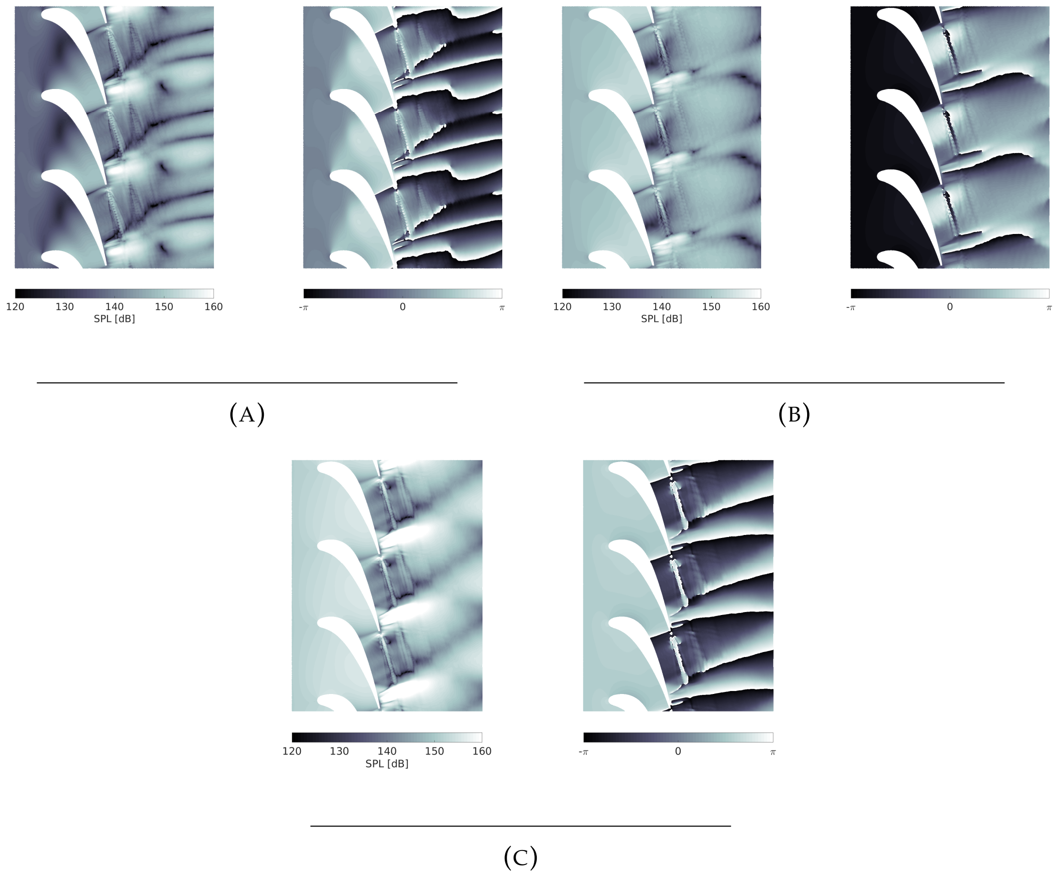

(A)

(B)

(C)

FIGURE 5.34: Amplitude (left) and phase (right) of the FFT of the pressure fluctuation field at f_1; forced inlet temperature $T_1 = 303.15[K]$ (A), $T_1 = 600[K]$ (B) and $T_1 = 900[K]$ (C).

Looking then at the amplitude field of p', it is directly possible to notice the glowing white area of high amplitudes towards the end of the blade (suction side). This zone corresponds again to the moving system of compression (weak shocks) and expansion waves. The case at $T_1 = 900[K]$ presents an outburst of the pressure field amplitude in such a zone, as it can be visualized from Figure 5.34c. The interaction of the entropy waves with the acoustic field created at f_1, becomes more and more important as the inlet static temperature increases, and hence the wavelength of the entropy waves is increased.

Moreover, the SPL in the converging portion of the vane and upstream of the blade increases as well, in accordance with the aforementioned trend. This suggest that also the entropy-to-acoustic conversion mechanism is enhanced, and the amplitude of the upstream propagating acoustic wave becomes greater and greater.

Then, it is possible to notice, in all cases, that the convergent part of the vane is decoupled from the discharge section.

Moving now the analysis to the POD of temperature and pressure field, several analogous considerations can be made.

For the temperature fluctuations, almost all the energy is contained in the first couple of modes $1-2$. This is true for all inlet temperatures. In Figure 5.35 it is possible

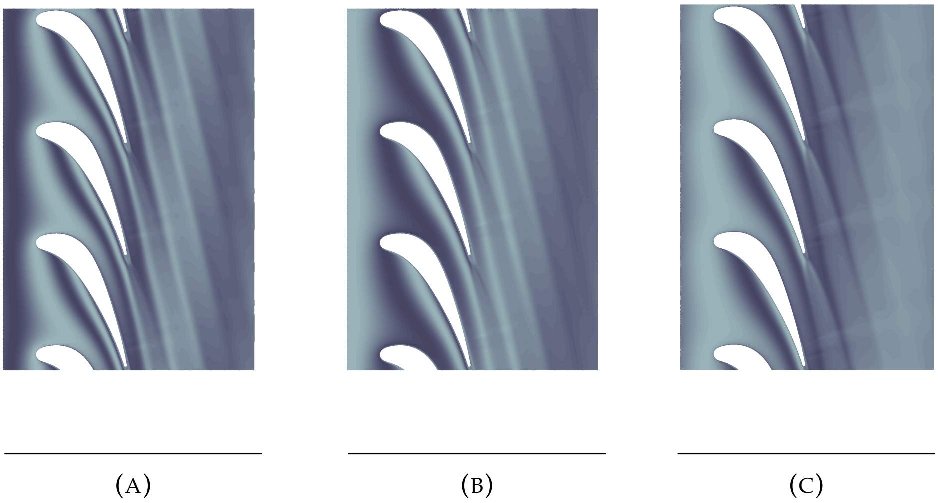
(A) (B) (C)

FIGURE 5.35: First POD topo-mode, temperature fluctuation field; forced inlet temperature $T_1 = 303.15$[K] (A), $T_1 = 600$[K] (B) and $T_1 = 900$[K] (C).

to visualize the modeshapes for all inlet temperatures; the chrono-mode is not presented since it is only a pure sinusoidal function ad 1000[Hz]. The modeshapes are very similar to each other, with incoming waves of larger wavelength and a thicker wake region as the inlet temperature increases.

For the pressure fluctuations, instead, the POD is more complex and less straight forward to interpret, since some topo-modes associated to the frequency f_1 appear also mixed to other frequencies. For the intermediate wavelength ratio $\lambda_s/C_{ax,\mathrm{mid}} = 1.11$, the first four modes are always associated with the shedding phenomenon and with the presence of coherent structures at the forcing frequency f_1. They contain 24% of the total energy but the modes are not always associated to a single frequency. This aspect can be seen in Figure 5.36.

In Figure 5.36b there is some low frequency content spread over a wider range of frequencies than Figure 5.36a, which only exhibits a dominant tone at $St_1 = 0.00524$. In addition, there is also a noticeable peak at the shedding frequency in the spectrum of the chrono-mode. The shedding features are clearly visible in the topo-mode as well. The energy content per mode is similar to the one in Figure 5.26.

For the largest wavelength $\lambda_s/C_{ax,\mathrm{mid}} = 1.36$, instead, the association of a single topo-mode to multiple temporal frequencies becomes even stronger than the previous case. There are, again, two modes which are prevalently linked to the shedding frequency $St_s = 0.16$, but they exhibit a noticeable tone at the frequency $St_1 = 0.00431$. These modes can be visualized in Figure 5.37.

The same situation happens for the topo-modes mainly associated to the frequency $St_1 = 0.00431$, as it can be seen from Figure 5.38.

The mode in Figure 5.38a shows a clear peak at $St_s = 0.16$, in addition to the one at $St_1 = 0.00431$. The enrgy content associated to the first four mode is around 55%, with the topo-modes associated to f_1 retaining $25\%$of it. All the remaining modes exhibit an energy content per mode below 2%.

From the previous analyses is then possible to draw important conclusions on the effect of the inlet reference temperature. First, it has an immediate effect on changing the wavelength of the incoming disturbances λ_s, as stated in the beginning of the present subsection. It also seems to modify the wake width downstream of the

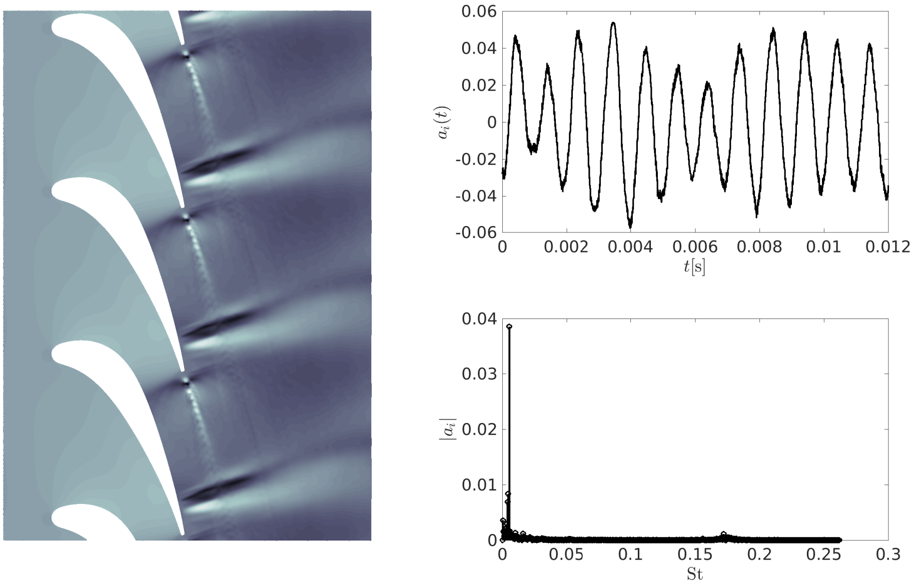

(A)

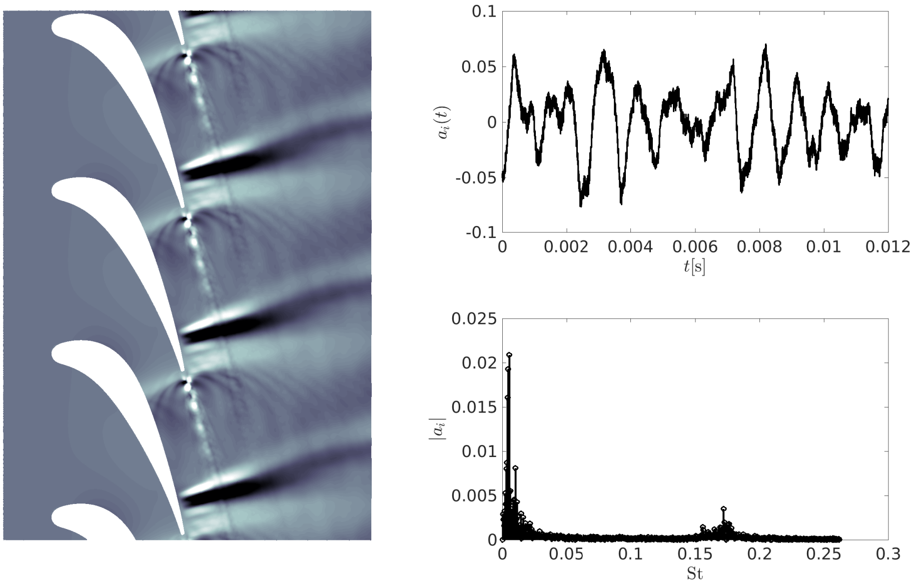

(B)

FIGURE 5.36: POD topo-modes of the pressure fluctuation field associated to f_1, (A) and (B); forced inlet temperature $T_1 = 600$[K].

blade, making it thicker as the inlet temperature increases. The shedding frequency is almost constant between the lower and the intermediate wavelengths, with the Strouhal numbers being equal to $St_s = 0.176$ and $St_s = 0.173$ respectively. The shedding frequency decreases instead at $St = 0.16$ for the largest wavelength. From the FFT of the temperature fluctuation field it is possible to see that the amplitude of the entropy waves is reduced, while they try to keep their planar character, even if

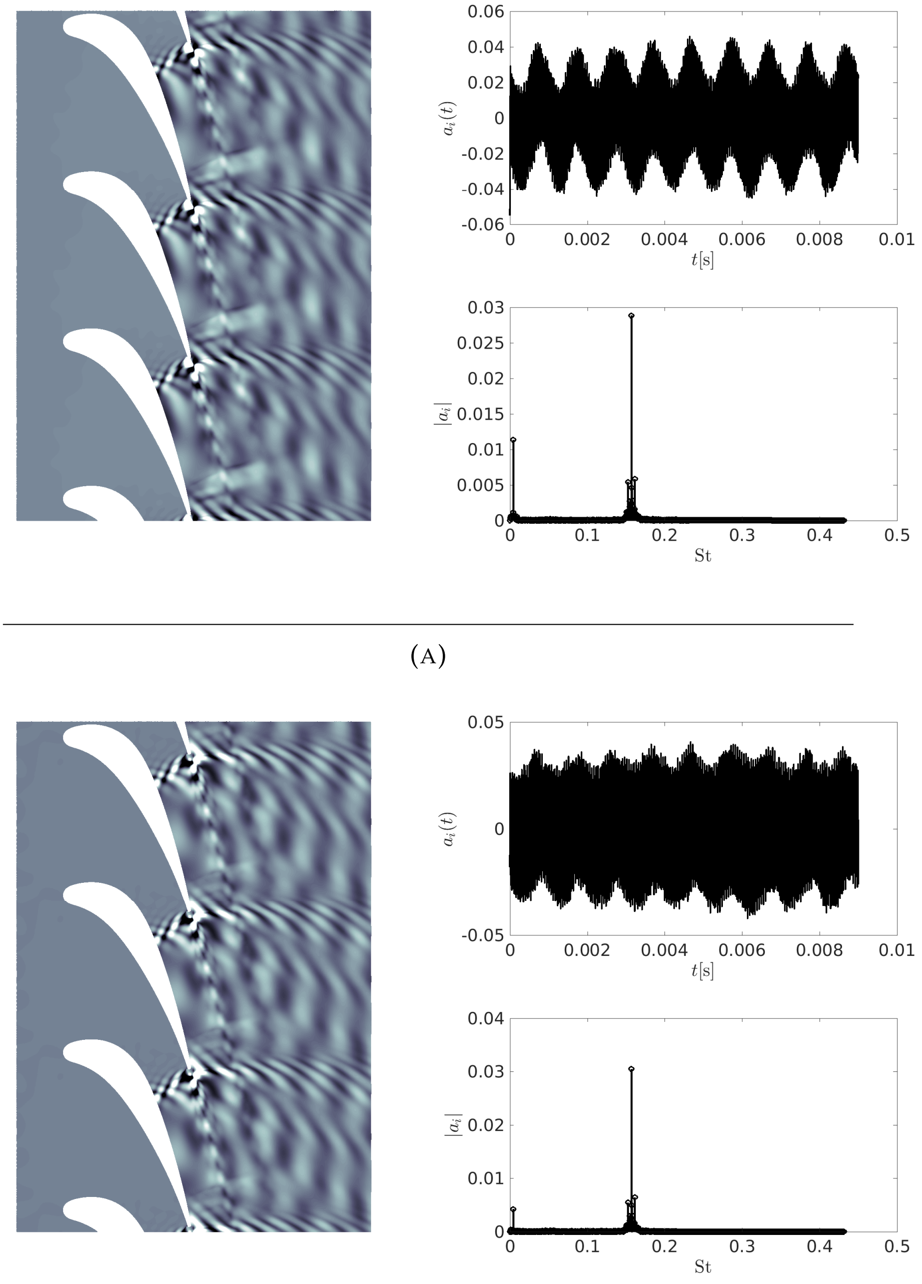

(A)

(B)

FIGURE 5.37: POD topo-modes of the pressure fluctuation field associated to the vortex shedding, (A) and (B); forced inlet temperature $T_1 = 900$[K].

they are strongly distorted across the NGV passage.
The FFT of the pressure fluctuation field, on the other hand, shows that the amplitude of the reflected acoustic waves (in terms of SPL) augments for increasing wavelengths, with the entropy-to-acoustic conversion enhanced across the vane. Moreover, it is also possible to observe that the amplitude of the downstream transmitted wave increases as well. With a particular zone of interest on the suction side of the blade, towards its end. This feature is present for all forced simulations, with

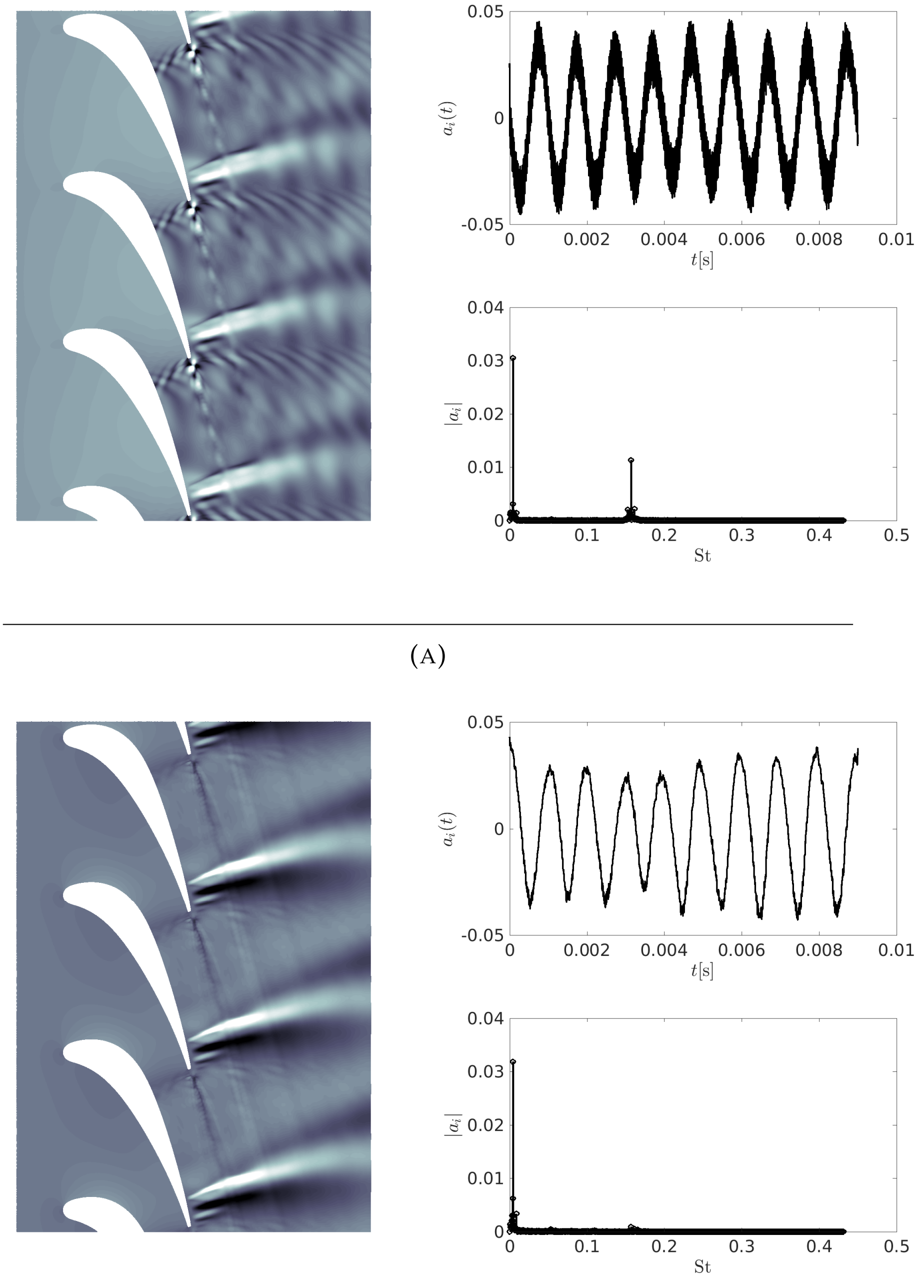

(A)

(B)

FIGURE 5.38: POD topo-modes of the pressure fluctuation field associated to f_1, (A) and (B); forced inlet temperature $T_1 = 900$[K].

an outbursting region of very high amplitudes (≥ 160[dB]) for the highest temperature (largest wavelength of the incoming disturbances).

From the POD of the temperature field, all the temporal signals of the chrono-modes associated to the inlet forcing frequency show a purely sinusoidal trend similar to the one of Figure 5.19. The associated topo-modes show very similar resemblances to their respective instantaneous fields of Figure 5.32.

The POD algorithm for the pressure fluctuation field, on the other end, is not identifying coherent structures at a single temporal frequency as the inlet temperature increases. In fact, single topo-modes are linked, in their frequency content, to both vortex shedding and coherent structures arising at f_1. The importance of the modes related to f_1, anyway, is enhanced for larger wavelengths: they can represent up to 25% of the total energy of the field p' by themselves (as in the case for the largest wavelength λ_s). In all simulations, similar POD topo- and chrono- modes appear when a fluctuating temperature is imposed at the inlet. The presence of such structures in the baseline case is not evident.

It can be concluded that additional acoustic power is created in all cases, where the inlet temperature field is forced at 1000[Hz]. The forcing is also able to excite the low frequency dynamics associated to the movement of compression and expansion waves emitted from the trailing edge.

5.2 Comparisons with the Analytical Model

In this section, the analytical model proposed by Cumpsty and Marble [18] will be described analytically. Its results will also be compared with the data collected from the simulations. The effect of the different wavelengths is also discussed, looking at how results are benchmarked with the model, as the wavelength of the entropy waves is increased.

5.2.1 Actuator Disk Model

This method was first introduced in 1977 by Cumpsty and Marble [18]; it is also possible to find an accurate analytical description in the work of Leyko *et al.* [19], related to the indirect combustion noise generated by planar entropy waves, in a subsonic stator blade-row.

The model is based on the compact assumption, i.e. the wavelength of the disturbances λ_s is much larger than the reference axial chord (in the present case $C_{ax,\text{mid}}$). The full entropy perturbation can be written in a non dimensional form as described in equation (5.1), which for small amplitude perturbations becomes

$$\frac{s'}{c_p} = \frac{T'}{T} - \frac{\gamma - 1}{\gamma}\frac{p'}{p}. \tag{5.18}$$

In the case of an inlet boundary purely forced in temperature the expression reduces to

$$\frac{s'}{c_p} = \frac{T'}{T} \tag{5.19}$$

The original model is extended to a series of stator-rotor blade rows, the present work will only deal with a single stator NGV passage.

The hypotheses of the model are summarized as follows:

- Compact assumption, $\lambda_s \gg C_{ax,\text{mid}}$.
- Low blade pitch-chord ratio, the blade details can be neglected and only the inlet and outlet flow Mach numbers and directions need to be considered.
- Subsonic axial flow.
- Radial variations are neglected, the flow is treated as two-dimensional in the axial-tangential plane.

- The acoustic power is calculated neglecting any discontinuity downstream of the turbine.
- Pressure waves are propagated from the row upstream and downstream when entropy waves interact with the turbine stage; vorticity waves, instead, are only propagated downstream.

Each flow-state, upstream and downstream, is steady, with a uniform state characterized by the flow velocity $\mathbf{w}$ of components (U, V), the direction θ, the uniform pressure p and the density ρ.
Assuming small perturbations, balance equations can be written on each side of the blade row. Then, the outgoing waves can be evaluated as functions of the incoming ones and of the main flow parameters. The waves are characterized by the wave vector $\mathbf{k}$ and by the wave angle ν. For a generic wave of the present model, the wavenumber $\mathbf{k}$ is expressed as $\mathbf{k} = [k_x, k_y]^T$; with $k_x = ||\mathbf{k}|| \cos \nu$ and $k_y = ||\mathbf{k}|| \sin \nu$. The velocity perturbation variables u' and v' can be related to the fluctuating direction θ' by the velocity triangles as

$$\frac{u'}{U} = \frac{w'}{W} - \theta' \tan \theta, \quad \frac{v'}{V} = \frac{w'}{W} + \frac{\theta'}{\tan \theta}. \tag{5.20}$$

A generic configuration can be visualized as example in Figure 5.39.

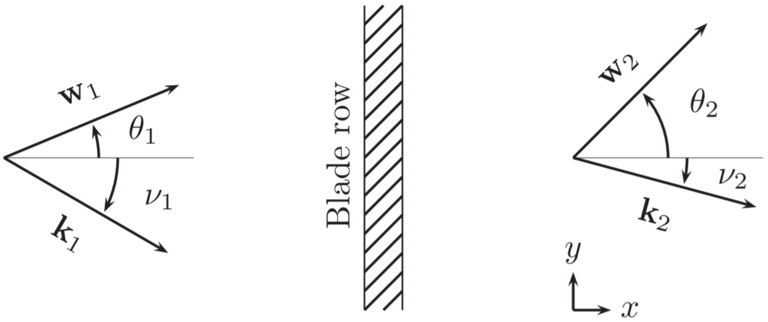

FIGURE 5.39: Schematic description of the analytical approach. $\mathbf{w}$ is the velocity vector and $\mathbf{k}$ is the wave vector. Figure from [19].

The disturbance to the uniform state consist in the vorticity wave $\xi' = \partial v'/\partial x - \partial u'/\partial y$, the entropy wave s'/c_p and the acoustic waves $p'_{\pm}/\gamma p$. Each perturbation satisfies the linearized continuity and momentum equation:

$$\frac{\mathrm{D}}{\mathrm{D}t}\left(\frac{\rho'}{\rho}\right) + \frac{\partial u'}{\partial x} + \frac{\partial v'}{\partial y} = 0, \tag{5.21}$$

$$\frac{\mathrm{D}}{\mathrm{D}t}(u') = -\frac{1}{\rho}\frac{\partial p'}{\partial x}, \tag{5.22}$$

$$\frac{\mathrm{D}}{\mathrm{D}t}(v') = -\frac{1}{\rho}\frac{\partial p'}{\partial y}. \tag{5.23}$$

They also satisfy the entropy conservation

$$\frac{\mathrm{D}}{\mathrm{D}t}\left(\frac{s'}{c_p}\right) = \frac{\mathrm{D}}{\mathrm{D}t}\left(\frac{p'}{\gamma p} - \frac{\rho'}{\rho}\right) = 0. \tag{5.24}$$

In which the operator $\mathrm{D}/\mathrm{D}t = \partial_t + U\partial_x + V\partial_y$, $U = W\cos\theta$ and $V = W\sin\theta$.
A generic entropy wave whose normal has an angle ν_s with respect to the x-axis, with wave number $\mathbf{k_s}$ and frequency f, can be written as

$$\frac{s'}{c_p} = A_s \exp[\mathrm{i}(2\pi f t - \mathbf{k_s}\cdot\mathbf{x})]. \tag{5.25}$$

This wave satisfy the entropy conservation (5.24) if the following dispersion relation holds:

$$\frac{c||\mathbf{k_s}||}{2\pi f} M\cos(\nu_s - \theta) - 1 = 0, \tag{5.26}$$

being the Mach number M calculated as $M = W/c$.
The entropy wave is not associated to any velocity field $w'_s = 0$ and no pressure field $p'_s = 0$ (while it might be coupled to an acoustic field $p'_\pm$).
The vorticity wave, on the other hand, can be derived directly from (5.22,5.23), noting that $\mathrm{D}\xi'/\mathrm{D}t = 0$. It can be written as

$$\xi' = A_\xi \exp[\mathrm{i}(2\pi f t - \mathbf{k}_\xi\cdot\mathbf{x})], \tag{5.27}$$

with the dispersion relation given by

$$\frac{c||\mathbf{k}_\xi||}{2\pi f} M\cos(\nu_\xi - \theta) - 1 = 0. \tag{5.28}$$

Since vorticity waves can be treated as divergence-free [18, 19], and they are not associated to any pressure field $p'_\xi = 0$, the resulting velocity field might be written as

$$\frac{u'_\xi}{c} = -\mathrm{i}\frac{\xi'}{c||\mathbf{k}_\xi||}\sin\nu_\xi \tag{5.29}$$

$$\frac{v'_\xi}{c} = \mathrm{i}\frac{\xi'}{c||\mathbf{k}_\xi||}\cos\nu_\xi. \tag{5.30}$$

Expressing now the velocity components u'_ξ and v'_ξ in the more convenient form of the flow variables of interest w'_ξ and θ'_ξ, it results

$$\theta'_\xi = (-u'_\xi\sin\theta + v'_\xi\cos\theta)/w, \tag{5.31}$$

$$w'_\xi = u'_\xi\cos\theta + v'_\xi\sin\theta. \tag{5.32}$$

The last pressure perturbation is defined, analogously to the previous ones, as

$$\frac{p'}{\gamma p} = A_\pm \exp[\mathrm{i}(2\pi f - \mathbf{k}_\pm\cdot\mathbf{x})]. \tag{5.33}$$

Since entropy and vorticity disturbances are described by independent solutions, acoustic waves generate an irrotational and isentropic acoustic field. The equation satisfied by the acoustic pressure field can be determined from equations (5.21 - 5.24). It results

$$\left(\frac{\mathrm{D}}{\mathrm{D}t}\right)^2\left(\frac{p'}{\gamma p}\right) - c^2\left(\frac{\partial^2}{\partial x^2} + \frac{\partial^2}{\partial y^2}\right)\left(\frac{p'}{\gamma p}\right) = 0. \tag{5.34}$$

The previous expression leads to the dispersion relation, for the acoustic wave, verified by

$$\left(1-\frac{c||\mathbf{k}_\pm||}{2\pi f}M\cos(\nu_\pm-\theta)\right)^2-\left(\frac{c||\mathbf{k}_\pm||}{2\pi f}\right)^2=0. \tag{5.35}$$

From now on, in order to avoid a long mathematical expression, a non dimensional wavenumber K will be defined as $K=c||\mathbf{k}||/2\pi f$.
In the present analytical model, the wavenumbers $k_{y,\pm}$ are real since the domain is periodic in the azimuthal direction. The wavenumbers $k_{x,\pm}$ can instead be complex and their non-dimensional counterparts read

$$K_{x,\pm}=\frac{-M\cos\theta(1-K_{y,\pm}M\sin\theta)}{1-M^2\cos^2\theta}\pm\left(\frac{(1-K_{y,\pm}M\sin\theta)^2-(1-M^2\cos^2\theta)K_{y,\pm}^2}{(1-M\cos^2\theta)^2}\right). \tag{5.36}$$

The acoustic waves $w'_\pm/c$ and $\theta'_\pm$ can now be related to the acoustic perturbation $p'_\pm/\gamma p$ by expressing $u'_\pm$ and $v'_\pm$ from the momentum equations (5.22), (5.23) and by noticing that $\rho'/\rho=p'/\gamma p$ (when considering acoustics only). They read respectively

$$\frac{w'_\pm}{c}=\frac{K_\pm\cos(\nu_{\pm-\theta})}{1-K_\pm M\cos(\nu_\pm-\theta)}\frac{p'_\pm}{\gamma p}, \tag{5.37}$$

$$\theta'_\pm=\frac{K_\pm\sin(\nu_\pm-\theta)}{M(1-K_\pm M\cos(\nu_\pm-\theta))}. \tag{5.38}$$

In the end, the contribution of all waves (entropy s, vorticity ξ and acoustic $\pm$) can be collected together into a transformation matrix linking the primitive variables to these waves:

$$\begin{bmatrix} s'/c_p \\ w'/c \\ p'/\gamma p \\ \theta' \end{bmatrix}=\mathbf{T}_w^p\begin{bmatrix} w^s \\ w^\xi \\ w^+ \\ w^- \end{bmatrix} \tag{5.39}$$

where

$$\mathbf{T}_w^p=\begin{bmatrix} 1 & 0 & 0 & 0 \\ 0 & -\mathrm{i}\frac{\sin(\nu_\xi-\theta)}{K_\xi} & \frac{K_+\cos(\nu_+-\theta)}{1-MK_+\cos(\nu_+-\theta)} & \frac{K_-\cos(\nu_--\theta)}{1-MK_-\cos(\nu_--\theta)} \\ 0 & 0 & 1 & 1 \\ 0 & \mathrm{i}\frac{\cos(\nu_\xi-\theta)}{MK_\xi} & \frac{K_+\sin(\nu_+-\theta)}{M[1-MK_+\cos(\nu_+-\theta)]} & \frac{K_-\sin(\nu_--\theta)}{M[1-MK_-\cos(\nu_--\theta)]} \end{bmatrix}, \tag{5.40}$$

represents the transformation matrix from the fluctuations to the waves.
As a further step, due to the compact assumption, matching conditions between the flow-fields upstream and downstream the cascade can be imposed. Three of the four conditions are given by conservation of entropy, continuity of mass-flow and conservation of total enthalpy. The last condition depends on the blade outlet Mach number. For subsonic flow a condition on the gas discharge angle with respect to the blade row is imposed, while for a supersonic discharge flow, a chocking condition, at the throat, is used instead.
The matching conditions will be conveniently presented in terms of the dimensionless primitive variables, with the subscript 1 and 2 indicating the states upstream and downstream the blade respectively.
Then, the entropy conservation is simply

$$\left.\frac{s'}{c_p}\right|_1=\left.\frac{s'}{c_p}\right|_2. \tag{5.41}$$

The equality of mass-flow entering and leaving the blade row requires instead

$$\left[\frac{\rho'}{\rho}+\frac{w'}{c}-\theta'\tan\theta\right]_1=\left[\frac{\rho'}{\rho}+\frac{w'}{W}-\theta'\tan\theta\right]_2. \tag{5.42}$$

The density perturbation in (5.42) might be substituted in favor of pressure and entropy changes using

$$\frac{s'}{c_p}=\frac{p'}{\gamma p}-\frac{\rho'}{\rho}. \tag{5.43}$$

Then, eliminating the entropy perturbations thanks to equation (5.41), the mass conservation becomes

$$\left[\frac{p'}{\gamma p}+\frac{1}{M}\frac{w'}{W}-\theta'\tan\theta\right]_1=\left[\frac{p'}{\gamma p}+\frac{1}{M}\frac{w'}{W}-\theta'\tan\theta\right]_2. \tag{5.44}$$

The conservation of total enthalpy implies that the quantity $c_pT+1/2W^2$ is equal at the inlet and at the outlet of the cascade. This relation is expressed as

$$\left[\frac{1}{1+\frac{1}{2}(\gamma-1)M^2}\left(\frac{T'}{T}+(\gamma-1)M\frac{w'}{c}\right)\right]_1=\left[\frac{1}{1+\frac{1}{2}(\gamma-1)M^2}\left(\frac{T'}{T}+(\gamma-1)M\frac{w'}{c}\right)\right]_2. \tag{5.45}$$

The temperature perturbations may be rewritten in terms of the entropy and acoustic ones as

$$\frac{T'}{T}=\frac{(\gamma-1)}{\gamma}\frac{p'}{p}+\frac{s'}{c_p}. \tag{5.46}$$

The equation (5.45) hence yields

$$\left[\frac{1}{1+\frac{1}{2}(\gamma-1)M^2}\left(\frac{p'}{\gamma p}+\frac{s'}{(\gamma-1)c_p}+M\frac{w'}{c}\right)\right]_1= \left[\frac{1}{1+\frac{1}{2}(\gamma-1)M^2}\left(\frac{p'}{\gamma p}+\frac{s'}{(\gamma-1)c_p}+M\frac{w'}{c}\right)\right]_2. \tag{5.47}$$

The final matching condition is chosen depending upon whether the discharge flow of the considered turbine stator is subsonic or supersonic. When the discharge flow is subsonic, the natural Kutta condition prescribed by Cumpsty and Marble [18] is specified as

$$\theta_2'=0, \tag{5.48}$$

or more generally

$$\theta_2'=\alpha\theta_1', \tag{5.49}$$

in which α is a real constant determined experimentally. Contrariwise, if the discharge flow is supersonic, there exist a sonic throat within each vane, which behaves like a quasi-steady chocked nozzle. The critical mass-flow per unit area is determined entirely by the approaching flow [18] and is proportional to

$$\dot{m}_{cr}\propto\left[pT^{-1/2}\left(1+\frac{1}{2}(\gamma-1)M^2\right)^{\frac{\gamma+1}{2(\gamma-1)}}\right]_1. \tag{5.50}$$

The variation in mass-flow rate $m'/m|_1$ is given by

$$\left[\frac{p'}{p}-\frac{1}{2}\left(\frac{1+\frac{1}{2}(\gamma+1)M^2}{1+\frac{1}{2}(\gamma-1)M^2}\right)\frac{T'}{T}+\frac{\frac{1}{2}(\gamma+1)M^2}{1+\frac{1}{2}(\gamma-1)M^2}\frac{w'}{c}\right]_1, \tag{5.51}$$

and it must be equal to the left hand side of equation (5.42). Equating the two expressions, the final matching condition, after some manipulations and reductions [18], is

$$\left[\frac{\gamma-1}{2}\frac{p'}{\gamma p}+\frac{1}{2}\frac{s'}{c_p}-\frac{1}{M}\frac{w'}{c}+\frac{1+\frac{1}{2}(\gamma-1)M^2}{1-M^2}\theta'\tan\theta\right]_1=0. \tag{5.52}$$

For the present study the fourth matching condition will be the one corresponding to the presence of a sonic throat across the NGV passage. The supersonic discharge Mach number is chosen to be equal to $M_2 = 1.05$ (just above sonic conditions) in order to apply the analytical model with supersonic discharge.

The set of equations (5.41), (5.44), (5.47) and (5.52) form a complete description for a generic stator blade row.

These matching conditions can be rewritten in a matrix form that relates the fluctuating primitive variables at the inlet and at the outlet of the blade row:

$$\mathbf{M_1}\begin{bmatrix} s'/c_p \\ w'/c \\ p'/\gamma p \\ \theta' \end{bmatrix}_1 = \mathbf{M_2}\begin{bmatrix} s'/c_p \\ w'/c \\ p'/\gamma p \\ \theta' \end{bmatrix}_2 , \tag{5.53}$$

with

$$\mathbf{M_1} = \begin{bmatrix} 1 & 0 & 0 & 0 \\ -1 & 1/M_1 & 1 & -\tan\theta_1 \\ \eta_1/(\gamma-1) & M_1\eta_1 & \eta_1 & 0 \\ 1/2 & -1/M_1 & (\gamma-1)/2 & \tan\theta_1/[\eta_1(1-M_1^2)] \end{bmatrix} , \tag{5.54}$$

and

$$\mathbf{M_2} = \begin{bmatrix} 1 & 0 & 0 & 0 \\ -1 & 1/M_2 & 1 & -\tan\theta_2 \\ \eta_2/(\gamma-1) & M_2\eta_2 & \eta_2 & 0 \\ 0 & 0 & 0 & 0 \end{bmatrix} , \tag{5.55}$$

where $\eta = (1+(\gamma-1)M^2/2)^{-1}$. The matrix $\mathbf{M_2}$ contains zeros in the last row, constituting a singularity and restricting the way in which they could be handled.

The final problem in terms of the upstream and downstream waves can be then expressed as

$$\mathbf{M_1}\mathbf{T^p_{w1}}\begin{bmatrix} w^s \\ w^\xi \\ w^+ \\ w^- \end{bmatrix}_1 = \mathbf{M_2}\mathbf{T^p_{w2}}\begin{bmatrix} w^s \\ w^\xi \\ w^+ \\ w^- \end{bmatrix}_2 . \tag{5.56}$$

The solution requires that the output variables are expressed in terms of the four inputs. The upstream vector contains three inputs w_1^+, w_1^ξ and w_1^s, while the reflected acoustic wave w_1^- is an output. Diametrically, the downstream vector contains the outputs w_2^+, w_2^ξ and w_2^s, and the input w_2^-.

However, the terms on the respective matrices $\mathbf{M_i}$, $\mathbf{T^p_{wi}}$ can be rearranged such that the vector of inputs and outputs are respectively on the correct side of the formulation:

$$\begin{bmatrix} (w^s)_2 \\ (w^\xi)_2 \\ (w^+)_2 \\ (w^-)_1 \end{bmatrix} = \mathbf{A_{out}}^{-1}\mathbf{A_{in}}\begin{bmatrix} (w^s)_1 \\ (w^\xi)_1 \\ (w^+)_1 \\ (w^-)_2 \end{bmatrix} \tag{5.57}$$

Normally, the matrix $\mathbf{A}_{\mathbf{out}}$ will not be singular.
The general expression of the output waves, in the most general case, is rather cumbersome. In subsection 5.2.2, however, the simplified case of incoming planar entropy waves will be threated. That is $k_y = 0$ and the only present disturbance is $w_1^s \neq 0$, while $w_1^\xi = w_1^+ = w_2^- = 0$.

5.2.2 Incoming Planar Entropy Waves

The present work will only deal with forced planar entropy waves, $k_y = 0$. Moreover, only the temperature field is forced at the inlet, hence the other incoming disturbances are set to be equal to zero: i.e. only $w_1^s \neq 0$.
Therefore, the relations of subsection 5.2.1, in terms of their respective waves, are simplified and the acoustic response of the blade row is analytically easy to treat.
Starting from the entropy conservation, equation (5.41) simply becomes

$$w^s|_1 = w^s|_2. \tag{5.58}$$

Then, from the relation imposing the chocked mass-flow a the throat, it is possible to derive the coefficient w_1^-/w_1^s. From the dispersion relation it results

$$K_i^+ = \frac{1}{1 + M_i \cos\theta_i} \tag{5.59}$$

$$K_i^- = -\frac{1}{1 - M_i \cos\theta_i}. \tag{5.60}$$

Imposing $w_1^+ = w_1^\xi = w_2^- = 0$, relation (5.52) yields to

$$\frac{\gamma - 1}{2}(w_1^-) + \frac{1}{2} w_1^s - \frac{1}{M_1}\left[\frac{K_1^- \cos\theta_1}{1 - M_1 K_1^- \cos\theta_1}\right] w_1^- + \frac{\tan\theta_1}{\eta_1(1 - M_1^2)}\left[\frac{K_1^-(-\sin\theta_1)}{M_1(1 - M_1 K_1^- \cos\theta_1)}\right] w_1^- = 0, \tag{5.61}$$

which for the dispersion relations in (5.59, 5.60), simply yields to

$$\frac{w_1^-}{w_1^s} = -\frac{1}{2}\left[\frac{\gamma - 1}{2} + \frac{\cos\theta_1}{M_1} + \frac{\sin\theta_1 \tan\theta_1}{\eta_1 M_1 (1 - M_1^2)}\right]^{-1}. \tag{5.62}$$

The other relations are analogous to the ones found by Leyko *et al.* [19] in their work assessing the indirect combustion noise mechanism for subsonic blade rows. With the same simplifications as before, the mass conservation simply becomes

$$w_1^- \left(1 - \frac{1}{M_1 \cos\theta_1}\right) = w_2^+ \left(1 + \frac{1}{M_2 \cos\theta_2}\right), \tag{5.63}$$

which leads to

$$\frac{w_2^+}{w_1^s} = \frac{1 - \frac{1}{M_1 \cos\theta_1}}{1 + \frac{1}{M_2 \cos\theta_2}} \frac{w_1^-}{w_1^s}. \tag{5.64}$$

Finally, the enthalpy conservation will lead to the expression for the generated vorticity wave w_2^ξ, which is of none interest for the present analysis.
For fixed Mach numbers $M_1 = 0.15$, $M_2 = 1.05$ and specific heat ratio $\gamma = 1.4$, the reflection (5.62) and transmission (5.64) coefficient of the acoustic wave are now plotted as function of the incoming and discharge directions of the flow, i.e. θ_1 and θ_2. As it can be seen from Figure 5.40, the reflected wave only depends on the inflow

angle θ_1. The red dot highlights the coefficient for the geometry adopted in the simulations, i.e. $\theta_1 = 0$.

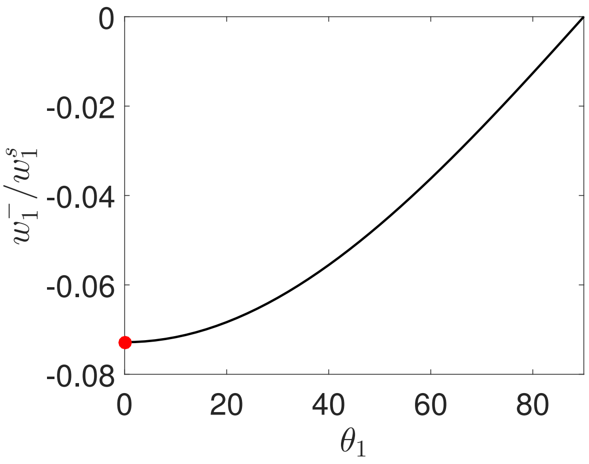

FIGURE 5.40: Reflected acoustic wave generated by an incoming entropy wave; (—) analytical model, (●) actual geometry.

For the transmitted wave, instead, the results depends on both incoming and discharge directions. Figure 5.41 show the results of the analytical model. Again the red dot refers to the actual geometry of the study, with $\theta_2 = 75$.

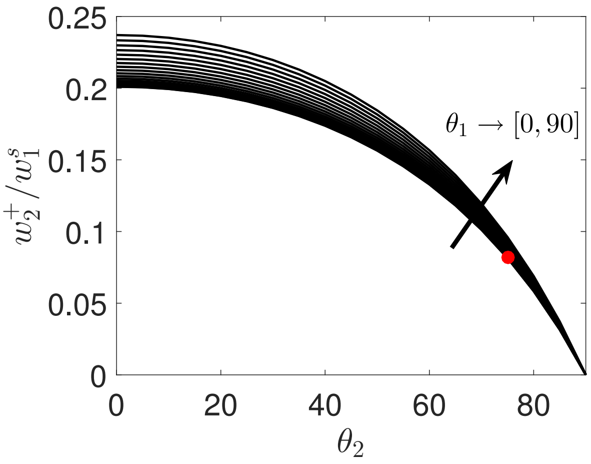

FIGURE 5.41: Transmitted acoustic wave generated by an incoming entropy wave; (—) analytical model, (●) actual geometry.

The value of the transmission coefficient is $w_2^+/w_1^s = 0.088$, while the reflection one is $w_1^-/w_1^s = 0.073$. This results will be compared to the numerical simulation in the next subsection 5.2.3.

5.2.3 Comparison of the Results

The calculation of the acoustic coefficients was performed on two planes orthogonal to the $x-$axis, respectively $x/C_{ax,\text{mid}} = -1.25$ upstream and $x/C_{ax,\text{mid}} = 1.90$ downstream of the vane. A schematic representation of those planes can be visualized in

Figure 5.42. The upstream plane will be referred as plane 1, while the downstream plane will be labeled as plane 2.

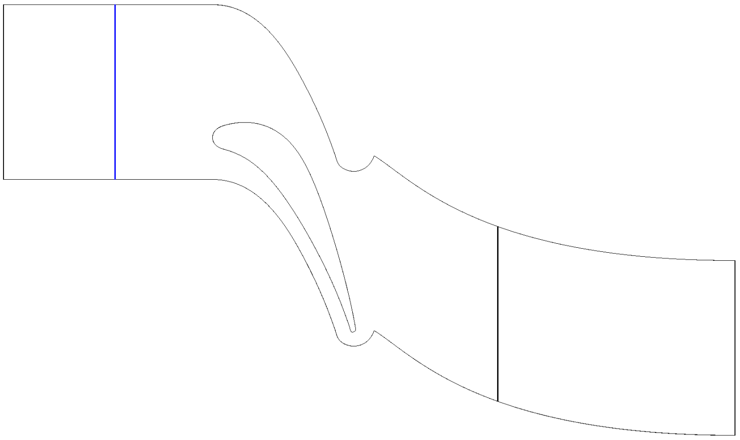

FIGURE 5.42: Azimuthal planes adopted for the evaluation of acoustic coefficients; (—) upstream plane 1, (—) downstream plane 2.

Flow variables were sampled on the planes of interest by the means of 75 local probes, with a sampling frequency varying accordingly to the simulated case. The flow quantities were also averaged in the $z-$direction. For both cases at $T_1 = 303.15$[K] and for the intermediate temperature $T_1 = 600$[K], the sampling frequency was set to $f = 500$[KHz]. In this way frequencies up to $7.5 \div 10$ the shedding frequency were captured with great margin. The sampling frequency was doubled to $f = 1000$[KHz] for the case with the highest temperature $T_1 = 900$[K].

In order to show the presence of additional generated acoustic power, first the unforced and forced case at $T_1 = 303.15$[K] will be compared in terms of sound pressure level and temperature amplitudes at $f_1 = 1000$[Hz].

Starting from the average spectrum (over all probes) of the temperature fluctuation field on plane 1, from Figure 5.43a it is immediate to identify the peak at $St_1 = 0.00733$ for the forced case. Its amplitude corresponds to 4.8% of the inlet static temperature. No comparable amplitudes, instead, were found for the baseline case. In fact it is barely possible to see the dashed line, highlighting the spectrum of the baseline case in Figure 5.43. On the other hand, for plane 2, it is possible to see from Figure 5.43b, that the entropy wave is attenuated downstream of the blade, while the greatest amplitude in the entire spectrum is still registered for St_1.

Figure 5.44 shows instead the pitchwise character of these waves on their respective upstream and downstream planes. The pitchwise location is normalized by the blade to blade distance H, and goes from the lower periodic boundary $y/H = 0$ to the upper periodic boundary $y/H = 1$.

Again, for the baseline case, no comparable amplitudes are found also in the pitchwise distribution. The entropy wave is perfectly planar in the upstream part. This can be expected since the flow is completely uniform in this region. Instead, the wave loses its perfectly planar character on the plane downstream of the NGV passage. Once more, it is possible to see that the amplitude of the entropy waves is reduced on plane 2.

Looking now at the SPL produced upstream and downstream, several conclusion

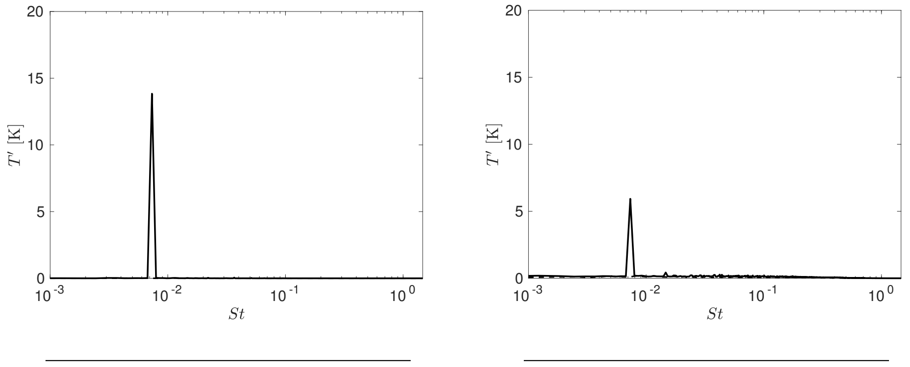

(A) (B)

FIGURE 5.43: Average spectrum of the forced temperature wave at plane 1 (A) and at plane 2 (B), $T_1 = 303.15$[K]; (- -) baseline case, (—) forced case.

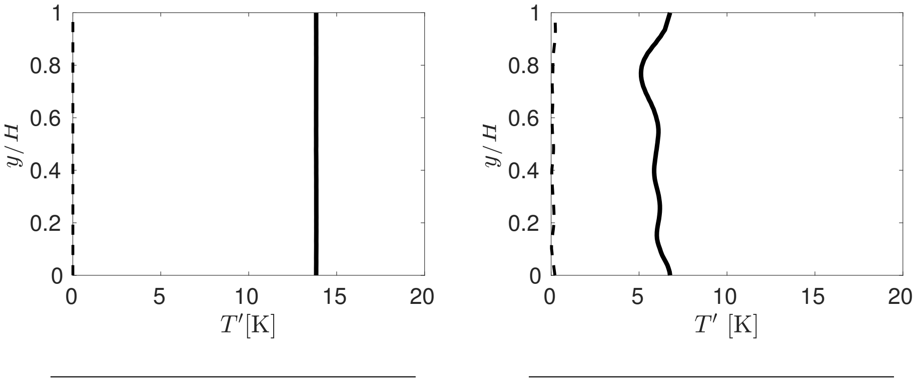

(A) (B)

FIGURE 5.44: Pitchwise distribution at the frequency St_1 of the temperature wave amplitude at plane 1 (A) and at plane 2 (B), $T_1 = 303.15$[K]; (- -) baseline case, (—) forced case.

can be drawn on the additional acoustic power generated at the inlet forcing frequency corresponding to St_1.

First, the average spectrum of the SPL upstream and downstream of the blade is presented in Figure 5.45.

It is possible to see the presence of a tone at St_1 on both planes. This time, in contrast with the temperature field, it is possible to observe the presence of low frequency contents even for the baseline case.

The pitchwise distribution of the SPL is then shown in Figure 5.46.

In accordance to the results of the temperature field, pressure waves are also planar upstream of the vane, due to the uniformity of the flow. It is clearly possible to visualize the presence of additional acoustics created upstream, Figure 5.46a. In fact, the difference in SPL between the baseline and the forced case is ≥ 20[dB]. Additional acoustic power is also generated downstream of the passage as it can be seen from Figure 5.46b. However, in this case, the acoustic wave is far from planar, with the presence of dark zones, which are also visible in the amplitude field of the FFT in Figure 5.3b. Differences ≥ 15[dB] are also registered for the SPL on plane 2.

The upstream and downstream spectra of the pressure fluctuation field are shown in Figures 5.47,5.48 for the two temperatures of 600[K] and 900[K] respectively. Again,

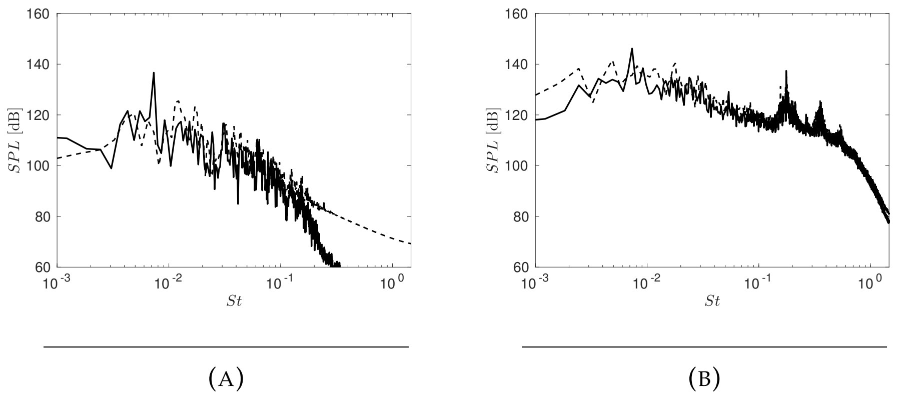

(A)

(B)

FIGURE 5.45: Average spectrum of the SPL at plane 1 (A) and at plane 2 (B), $T_1 = 303.15[\mathrm{K}]$; (- -) baseline case, (—) forced case.

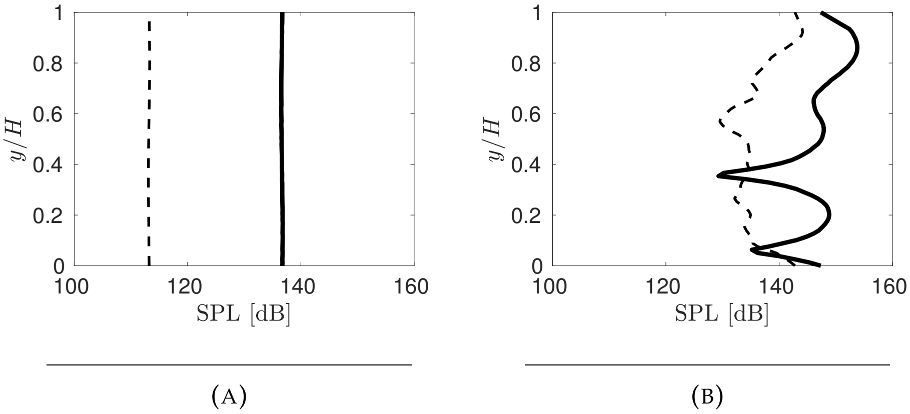

(A)

(B)

FIGURE 5.46: Pitchwise distribution at the frequency St_1 of the SPL at plane 1 (A) and at plane 2 (B), $T_1 = 303.15[\mathrm{K}]$; (- -) baseline case, (—) forced case.

two peaks are present both upstream and downstream of the passage at the respective frequency identified by St_1. Notable amplitudes at the low frequency range are still present for both temperatures, even for the baseline case.
At this point, after having shown the presence of an effective additional generated acoustic field, the analytical model will be compared with the results of numerical simulations. In this analysis the specific heat ratio γ will be changed accordingly to the simulated case. For the coefficients of the analytical model, the parameter γ as a minor influence on the results, therefore only one value will be reported. The expression used for the entropy and the acoustic waves are the ones used in equations (5.18,5.33). The amplitude of these coefficient was averaged over the plane of interest in order to get a single coefficient at a specific frequency.
The final results are compared in table 5.2. Some considerations can be made in terms of the amplitude of these coefficients and in relation to their trend with increasing wavelengths of the incoming disturbances.
The value of the transmitted entropy wave w_2^s/w_1^s is less then unity for all simulated cases, but it increases as the wavelength λ_s increases. Two might be the reasons for that behavior: first the compact assumption might not hold for the present cases and therefore the results are not in accordance with the analytical model; second, there

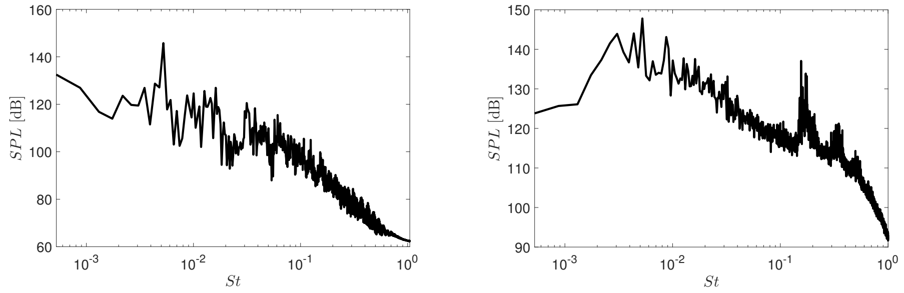

(A) (B)

FIGURE 5.47: Average spectrum of the SPL at plane 1 (A) and at plane 2 (B), $T_1 = 600$[K].

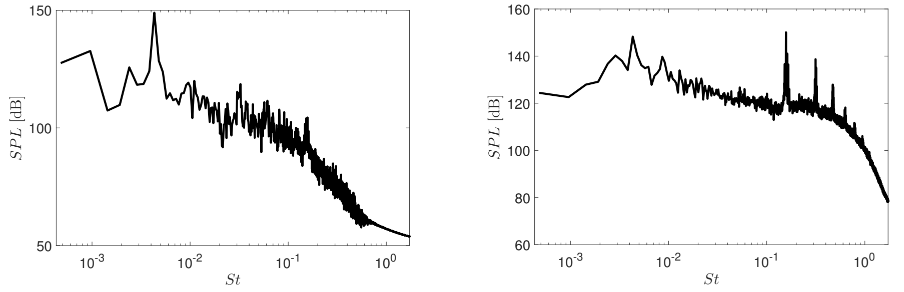

(A) (B)

FIGURE 5.48: Average spectrum of the SPL at plane 1 (A) and at plane 2 (B), $T_1 = 900$[K].

might be, in transonic conditions, sources of losses which do not verify entropy conservation across the vane passage.
For the acoustic reflected coefficient w_1^-/w_1^s, instead, the value increase monotonically for higher wavelengths. This aspect suggest that moving towards higher ratios of $\lambda_s/C_{ax,\mathrm{mid}}$, the coefficients are in closer agreement with the analytical model, which is based on the compact assumption.

TABLE 5.2: Acoustic/Entropy wave coefficients

T_1	f_1	St_1	$\lambda_s/C_{ax,\mathrm{mid}}$	w_1^-/w_1^s	w_2^+/w_1^s	w_2^s/w_1^s
303.15[K]	1000[Hz]	0.00733	0.76	0.011	0.068	0.45
600.00[K]	1000[Hz]	0.00524	1.11	0.032	0.075	0.50
900.00[K]	1000[Hz]	0.00431	1.36	0.047	0.084	0.51
Analytical Model	–	–	$\to \infty$	0.073	0.088	1.00

Finally, for the transmitted acoustic coefficient w_2^+/w_1^s, its value increases again monotonically for higher wavelengths. For the simulated transonic conditions, there might be flow features which interacts stronger with the system of incoming entropy waves, as the wavelength λ_s increase. A good example is the interaction with the system of compression and expansion waves that are emitted from the trailing edge. In this case, one can observe that the transmitted acoustic wave associated to the largest wavelengths is close to the value predicted by the analytical model. As the λ_s is further increased, it might be possible that this coefficients becomes greater and greater, underlining additional generated noise in transonic/supersonic conditions. For all cases, the SPL amplitude field exhibits region of great amplitudes as it can be seen from Figure 5.34.

Chapter 6

Conclusions

6.1 Conclusions and Future Work

The indirect combustion noise generation mechanism has been addressed by the means of 3D LES for a simplified Nozzle Guide Vane passage of a high pressure turbine. The solver adopted for the simulations was first validated against experimental data available for off-design transonic conditions without temperature forcing. Overall the numerical results are in very good agreement with experimental data. The larger discrepancies were only found in terms of maximum total pressure losses which might be due to the simplified 2D-extruded geometry adopted, for which the wake mixing might not be enhanced as in the real case scenario. In the core part of the work (Chapter 5), a pulsating entropy wave-train was imposed at the inlet of the domain to simulate temperature non-uniformities coming from the combustion chamber. The resulting flow-field was analyzed using FFT of two-dimensional sections sampled during the simulation. At the forcing frequency imposed at the inlet, several zones of the fluid domain responds with high amplitudes of the pressure fluctuations, which are not present in the baseline case. The response of the NGV passage is stronger as the wavelength λ_s of the incoming disturbances is increased. Moreover, this aspect is corroborated by the analysis performed via the Proper Orthogonal Decomposition method: the baseline case did not show any particular coherent structure at the inlet forcing frequency f_1, St_1; while pressure and temperature fields of the forced cases all showed the presence of high energy modes at that particular frequency. Moreover, the combination of the POD topo- and chrono-modes was in accordance with the results found by the sampled shock line identifying the movement of compression and expansion waves emitted from the trailing edge. For the pressure fluctuation field, the chrono-modes identified the characteristic frequency content, while the topo-modes identified the zones with the highest response of the fluctuation. Several topo-modes, both for the baseline and the forced case, corresponded to *Region* 1, 2 and 3 highlighted respectively in Figure 5.10. It is also worth to mention that the POD analysis was not always able to relate the topo-modes to a single temporal frequency.

An interesting feature was also observed regarding the system of shocks emitted from the trailing edge: three regions of interest involving the shocks movement were identified. *Region* 1 corresponded to the location $x/C_{ax,\mathrm{mid}} \approx 0.96$ where the position of the shock changes slowly during time; the region has fairly similar characteristics for both the baseline and the forced case. It is the zone characterized by the lowest frequency content. *Region* 2, instead, corresponds to the region for which the amplitude of the pressure fluctuations is the highest. For the forced case, black stripes at regular intervals of time are visible in *Region* 2 in the detail of Figure 5.11b. The frequency of these intervals is evaluated by the means of a FFT at a fixed position in space: it corresponds exactly to the inlet forcing frequency $f_1 = 1000$[Hz]. Remarkably, this characteristic does not appear for the baseline case and the shock movement is not organized at any particular frequency of interest. *Region* 3 corresponds to the initial part of the wake, towards the trailing edge at $x/C_{ax,\mathrm{mid}} \approx 1.03$, where compression and expansion waves are emitted by turbulent structures and appear with higher frequencies compared to the two other regions. These aspects of the shock dynamics in *Region* 2 justify the high amplitude found by the FFT of the pressure fluctuation field at 1000[Hz]. The shock movement mechanism was also experienced and commented in literature by other authors, e.g. by the work of Panda [56] and by the work of Risborg & Soria [57].

Finally, reflection and transmission coefficients were compared to analytical models available in literature [18]. The 3D simulations show that the entropy waves are highly distorted by the passage and lose their strength. This can be addressed from the entropy wave transmission coefficient which is reduced significantly for all the wavelengths of the incoming disturbances. The hypothesis of entropy conservation assumed by the analytical model might not hold in the case of transonic/supersonic conditions and with short incoming entropy waves. The reflected acoustic wave, instead, is weaker than the one predicted by the compact theory for all simulations. However, the reflected acoustic coefficient increases towards the analytical one as λ_s increases. This might be also due to the decoupled dynamics of the convergent part of the NGV from the discharge section: in fact the throat is sonic and downstream generated noise cannot propagate backwards. Finally, the transmitted acoustic wave is in fairly good agreement with the analytical model, and the transmission coefficient assumes also larger values for the higher wavelengths λ_s, suggesting the presence of flow features, in transonic conditions, which might generate additional noise. An example is the dynamics of the compression/expansion waves emitted from the trailing edge, which interacts with the incoming entropy waves.

The transmitted acoustic wave is the main contributor to the generated indirect combustion noise.

Regarding the possible continuations of the work, a complete characterization of indirect combustion noise of a complete HPT stage (stator plus rotor) remains an important aspect. This type of analysis might include also the simulation of the combustion chamber coupled to the turbine stage. In alternative to the complete combustion chamber, a frequency spectrum extracted from the latter might be imposed together with the presence of free-stream turbulence, with larger wavelengths, such that $\lambda/C_{ax,\mathrm{mid}} \sim 10$. This type of simulation will constitute a simulation scenario very close to the real case.

Last, further investigation on the entropy to acoustic conversion mechanism in transonic/supersonic condition will also suggest major insights for indirect combustion noise generation.

Appendix A

Scalability Performances of *foam-extend*

In order to decide the optimal number of cores to use for the simulations, a scalability test has been performed with the solver *dbnsTurbFoam*. This study allowed the selection of the index identifying the lowest number of cells per core for which the code was still halving the solving time, while doubling the number of cores.
The analysis was performed on a test-case based on a 3D RANS simulation with the same settings of the baseline case (section 4.2).
The simulations were conducted on a reduced mesh size, with only 32 layers in the $z-$direction. The total number of elements was, then, equal to $739500 \times 32 = 23664000$. The simulated cases of the scalability test run for a total of 10000 iterations, in order to consider negligible the time required for the case initialization. One iterations consist in the complete solution of one physical time-step of $\Delta t = 1e^{-9}$[s], according to the solution algorithm described in subsection 3.3.6. Two main performance indices were assessed: first, the proportionality of the computational time per iteration required for the simulation with respect to the number of cores adopted; second, the efficiency of the code, measured in seconds per iteration divided by cells per core. Six simulations were performed with the only difference being the number of cores utilized. They were $n_{\text{cores}} = [32,\ 64,\ 128,\ 256,\ 512,\ 1024]$.
The main results are summarized in Figure (A.1).

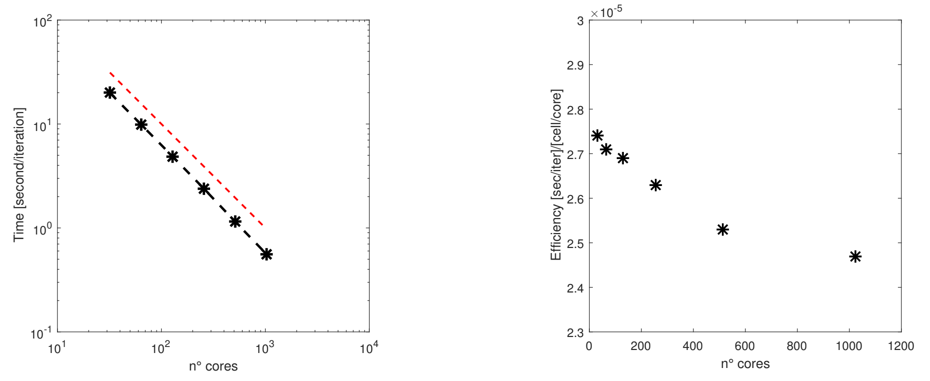

(A)

(B)

Figure A.1: Scalability performances: time per iteration (A), (- -) reference line n_{cores}^{-1}, (- -) CPU time ; efficiency (B).

As it can be seen from Figure (A.1a), the reference line n_{cores}^{-1} shows that the time per iteration scales exactly as $t_{\text{iter}} \propto n_{\text{cores}}^{-1}$.
While for the performance of the code, the index seconds per iteration divided by

cells per core keeps diminishing as the utilized number of cores increases. Anyway, it might be noticed that the curve starts to flatten out, evidencing that the efficiency of the solver is in the neighborhood of optimal conditions using 1024 cores. The maximum efficiency among the tested cases is reached for roughly 20000 cells per core.

After these considerations, the choice of the number of cores was also based on the availability of computational resources. The LES simulations of 53244000 cells were, therefore, chosen to run on 1600 cores, with a number of cells per core around 35000.

Appendix B

Grid Sensitivity Study

A grid sensitivity study has been conducted for the LES simulations of the baseline case. The aim of the analysis is to evaluate the convergence of the results towards the experimental data, as the grid is refined. The mesh size has been reduced to roughly 30 million cells for the intermediate mesh and to 15 million cells for the coarse one. The distance of the first layer height, as well as the discretization in the wall normal direction, has been left unchanged around the airfoil. The mesh was reduced by doubling the Δx^+ size and increasing the spacing and the number of layers in the $z-$direction. The Δz was augmented to 0.000125[m] and 0.00015[m], leading to 60 layers and 50 layers in the spanwise direction, respectively for the medium and the coarse mesh. The results are compared in terms of the NGV loading, circumferential pressure distribution and total pressure losses in the wake.

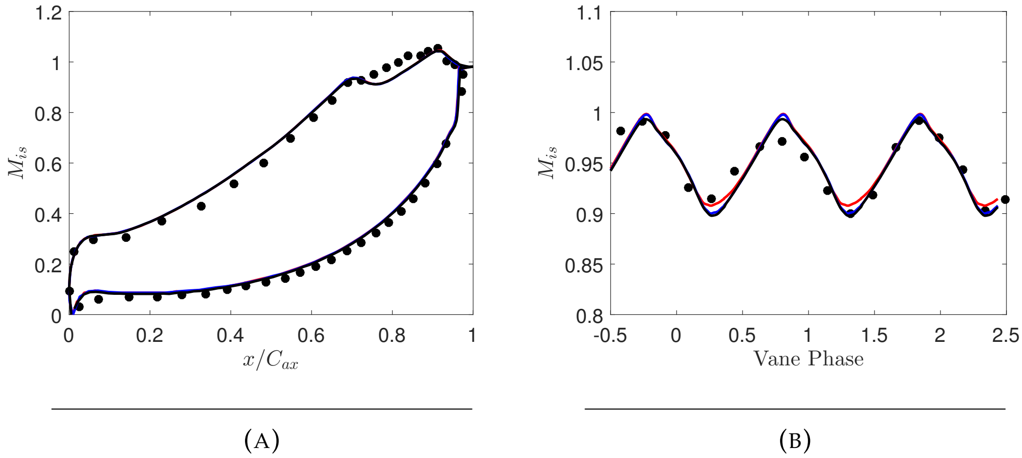

(A)

(B)

FIGURE B.1: NGV blade loading (A) and circumferential pressure distribution (B); (•) experimental data; (—) fine mesh; (—) medium mesh; (—) coarse mesh.

Figure (B.1) shows the NGV loading and the circumferential pressure distribution at a location $x/C_{ax,\text{hub}} = 0.4$ downstream of the vane. The type of graph is similar to the one of Figure (4.16), but now the comparison is among LES simulations of different mesh sizes. It can be noticed that the NGV loading is the same for all three types of mesh, while minimal difference are seen in the circumferential pressure distribution for the coarse mesh of Figure (B.1b).

A similar plot will now be showed in Figure (B.2) in terms of total pressure losses in the wake.

The figure shows that very small differences between the fine and the medium mesh are present in the wake losses profile at $x/C_{ax,\text{hub}} = 0.071$ downstream of the blade. The coarse mesh exhibits, instead, the largest losses in the center of the wake.

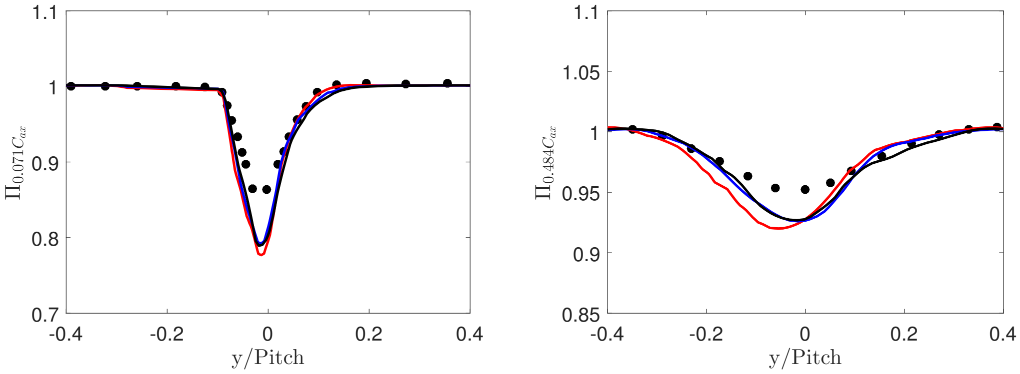

(A) (B)

FIGURE B.2: Total pressure ratio at different downstream locations: $7.1\%C_{ax,\text{hub}}$ (A) and $48.4\%C_{ax,\text{hub}}$ (B) ; (●) experimental data; (—) fine mesh; (—) medium mesh; (—) coarse mesh.

The greatest difference, however, is in terms of the wake position at $x/C_{ax,\text{hub}} = 0.484$ downstream of the passage. Again, small differences are present between the medium and the fine mesh, while the coarse mesh is totally off from the experimental data.

From this analysis, it can be concluded that the medium and the fine mesh almost converge to the same solutions, both agreeing fairly well with the experimental data. The fine mesh is the one adopted in the LES simulations with the entropy waves imposed at the inlet.

Bibliography

[1] ICAO. *2016–2030 Global Air Navigation Plan*. 2016.

[2] M. J. Lighthill. "On Sound Generated Aerodynamically. I. General Theory". In: *Proceedings of the Royal Society of London A: Mathematical, Physical and Engineering Sciences* 211.1107 (1952), pp. 564–587.

[3] A. P. Dowling and Y. Mahmoudi. "Combustion Noise". In: *Proceedings of the Combustion Institute* 35 (2015), pp. 65–100.

[4] M. Kaltenbach, C. Maschke, and R. Klink. "Health Consequences of Aircraft Noise". In: *Deutches Ärzteblatt International* 105.312-32 (2008), pp. 548–556.

[5] C. Eriksson et al. "Aircraft Noise and incidence of hypertension". In: *Epidemiology* 18.716-62 (2007).

[6] L. Jarup, M-L. Dudley, and W. Babisch et al. "Hypertension and Exposure to Noise near Airports (HYENA): Study Design and Noise Exposure Assessment." In: *Environmental Health Perspectives* 113.1473-8 (2008).

[7] E. Greiser, C. Greiser, and K. Janhsen. "Night-Time Aircraft Noise Increases Prevalence of Prescriptions of Antihypertensive and Cardiovascular Drugs Irrespective of Social Class - the Cologne-Bonn Airport study." In: *Journal of Public Health* 15.327-37 (2007).

[8] SA. Stansfels, B. Berglund, and C. Clarc et al. "Aircraft and road Traffic Noise and Children's Cognition and Health: a Cross-National Study". In: *The Lancet* 365.347-58 (2005).

[9] D. Schreckenberg. "Stellungnahme zum Antrag der Landesregierung betreffend Verordnung über die Änderung des Landesentwicklungsplans". In: *ZEUS GmbH* (2007).

[10] S. Bragg. "Combustion Noise". In: *Journal of Institute of Fuel* 36 (1963), pp. 12–16.

[11] W. Strahle. "On Combustion Generated Noise". In: *Journal of Fluid Mechanics* 49.2 (1971), pp. 399–414.

[12] S. Candel. "Analytical Studies of Some Acoustic Problems of Jet Engines". PhD thesis. 1972.

[13] F. E. Marble and S. Candel. "Acoustic Disturbances from Gas Non Uniformities Convected through a Nozzle". In: *Journal of Sound and Vibrations* 55.2 (1977), pp. 225–243.

[14] F. Backe, U. Michel, and I. Rhole. "Investigation of Entropy Noise in Aero-engine Combustors". In: *Journal of Engineering for Gas Turbines and Power* 129 (2007), pp. 370–376.

[15] M. S. Howe. "Indirect Combustion Noise". In: *Journal of Fluid Mechanics* 659 (2010), pp. 267–288.

[16] F. Bake et al. "The entropy Wave Generator (EGW): a reference case on entropy noise". In: *Journal of Sound and Vibrations* 326 (2008), pp. 574–598.

[17] M. Leyko et al. “Numerical and Analytical Modeling of Entropy Noise in a Supersonic Nozzle with Shock”. In: *Journal of Sound and Vibrations* 3.16 (2011), pp. 3944–3958.

[18] N. A. Cumpsty and F. E. Marble. “The Interaction of Entropy Fluctuations with Turbine Blade Rows; a Mechanism of Turbojet Engine Noise”. In: *Proceedings of The Royal Society* 357.1690 (1977), pp. 323–344.

[19] M. Leyko et al. “Simulation and Modeling of the Waves Transmission and Generation in a Stator Blade row in a Combustion-Noise Framework”. In: *Journal of Sound and Vibrations* 333 (2014), pp. 6090–6106.

[20] F. Bake et al. “Indirect Noise Generation in a High Pressure Turbine Stage”. In: *22nd AIAA/CEAS Aeroacoustics Conference* (2016).

[21] P. A. Thompson. *Compressible-Fluid Dynamics*. 1988.

[22] A.J.M. Spencer. *Continuum Mechanics*. 1980.

[23] L. Quartapelle and F. Auteri. *Fluidodinamica Comprimibile*. 2013.

[24] H. B. Callen. *Thermodynamics and an Introduction to Thermostatistics*. 1998.

[25] B. E. Poling, J. M. Prausnitz, J. P. O’connell, et al. *The properties of gases and liquids*. Vol. 5. Mcgraw-hill New York, 2001.

[26] CFD Open. “Openfoam programmer’s guide, version 3.01”. In: *OpenFOAM Foundation* (2015).

[27] Randall J. LeVeque. *Finite-Volume Methods for Hyperbolic Problems*. Cambridge University Press, 2002.

[28] P. Lax and B. Wendroff. “Systems of conservation laws”. In: *Communications on Pure and Applied Mathematics* 13.2 (1960), pp. 217–237.

[29] J. Blazek. *Computational fluid dynamics: principles and applications*. Butterworth-Heinemann, 2015.

[30] V. V. Rusanov. “The calculation of the interaction of non-stationary shock waves and obstacles”. In: *USSR Computational Mathematics and Mathematical Physics* 1.2 (1962), pp. 304–320.

[31] T. J. Barth and D. C. Jespersen. “The design and application of upwind schemes on unstructured meshes”. In: (1989).

[32] S. Chandramouli et al. “Numerical characterization of entropy noise with a density based solver”. In: *ETC2017-143* (2017).

[33] S. K. Godunov. “A difference method for numerical calculation of discontinuous solutions of the equations of hydrodynamics”. In: *Matematicheskii Sbornik* 89.3 (1959), pp. 271–306.

[34] K. Michalak and C. O. Gooch. “Differentiability of slope limiters on unstructured grids”. In: *Proceedings of fourteenth annual conference of the computational fluid dynamics society of Canada*. 2006.

[35] S. P. Spekreijse. “Multigrid solution of the steady Euler equations”. In: (1987).

[36] R. Courant, K. Friedrichs, and H. Lewy. “On the partial difference equations of mathematical physics”. In: *IBM journal of Research and Development* 11.2 (1967), pp. 215–234.

[37] E. Garnier, N. Adams, and P. Sagaut. *Large eddy simulation for compressible flows*. Springer Science & Business Media, 2009.

[38] F. R. Menter et al. “Two-equation eddy-viscosity turbulence models for engineering applications”. In: *AIAA journal* 32.8 (1994), pp. 1598–1605.

[39] D. Wilcox. “Reassessment of the scale-determining equation for advanced turbulence models”. In: *AIAA journal* 26.11 (1988), pp. 1299–1310.

[40] B. E. Launder and B. I. Sharma. “Application of the energy-dissipation model of turbulence to the calculation of flow near a spinning disc”. In: *Letters in heat and mass transfer* 1.2 (1974), pp. 131–137.

[41] J. Smagorinsky. “General circulation experiments with the primitive equations”. In: *Monthly weather review* 91.3 (1963), pp. 99–164.

[42] M. P. Martin, U. Piomelli, and G. V. Candler. “Subgrid-scale models for compressible large-eddy simulations”. In: *Theoretical and Computational Fluid Dynamics* 13.5 (2000), pp. 361–376.

[43] W. W. Kim and S. Menon. “A new dynamic one-equation subgrid-scale model for large eddy simulations”. In: 1995, p. 356.

[44] T. Yasa et al. “Performance of a nozzle guide vane in subsonic and transonic regimes tested in an annular sector”. In: *ASME Turbo Expo 2010: Power for Land, Sea, and Air*. American Society of Mechanical Engineers. 2010, pp. 1457–1467.

[45] N. Glodic. *Experimental Analysis Of Aerodynamic Losses Of A Film Cooled Nozzle Guide Vane In An Annular Sector Cascade*. Tech. rep. KTH, Sweden, 2008.

[46] T. Yasa et al. *Investigation of the Loss Mechanism of a HP Nozzle Guide Vane*. Tech. rep. KTH, Sweden, 2009.

[47] HM Atassi, AA Ali, and OV Atassi. “Interaction of acoustic and vortical disturbances with an annular cascade in a swirling flow”. In: *Unsteady Aerodynamics, Aeroacoustics and Aeroelasticity of Turbomachines* (2006), pp. 247–259.

[48] J. Castillo. *Mathematical aspects of numerical grid generation*. SIAM, 1991.

[49] H. Schlichting et al. *Boundary-layer theory*. Vol. 7. Springer, 1960.

[50] A. P Dowling and Y. Mahmoudi. “Combustion noise”. In: *Proceedings of the Combustion Institute* 35.1 (2015), pp. 65–100.

[51] H.A. Hassan. “Scaling of combustion-generated noise”. In: *J. Fluid Mech.* 66.03 (1974), pp. 445–453.

[52] S. Kotake and K. Takamoto. “Combustion noise: effects of the shape and size of burner nozzle”. In: *J. Sound Vib.* 112.2 (1987), pp. 345–354.

[53] M. Ihme and H. Pitsch. “On the generation of direct combustion noise in turbulent non-premixed flames”. In: *Int. J. Aeroacoust.* 11.1 (2012), pp. 25–78.

[54] D. Papadogiannis et al. “Assessment of the indirect combustion noise generated in a transonic high-pressure turbine stage”. In: *J. Eng. Gas Turbine Power* 138.4 (2016), p. 041503.

[55] B.-T. Chu and L. SG. Kovásznay. “Non-linear interactions in a viscous heat-conducting compressible gas”. In: *J. Fluid Mech.* 3.05 (1958), pp. 494–514.

[56] J. Panda. “Shock oscillation in underexpanded screeching jets”. In: *J. Fluid Mech.* 363 (1998), pp. 173–198.

[57] A. Risborg and J. Soria. “High-speed optical measurements of an underexpanded supersonic jet impinging on an inclined plate”. In: *28th international congress on high-speed imaging and photonics*. International Society for Optics and Photonics. 2008, 71261F–71261F.

[58] J. L. Lumley. “The structure of inhomogeneous turbulent flows”. In: *Atmospheric Turbulence and Radio Wave Propagation* (1967).

[59] K. Karhunen. “Zur spektraltheorie stochastischer prozesse”. In: *Ann. Acad. Sci. Fennicae, AI* 34 (1946).

[60] M. Loéve. *Probability theory: foundations, random sequences*. van Nostrand Princeton, NJ, 1955.

[61] Y.C. Liang et al. “Proper orthogonal decomposition and its applications—Part I: Theory”. In: *Journal of Sound and vibration* 252.3 (2002), pp. 527–544.

[62] L. Sirovich. “Turbulence and the dynamics of coherent structures. I. Coherent structures”. In: *Quarterly of applied mathematics* 45.3 (1987), pp. 561–571.